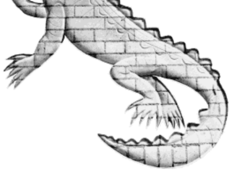

Shocks and jets in Radio Galaxies and Quasars

Sergio Mendoza

Astrophysics Group
Cavendish Laboratory
and
Churchill College
Cambridge
United Kingdom

A dissertation submitted in candidature for the degree of Doctor of Philosophy in the University of Cambridge

1st November 2000

Contents

List of Figures

Preface

This dissertation is the result of work carried out in the Astrophysics group of the Cavendish Laboratory, Cambridge U.K. The work described here is all my own, except where clear reference is made to the work by others. The work in here has not been submitted for a degree, diploma or any other qualification at this, or any other, university. This dissertation does not exceed $60,000$ words in length.

Sergio Mendoza
Cavendish Laboratory
Cambridge, United Kingdom
November, 2000

Acknowledgements

This dissertation would not have been possible to complete without the help of so many people: people not only from the Cavendish Laboratory, but also from outside.

My parents contributed greatly on this. I thank them for always being at my side, listening to me and giving me support. I thank my two sisters, Marisela and Isabel and my four brothers Adrián, Arturo, Roberto and Ricardo for all their encourangement. My sister Marisela deserves special thanks. Her presence in the U.K. has given me a lot of courage and strength in all my work.

I would like to thank my supervisor, Malcolm Longair for the discussions and suggestions given for the fundamental processes of this dissertation. Thanks also to the Astrophysics group of the Cavendish Laboratory, in particular Peter Scheuer, Paul Alexander, Christian Kaiser and Philip Best. Without David Titterington, our system administrator, my computational work would not have gone as smoothly as it did. Discussions with Julia Riley, Guy Pooley and Richard Saunders were very helpful. I should thank greatly my teachers in Cambridge: Malcolm Longair, Martin Rees, Douglas Gough, Jim Pringle and Roger Blandford.

During these past years, friends in the Cavendish Laboratory and the University at large, have been a great support in all parts of my PhD work: Dean Rasheed, Declan Moran, Rafael Carazo Salas, Carlos Calcaneo Roldán, Clovis Peréz, Demetris Charalambus and especially Eric De Silva.

I thank all the hackers I met in Churchill College. It was always great to be surrounded by people who considered GNU/Linux to be a revolutionary philosophy to follow –a movement based on intellectual principles rather than monetary ones. Amongst all of them, I would like to thank Demetris Charalambus. In the computational world, I want to thank the Free Software Foundation. Most of the work done for this dissertation used free software and Debian, their operating system.

Jorge Cantó and Alejandro Raga in the Instituto de Astronomía of the Universidad Nacional Autónoma de México (IAUNAM) were always attentive in my academic education. Both of them gave very useful comments on my work and answered so kindly and thoroughly my questions on their models over the years.

When I first came to England, to study Part *III* Mathematics in Cambridge, I received money as a gift from people of UNAM and IAUNAM in México. To all of them, a big "Thank You" for your trust and for your good wishes. I am very thankful to Estelle Cantillon and Eric Monami for their great moral and somehow economic support.

My funding was provided by the Dirección General de Asuntos del Personal Académico (DGAPA) from the UNAM and the Cavendish Laboratory during the last months of my PhD. I gratefully acknowledge this support.

Finally, I would like to thank Alison Judge for being so patient with me during the last stages of the PhD. She provided a lot of support, more than she could ever imagine.

To my parents: Sergio and Maricela,
my sisters: Marisela and Isabel
and my brothers:
Adrián, Arturo, Roberto and Ricardo,
for their great support and love.

List of symbols

G	Newton's Universal constant of Gravitation
M	Mach number (classical and relativistic)
T	Proper Temperature
V	Proper volume per particle
V	Volume per unit mass
a	Relativistic sound speed
c	Newtonian (classical) sound speed
c	Speed of light
e	Proper internal energy per unit proper volume
k	Riemman curvature
n	Number of particles per unit proper volume
p	Pressure
s	Specific entropy
s	Relativistic interval
u_k	Four velocity
v	Velocity
w	Specific enthalpy
α	Mach angle
γ	Lorentz factor
κ	Polytropic index
ρ	Mass density

σ	Proper specific entropy
ω	Proper specific enthalpy
ϵ	Specific internal energy
Latin indices: $\{a,\ b, \ldots\}$	Take values 0, 1, 2, 3,
Greek indices: $\{\alpha,\ \beta, \ldots\}$	Take values 1, 2, 3,

Abstract

The subject of this dissertation is the interaction of jets in radio galaxies and quasars with their environments. When radio jets expand from the nucleus of an active galaxy, they pass through the interstellar medium of the host galaxy and the neighbouring intergalactic medium. The pressure forces acting on the jet bend it and induce a curvature giving rise to a non-straight shape of the jet. Another interaction occurs when expanding jets collide with stratified clouds in the interstellar and intergalactic medium.

To model deflections produced by jet–cloud and jet–galaxy interactions, a model was developed based on the assumption that, for a jet which expands adiabatically and has reached a steady state, pressure balance must be maintained between the jet material and its surrounding environment. The main consequence of the model is that the bendings in the jets are very sensitive to their initial velocities. For instance, a jet with a high initial Mach number will penetrate the stratified density region with an almost straight trajectory, whereas a low Mach number jet will show pronounced curvatures.

By studying the characteristics emanating from the a jet that bends, it is possible to set an upper limit to the maximum bending angle (the angle the jet makes with its original straight trajectory) for which a jet will not produce an internal shock. The result is that non–relativistic jets with a classical equation of state can only bend by no more than $\sim 75^\circ$ whereas relativistic jets cannot be deflected more than $\sim 50^\circ$.

An important interaction between jets and their surrounding environment occurs in some radio galaxies which show alignment between their optical and radio emission, the so called radio/optical alignment effect. This radiation has been shown to be produced by shock waves in small radio sources. It appears that cold clouds embedded in the interstellar and intergalactic medium collide with the expanding jet, producing shocks which are able to induce the observed emission. When the jets expand, they collide with cold clouds giving rise to a natural scenario for which shock waves are produced as a result of the collision. A model for this shock/cloud collision in one dimension has been developed. This shows in detail that the interaction of the bow shock of the jet transmits a shock inside the cloud and reflects back a rarefaction wave once it crosses it and collides with the rear of the cloud.

Chapter I

Introduction

§1 Extragalactic radio jets

In the early 1900's, observations of the elliptical galaxy M87 (NGC 4486, 3C 274 or Virgo A) carried out by Heber Curtis (Curtis, 1918) revealed a "curious straight jet ... apparently connected with the nucleus by a thin line of matter". These optical observations were not followed up by Curtis and it was not until the development of radio astronomy in the 1960's that jets emanating from the nuclei of certain galaxies became a major theme of research in astrophysics.

The birth of modern radio astronomy began with Karl Jansky who, in May 1933, announced the discovery of the radio emission of our Galaxy (Longair, 1995). His observations were made at 20.5 MHz with a radio antenna built to identify natural sources of radio noise which could interfere with radio transmissions. Grote Reber, a radio engineer and amateur astronomer, built a home radio antenna operating at a 160 MHz with which he confirmed Jansky's discovery and made radio scans along the galactic plane (Reber, 1940). The results of Jansky and Reber ruled out the possibility that the emission could be black body. As an alternative, Reber suggested that it might be bremsstrahlung radiation. However, not long after that, Henyey and Keenan showed that this was also not possible. The origin of this radio emission remained a mystery. The culmination of these early radio astronomical studies was Reber's map of the galactic radio emission (Reber, 1944).

Alfven & Herlofson (1950) were the first to propose that the galactic radio emission might be synchrotron radiation of high energy electrons gyrating in magnetic fields in the atmospheres of stars. In the early 1950's, Kippenhauer and Ginzburg first applied the synchrotron hypothesis to high energy electrons moving in the interstellar magnetic fields. By the mid–1950s, the power–law form and the degree of polarisation of the galactic radio spectrum provided convincing evidence that the radiation was synchrotron.

Soon after the second World War, scientists who were involved in the development of radar began to analyse the nature of cosmic radio emission. Hey and collaborators at the Army Operational Research Group in the United Kingdom discovered the first discrete

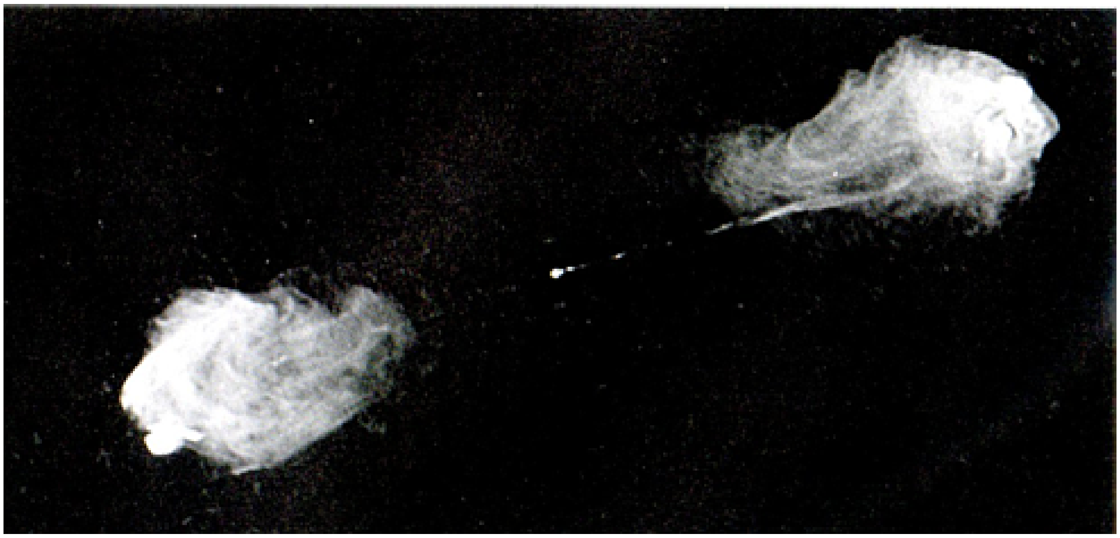

Figure I.1: High resolution image of the archetypical powerful radio galaxy Cygnus A (3C 405) at 5 GHz. Two symmetrical jets of hot fast–moving particles are generated in the central regions of the host galaxy. The jets expand and interact with the intergalactic medium forming radio lobes which expand for tens of kiloparsecs at the edges of the radio galaxy (Perley et al., 1984). The source extends about 150 kpc end to end. In contrast, when the galaxy is observed at optical wavelengths, its size is less than a tenth of its radio length.

radio source in the constellation of Cygnus. This source became known as Cygnus A (see fig.(I.1)) and remains to date the brightest radio galaxy.

Radio astronomy groups at Cambridge, Manchester and Sydney began the construction of more powerful telescopes to study the radio sky. In 1948, Martin Ryle discovered the brightest discrete source in the northern hemisphere, Cassiopeia A. This object was identified by Baade & Minkowski (1954) as a supernova remnant. Baade & Minkowski (1954) also identified the radio source Cygnus A (fig.(I.1)) with a galaxy at redshift $z = 0.057$. The faint optical image had a disturbed appearance comprising two parts. They interpreted the structure of this galaxy as being the result of the collision of two galaxies. Jennison & Das Gupta (1956) showed that the radio emission from Cygnus A did not originate from the galaxy, but rather from two giant patches or radio *lobes* placed symmetrically about the galaxy on the sky. These radio structures are presumed to have a three dimensional structure, like a dumbbell, and are often called *lobes*. Later, it was shown that the double optical structure was only an illusion created by an obscuring lane of dust.

Telescopes of even higher sensitivity and of higher angular resolution were built in the 60's and 70's, particularly at the University of Cambridge, the Westerbork Observatory in the Netherlands and the National Radio Astronomy Observatory (NRAO) in West Virginia. This work culminated with the construction of the Very Large Array (VLA) in New Mexico, which consists of 27 linked radio telescopes, each of 25 meters in diameter configured in a Y-shaped array that span 40 kilometres. With this instrument it became possible to analyse the radio emission of objects like Cygnus A in detail. The type of objects resembling Cygnus A became known as *radio galaxies*. At the outer extremities of the radio lobes in the bright double radio sources, *hot spots*, that is, compact regions of intense radiation, were often observed. Many of the radio sources also showed *bridges* or *tails*, now called *jets*, extending from the hot spots towards the centre of the source, in which there is often a compact region of radio emission called a *core*. Optical identifications of these radio sources revealed that most of the powerful double radio sources are associated with elliptical galaxies, like Cygnus A, or with a quasar[†]. In both cases the core is found to coincide with the galaxy's optical centre.

Even before the beautiful maps made by the VLA were available, theoretical considerations led naturally to a picture in which the hot spots and radio lobes are powered by jets originating in the nucleus of the host galaxy. Rees (1971) suggested that there was a central "*engine*" in the core of the galaxy responsible for all the radio–emitting electrons and magnetic fields. This central engine provided power to the giant lobes to energize their electrons and fields through some sort of "channel". Rees thought that the *beams*, which carry power from the central core to the lobes, were made of ultra–low frequency electromagnetic waves. However, theoretical calculations soon made it clear that electromagnetic beams cannot pass through the galactic interstellar gas.

A few years later, Longair, Ryle & Scheuer (1973) generalised arguments about the dynamical structure of the double radio sources. Instead of the beams being made up of electromagnetic waves, they proposed that beams were made up of hot, magnetised gas. This idea, of a *gas jet* was accepted by Rees and gave rise to the standard model for powerful double radio sources, discussed later on in this Chapter.

§2 Active galactic nuclei (AGN)

By the 1960's, astronomers began to realize that there were unusual signs of activity in the centres of many galaxies. These galaxies had intense concentrations of blue light, quite uncharacteristic of the standard radiation received from aggregates of stars and gas, which are the normal sources of radiation in a galaxy. The spectrum of this new source of light contained too much blue and ultraviolet radiation to come from even the hottest and most massive stars. In some cases, these sources of radiation were found to be as bright as the host galaxy, their emission often varying with time. Galaxies containing these central sources came to be known as *Active Galactic Nuclei* (AGN). Observations made at radio frequencies revealed that certain classes of these galaxies contained narrow, fast jets of gas as was briefly mentioned in the previous section.

It is likely that all galaxies posses some form of activity in their nuclei associated with

---

[†] Quasars are a class of radio sources that look like ordinary stars on photographic plates, but show spectral emission lines with large redshifts. The name stands for *quasi–stellar* objects. They can outshine an entire galaxy by more than a factor of a 1000.

a supermassive black hole. The luminosities of the nuclei can range from $10^{40}\,\mathrm{erg\,s^{-1}}$ to $10^{47}\,\mathrm{erg\,s^{-1}}$.

The classification of AGN is a very confused and confusing subject (Robson, 1996). This is mostly because of observational problems. It is not possible to obtain full spectral coverage for all objects and so, it is not easy to reconcile a classification based on say, X–ray properties with that of optical emission lines of a different sample. Other problems are historical in origin. The phrase "quasi–stellar" object is an example of this. One of the challenges of AGN research is to infer the physical processes that take place in different AGN assuming that they are simple, in spite of the confusing character of the observations (Blandford, 1990).

Let us describe briefly one of the "*modern*" classification schemes. The observational details of these observations can be found in Woltjer (1990) and Robson (1996), and are clearly summarised by Begelman et al. (1984), Blandford (1990), Longair (1995) and Reynolds (1996).

AGN can be divided into two categories, *radio–loud* objects, with a luminosity $L_{5\,\mathrm{GHz}} \gtrsim 10^{24}\,\mathrm{WHz^{-1}sr^{-1}}$, or *radio–quiet*, for which $L_{5\,\mathrm{GHz}} \lesssim 10^{24}\,\mathrm{WHz^{-1}sr^{-1}}$, objects on the basis of their radio properties. About 10 % of all AGN are radio–loud. The rest are radio–quiet.

Radio–loud AGN emit collimated beams or jets of plasma which feed energy and particles to the three dimensional dumbbell structures or lobes (Begelman et al., 1984; Blandford, 1990). The jets and the lobes are sources of continuum radio emission due to synchrotron radiation from relativistic electrons spiralling in a magnetic field in the jets and lobes.

The flow inside the jets in radio–loud AGN may expand, or propagate, with relativistic velocities. This is inferred from the following two observations. Firstly, high spatial resolution radio mapping, with Very Long Baseline Interferometry (VLBI), made at epochs separated by years show that there are blobs within the jet moving outwards from the nucleus. In many cases the proper motion of these blobs in the sky show that the speeds exceed the speed of light. These so–called *superluminal motions* were first predicted by Rees (1966) and they are produced as a result of relativistic motion of the blobs moving at small angles to the line of sight to the observer (Blandford, 1990). Superluminal motion has been the most successful interpretation of these observations, however many other unsuccessful models have been developed to account for it (see Recami et al., 1986, for a review of different models). Secondly, many radio–loud AGN objects, particularly FR—II radio galaxies and radio–loud quasars as defined later, display only one jet. It is very difficult to believe that only one–sided jets are created in symmetrical double radio sources. In fact, it is believed that there are two jets, but due to the relativistic bulk motion of the flow within the jet, there are significant *beaming* effects due to aberration (Begelman et al., 1984; Blandford, 1990). This is believed to be the reason why *counter–jets* are not observed on the radio maps. These observations imply that the bulk motion of the plasma inside the jet has a Lorentz factor $\gamma \sim 3$–10.

Radio–quiet AGN do not show large scale kilo parsec jets. However, some small parsec jets have been observed in some of these sources. An outflow of bipolar radio emission, extending less than 5 kpc, is very often seen from these AGN. There are some larger scale structures associated with this objects, but their nature is rather obscure and they might be the result of an AGN outflow or a starburst driven superwind coming from the host galaxy.

Radio–quiet AGN can be classified on their basis of optical/UV spectral properties. Briefly, this classification is as follows:

✞ *Seyfert I galaxies / radio–quiet quasars.* ➜ Their properties are complex and multi–component. They are often referred as *broad–line* or *type-1* AGN because they have broad permitted optical/UV emission lines (with full width at half maximum FWHM $\sim$ 200–20000 $\mathrm{km\,s^{-1}}$) in the nuclear spectrum. The region from which all this emission arises, the so called *broad line region* (BLR), contains dense photoionised clouds (with an electron number density $n_e \sim 10^9\,\mathrm{cm^{-3}}$) with a small volume filling factor. The optical/UV spectra of these objects shows also narrow permitted and forbidden emission lines (FWHM $\sim 500\,\mathrm{km\,s^{-1}}$). The gas in this region, the *narrow line region* (NLR), is more tenuous that in the BLR and lies at greater distances from the core of the AGN. Traditionally, the distinction between a Seyfert I galaxy and a radio–quiet quasar, often referred as quasi–stellar object or QSO, was made on the basis of whether the galaxy or AGN was discovered first.

✞ *Seyfert II galaxies.* ➜ The spectra of these active nuclei show narrow permitted and forbidden emission lines very similar to those of Seyfert I galaxies. However, Seyfert II galaxies show no broad lines and the optical/UV continuum radiation is much weaker.

Radio–loud AGN can be sub-divided on the basis of their morphology and optical/UV spectral properties. The strong extragalactic radio sources have been divided mainly into two categories, the *extended radio sources*, the bulk of their emission originating from regions more than a kiloparsec from the nucleus of the associated galaxy or quasar, and the *compact radio sources*, in which the emission comes from a region less than a kiloparsec from the nucleus. The extended sources have a steep spectrum $\alpha \sim 0.5$–1[†], whereas the compact sources have a flat one $\alpha \sim 0$–0.5. The majority of the extended radio sources are associated with elliptical galaxies and the minority with quasars. The extended radio sources can be divided into two main categories:

✞ *Fanaroff–Riley type I radio galaxies* (FR I). ➜ These sources are also called *edge–darkened* sources because the radio surface brightness profiles fall continuously as the distance from the nucleus towards the edge of the radio lobe increases. They are low luminosity objects with a luminosity $L_{\mathrm{radio}} \lesssim 10^{42}\,\mathrm{erg\,s^{-1}}$, and usually have two anti–parallel jets emerging from the nucleus of the source. FR I sources show narrow emission lines coming from a NLR, but they do not show broad optical/UV lines.

✞ *Fanaroff–Riley type II radio galaxies* (FR II). ➜ The radio surface brightness

---

[†] The spectral index α is defined by $S_\nu \propto \nu^{-\alpha}$, where S_ν is the flux density at a frequency ν.

of these sources increase as one moves towards the outer edge of the halo, where the jets terminate in strong shocks. As a result of this, FR II radio galaxies are often referred as *edge–brightened* sources. These radio sources are luminous ($L_{\rm radio} \gtrsim 10^{42}\,{\rm erg\,s^{-1}}$) and usually have at most one jet with spectral index $\alpha \sim 0.5$. They show linear polarisation with the electric vector perpendicular to the jet. The optical characteristics of this type of AGN are very similar to Seyfert I galaxies, showing broad and narrow emission lines with a strong continuum, or like Seyfert II galaxies, showing only narrow lines. When Seyfert I–like, these object are classified as *broad–line radio galaxies* (BLRG) and when Seyfert II–like as *narrow–line radio galaxies* (NLRG).

Compact radio sources are mainly divided in two categories:

✞ *Radio–loud quasars.* ➜ The differences between BLRG and radio–loud quasars (RLQ), also known as *quasars*, is blurred. The distinction is largely made on the basis of whether or not the active nucleus overwhelms the light from the galaxy. If this happens the object is called a RLQ. These RLQ objects often have one–sided jets in which superluminal motion is observed. These sources, sometimes called *core–jet* sources have a flat spectrum, $\alpha \sim 0$, core and a somewhat steeper spectrum in the one–sided jet.

✞ *Blazars.* ➜ These are radio–loud objects exhibiting very strong and variable continuum emission at all wavelengths and they have a high optical linear polarisation. The emission lines in these sources are either very weak or absent in the optical/UV spectrum. When these emission lines are present, the objects are classified as *optically violent variable* (OVV) *quasars* and when these lines are absent the sources are referred as *BL Lac objects*, after the first example of this last to be discovered.

§3 Unified model for AGN

The idea of unification for different types of active galactic nuclei came about when it was realized that projection effects must play an important role in the interpretation of some of these sources. Much effort has been expended in determining to what extent different types of AGN are simply different manifestations of the same object viewed from different angles.

The first convincing evidence that Seyfert I and Seyfert II galaxies are one and the same object was put forward by Antonucci & Miller (1985) from studies of the Seyfert II galaxy NGC 1068. They observed polarised scattered broad line emission which was as broad as the broad permitted lines seen in Seyfert I galaxies. These observations gave rise to what has become the standard model for the unification of Seyfert I and Seyfert II galaxies. There exists a “*obscuring torus*” centred about the nucleus of the galaxy which, when observed at a small angle to the axis of the torus, the active nucleus and the broad–line regions are observed. The object is classified as a Seyfert I galaxy. If the axis of the torus is observed at a large angle to the line of sight, only the narrow–line regions, located further away from the nucleus are observed.

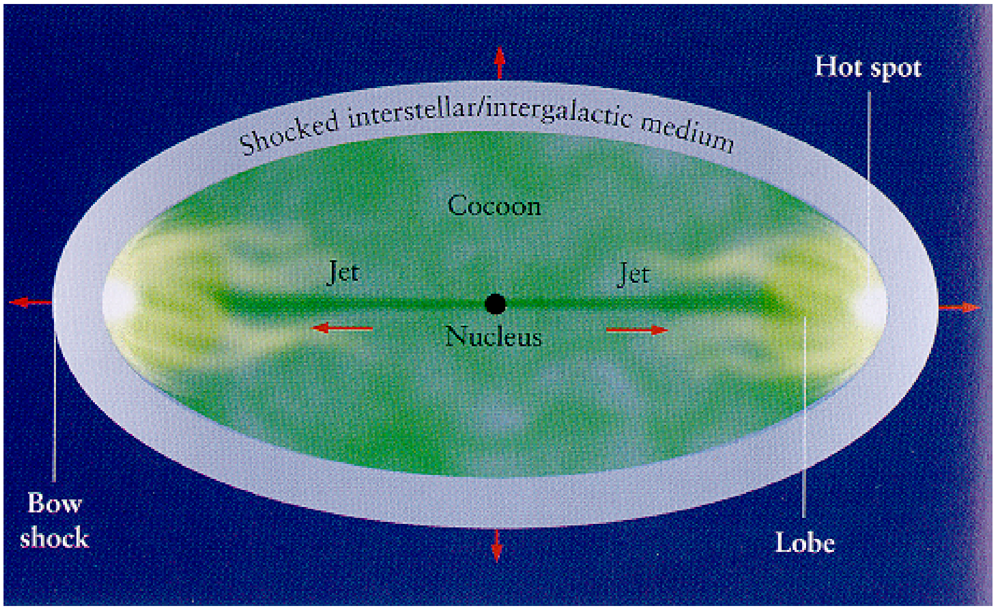

Figure I.2: Structure and mechanism of strong radio sources. A well collimated flow of relativistic material (electron—positron plasma) expands into the intergalactic and interstellar medium of a galaxy buried in the nucleus of the AGN. As the jets expand they form a cavity or cocoon made of jet material which is made of gas from the jet as it is recycled back towards the nucleus or core of the source. The termination of the jets occur on a three dimensional dumbbell structure called lobe. The brightest region in the lobes, and the whole source is called hot spot. They are the product of the collision of the jets with the interstellar or intergalactic medium as they expand. The expansion of the cocoon into the interstellar or intergalactic medium produces a bow shock. Behind this bow shock, lies a region of shocked interstellar or intergalactic medium material which is the interface between the cocoon and the external medium. The boundary between the cocoon and the shocked intergalactic medium is a contact discontinuity. This diagram was taken from Begelman & Rees (1996).

Another unification scheme, first proposed by Barthel (1989a,b), has been developed for strong radio sources. The idea behind this unification is that radio galaxies and radio quasars are the same class of object, viewed at different angles. The model suggests that there is an obscuring torus at the centre of radio galaxies; when the observer views the source within a cone of half–angle roughly 45 ° with respect to the axis of the radio source/torus, the object is identified as a quasar. When the torus hides the active nucleus from the observer, the source is identified as a radio galaxy; when the source is viewed very near the axis of the radio source, the emission of the relativistic flow inside the jet is enhanced because of relativistic beaming and the objects are identified as blazars.

As a result of observations of powerful double radio galaxies, Scheuer (1974) developed what has become the standard model for this type of radio sources (see fig.(I.2)). There is a supermassive blackhole (Begelman et al., 1984; Blandford, 1990) located in the centre of the active galaxy and a pair of relativistic (most probably) electron–positron continuous beams, or jets, expand into the interstellar and intergalactic medium of the source. Each jet forms a very strong shock at its end and the regions where the jet interacts with the intergalactic and interstellar medium are identified in radio maps as hot spots. The shocked material from the head of the jet is recycled back towards the galaxy and forms a cavity or *cocoon* which is effectively a waste basket from the jet material. The cocoon is identified with the extended radio lobes of the radio source. The cocoon and the jet are assumed to be in pressure equilibrium. The expansion of the cocoon into the external medium, that is, the intergalactic or interstellar medium of the host galaxy, produces a bow shock. Behind this bow shock there is a region of shocked interstellar or intergalactic medium. The boundary between this shocked material and the cocoon has to be necessarily a contact discontinuity.

§4 Fluid dynamics of jets

The simplest way to understand the flow of these relativistic jets is to use conservation laws (Begelman et al., 1984; Blandford, 1990). In what follows we will use some of the basic equations derived in Chapter II. This section is included here for consistency with the discussion of jets.

Let us first discuss the case of non–relativistic jet flow, with a polytropic index $\gamma = 5/3$. It is simplest to approximate the jet as a one dimensional flow of variable cross section area A. The rate at which mass is injected into the jet in time t, the *discharge*, is $\dot{M}$. The flow inside the jet has a velocity v. Using eqs.(10.2)-(10.3) it follows that the total energy (kinetic and internal) of the flow inside the jet with respect to time –the *power*, is given by (Blandford, 1990):

$$L = \frac{1}{2}\dot{M}v^2 \left(1 + \frac{3}{M^2} \right) , \tag{4.1}$$

where M is the Mach number of the flow. It follows from the derivation of this relation that the first term inside the parenthesis on the right hand side of eq.(4.1) is the bulk kinetic energy transported by the fluid. The second term is the transport of the enthalpy, that is, the internal energy plus the work pV, where V is the volume. If the jet is steady, the *thrust*, that is the rate of change of momentum with respect to time, is given by (Blandford, 1990):

$$P = \dot{M}v \left(1 - \frac{3}{5M^2} \right) . \tag{4.2}$$

The first term on the right hand side of eq.(4.2) is the rate of supply of bulk momentum flux and the second term is contributed by the gas pressure p. When the flow is highly supersonic, that is $M \gg 1$, it follows from eqs.(4.1)-(4.2) that the bulk motion dominates. The simplest assumption to make is that the jet expands adiabatically and that it is stationary. Under these circumstances, the power and discharge, given by $\dot{M} = \rho A v$ are constants. The mass density is represented by ρ. We assume that the jet is in *pressure equilibrium* with its surroundings.

Since the discharge is constant and because the gas is by assumption adiabatic, it follows that $\rho \propto A^{-1} v^{-1} \propto p^{3/5}$. Thus, the Mach number and the velocity within the jet scale as:

$$M \propto p^{-4/5} A^{-1}, \text{ and } v \propto p^{-3/5} A^{-1}, \tag{4.3}$$

respectively. It follows from eq.(4.3) that the area, as a function of the pressure for a given luminosity, passes through a minimum. This minimum occurs when the velocity of the jet attains the local velocity of sound (Blandford, 1990). In other words, a jet accelerates to supersonic speeds by passing through a *converging–diverging* or *De Laval nozzle* (Begelman et al., 1984; Landau & Lifshitz, 1995). It can be shown that in the subsonic portion of the flow, the pressure and density are approximately constant and so, according to eq.(4.3), the area decreases inversely proportional to the velocity: $A \propto 1/v$. In contrast, for the supersonic regime the velocity is almost constant. Using eq.(4.3), this implies that the area increases as $A \propto p^{-3/5}$. Very often (Binney & Tremaine, 1997) the pressure profile in a galaxy scales with the inverse of the square of the radial coordinate r measured from the centre of the galaxy, that is $p \propto r^{-2}$. This implies that the angle made by the jet width and the axis of the radio source decreases as $A^{1/2} r^{-1} \propto r^{-2/5}$. Thus, we have just proved that a supersonic jet can be collimated as the pressure diminishes, regardless of the expansion of its cross sectional area.

The thrust in an adiabatic jet is not constant. It actually diminishes during subsonic propagation and increases in the supersonic regime. This occurs because the surface of the jet is not exactly parallel to the mean flow velocity and an external pressure force acting parallel to the jet changes its momentum (Begelman et al., 1984; Blandford, 1990).

Let us consider now a fully relativistic jet. The assumptions made are that the fluid inside the jet is an ultra–relativistic plasma with an equation of state $p = e/3 \propto n^{4/3}$, where e is the proper internal energy per unit proper volume and n the number of particles per unit proper volume. The *relativistic power* L can be written down directly using the fact that, if $\mathcal{T}^{km}$ is the energy–momentum tensor and c the speed of light, then $c\mathcal{T}^{0\alpha}$ is the energy flux density vector (see section §8):

$$L = 4 p \gamma^2 v A = \text{const}, \tag{4.4}$$

where γ is the standard Lorentz factor. Since the particle number has to be conserved, it follows from the definition of the continuity equation, eq.(9.1), that

$$n\gamma v A = \text{const.} \tag{4.5}$$

Substitution of eq.(4.4) into eq.(4.5) implies that:

$$A \propto \frac{\gamma^2}{v} \tag{4.6}$$

As in the non–relativistic case, the area A is again minimised at the point where the flow is transonic. The thrust is given by the space components of the energy–momentum tensor:

$$P = \left(4\gamma^2 \frac{v^2}{c^2} + 1\right) pA. \tag{4.7}$$

The thrust changes in exactly the same way as its non–relativistic counterpart does.

Real astrophysical jets do not satisfy necessarily the assumptions we made above. This is because in a real jet, there will be a velocity shear across the jet and most probably turbulence combined with internal shocks inside the jet will develop. There will also be radiative losses and internal dissipation causing particle acceleration. Not even the mass density flux will be constant along the jet, because it is expected that jets entrain gas from the surrounding environment. Finally, perhaps the most important omission from the considerations discussed above is the fact that jets might well be hydromagnetic (Blandford, 1990). Nonetheless, the whole picture provides a framework for studying more detailed effects of the physics of these sources.

§5 Bending of jets in radio galaxies

As jets in radio galaxies expand, they interact with their surrounding environment. There are many examples in which the jets, rather than having a straight trajectory, show changes in their morphology due to interaction with their surroundings induced by different physical mechanisms.

Dramatic curvature is observed in certain FR II radio sources, particularly those known as *radio trails* or *head-tail* objects. A good illustration of of such a source is NGC 1265 shown in fig.(I.3) (see O'Dea & Owen (1986) for detailed multifrequency VLA maps of the source). The jets in this radio galaxy are strongly curved giving the source a semicircular shape, with the host galaxy at the pole. The curvature of the jet is attributed to the motion of the host elliptical galaxy through the high density intracluster medium which results in a significant ram pressure on the radio emitting material of the jet (Begelman et al., 1984). Indeed, the path of the jet can be determined from Euler's equation of hydrodynamics in

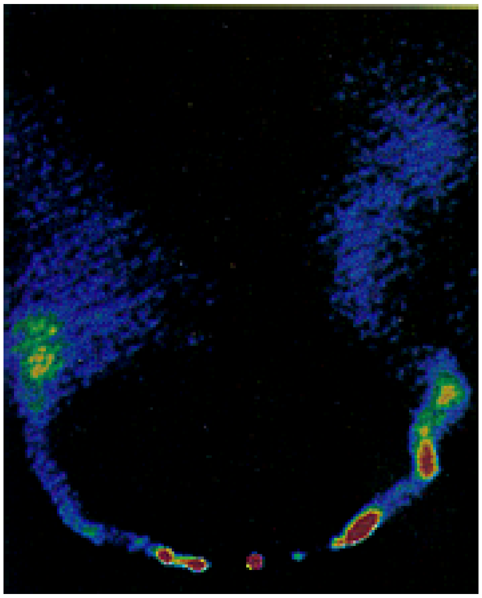

Figure I.3: The prototype radio tail galaxy NGC1265 (Begelman & Rees, 1996). An intergalactic wind directed upwards in the image hits the radio galaxy and produces enough ram pressure on the jets to cause them to bend.

its classical form (Jaffe & Perola, 1973; Begelman et al., 1979; Christiansen et al., 1981; de Young, 1991) or its relativistic generalisation (O'Dea, 1985). In the classical case, the *bending* equation takes the form:

$$\frac{\rho_j v_j^2}{R_{\mathrm{bend}}} = \frac{\rho_e v_g^2}{R_p}, \tag{5.1}$$

for a jet with density ρ_j and internal gas constant velocity v_j. The density of the intergalactic (or external) medium is ρ_e and v_g is the velocity of the host galaxy with respect to the intracluster medium. The radius of curvature of the jet is R_{bend} and the pressure scale length, or the scale over which the ram pressure acting on the beam changes, is R_p. The pressure scale height is assumed to be equal to the width of the jet (de Young, 1991). The meaning of eq.(5.1) is that the centrifugal acceleration exerted by the jet as it curves has to balance the gradient in the ram pressure acting on the jet over a pressure scale height. Integration of eq.(5.1) gives the required shape of the jets. Numerical simulations by de Young (1991) have shown that the simplified *bending* equation is in very good agreement with these more detailed computations.

Another way of inducing deflections in radio jets is caused by a combination of kinetic and geometrical effects. For example, consider the case in which the proper motion of the host galaxy through the intergalactic medium is attributed to the gravitational field of a companion galaxy. In this case each fluid element travelling along the jet follows a straight trajectory, but since the galaxy producing the jet is moving in a Keplerian orbit about its companion, the jet appears to be curved. Sources for which this kind of physical

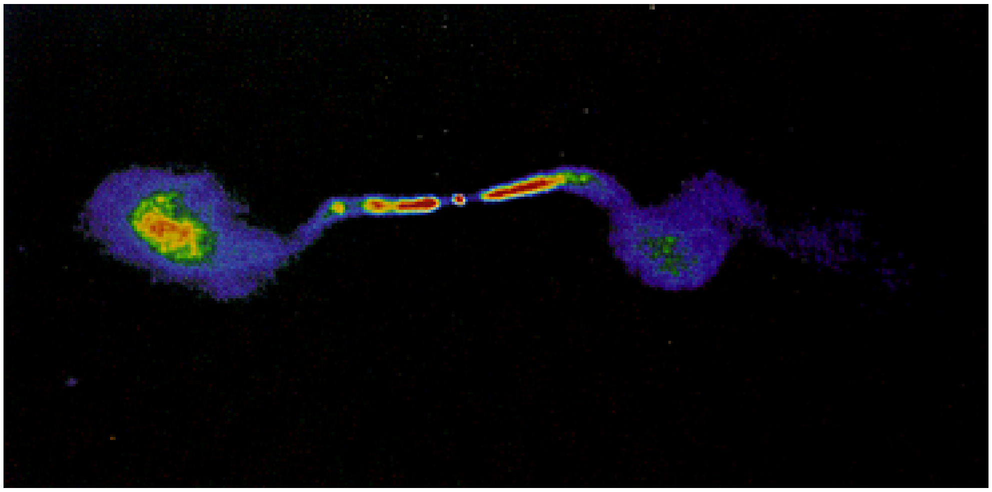

Figure I.4: The radio source 3C 449 shows mirror symmetry which is attributed to the motion of the host galaxy in orbit about a companion (Begelman & Rees, 1996). As the galaxy "rotates" about its close companion the jets bend sharply giving rise to mirror symmetry.

mechanisms occur are called *mirror symmetric*. The prototype radio galaxy 3C 449 shown in fig.(I.4) illustrates this type of symmetry.

The models developed for mirror symmetric radio sources are based in the idea that the material of the jet moves ballistically. This is a first order approximation, but reproduces quite well the shape of the radio sources (Blandford & Icke, 1978).

Radio sources with jets can possess another peculiar shape due to a combination of kinetic and geometrical effects. This occurs if the jets precess about a defined axis. The precession can result in the jet being curved as observed in the plane of the sky, although any fluid particle of the jet always follows a straight trajectory. This behaviour is manifested in the plane of the sky as *inversion* (or 180° rotation) *symmetry*. For example, a bend to the right in one jet becomes a bent to the left in the opposite jet. A typical example is the radio galaxy NGC 326 which is shown in fig.(I.5). It is very likely that this precession originates at the very base of the jet (see Begelman et al., 1984, and references therein), close to the central engine.

A radio source which presents inversion symmetry can be modelled as follows. In its simplest form, the advancing jet moves under the influence of a dynamic pressure force F per unit mass which is given by $\mathsf{F} = (\boldsymbol{w} - \boldsymbol{v})/\mathsf{T}$ where the velocity of the jet beam is $\boldsymbol{v}$, the velocity of the central source is $\boldsymbol{w}$ with respect to the intracluster medium and T is a stopping time. In other words, the equation of motion of the beam is:

$$\frac{\mathrm{d}\boldsymbol{v}}{\mathrm{d}t} = \frac{1}{\mathsf{T}} \left(\boldsymbol{v} - \boldsymbol{w} \right). \tag{5.2}$$

Integration of eq.(5.2) gives:

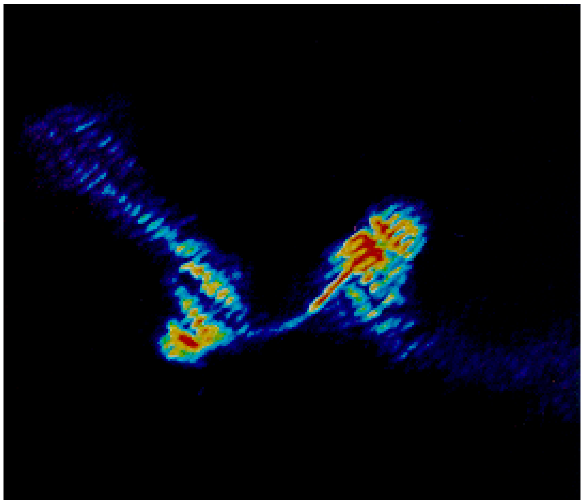

Figure I.5: Inversion symmetry in the radio galaxies source associated with NGC 326. The radio image of the galaxy shows a bend in the top left jet implies a bend to the bottom right jet. This peculiar shape arise because the jets precess about a certain axis, resulting in a cone–like radio structure. The projection on the plane of the sky of this motion produces inversion symmetry.

$$\boldsymbol{v} = \boldsymbol{w} - (\boldsymbol{w} - \boldsymbol{v}_0)\, e^{-t/T}, \tag{5.3}$$

where $\boldsymbol{v}_0$ is the initial velocity of the jet. Again, integration of eq.(5.3) gives the position $\mathbf{r}$ of the beam as a function of time:

$$\mathbf{r} = \boldsymbol{w}t + T\,(\boldsymbol{v}_0 - \boldsymbol{w})\left(1 - e^{-t/T}\right), \tag{5.4}$$

in which $\mathbf{r}(t=0)=0$ has been chosen as the base of the jet. The initial velocity $\boldsymbol{v}_0$ is usually assumed to be constant in magnitude, but it can precess on a cone with opening angle θ and period P (Icke, 1981):

$$\boldsymbol{v}_0 = v_0 \begin{pmatrix} \sin\theta\cos\left[2\pi\,(t_0 - t)\,/P\right] \\ \sin\theta\sin\left[2\pi\,(t_0 - t)\,/P\right] \\ \cos\theta \end{pmatrix}, \tag{5.5}$$

in spherical polar coordinates $(r,\ \theta,\ \varphi = 2\pi\,(t_0 - t)\,/P)$, with a precession period P. With the aid of eqs.(5.4)-(5.5) the inversion symmetry can be modelled to great accuracy for radio galaxies with this particular shape (Icke, 1981).

Evidence exists for deflections of galactic and extragalactic jets when they interact with high density clouds in the interstellar and extragalactic environment surrounding them (see for example Burns, 1986; Bachiller et al., 1995; Best et al., 1998; Lehnert et al.,

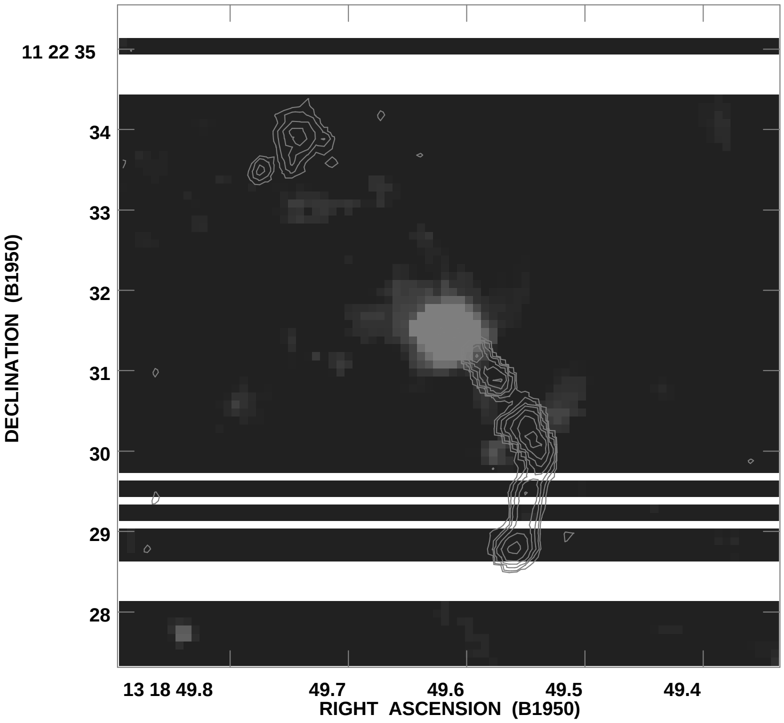

Figure I.6: Quasar PKS 1318 + 113. The figure shows the narrowband Lyα image with VLA 2 cm radio map contours superimposed (Lehnert et al., 1999). The southern jet of the quasar is deflected as it bores a hole through what seems to be two independent Lyα clouds seen at the southwest of the centre of the source.

1999; McNamara et al., 1996).

The first suggestion that a deflection of a jet could be due to its interaction with a cloud was made by Burns (1986), to explain the contradictions encountered when trying to apply the arguments of radio trail sources to *wide angle tail* (WAT) sources. WAT radio galaxies have a similar C–shaped structure, like radio trails but they appear distorted. Indeed, in most sources the tails bend at the point where the jet disrupts, and some others bend after this disruption (O'Donoghue et al., 1990). Burns (1986) came to the conclusion that large bends in WAT's approaching 1 Mpc in scale can not be achieved unless unphysically high speeds through an extremely dense intracluster gas occurs.

More recently, Lehnert et al. (1999) have presented direct evidence for a jet–cloud interaction in the quasar PKS 1318 + 113 (fig.(I.6)). The radio image of PKS 1318 shows a strong deflection of the southern radio jet. The deflection begins to occur exactly at the point at which two separated Lyα clouds seem to be surrounding the radio jet. As explained by Lehnert et al. (1999), it seems that the jet has drilled a hole through the cloud. This is the reason why they appear as two independent clouds around the jet at the point where it begins to curve.

Pressure stratification can cause a jet to curve. This was first proposed by Icke (1991) and extended by Cantó & Raga (1996) and Raga & Cantó (1996). These authors carried out their analysis using non–relativistic jet velocities and assuming that the cloud was a Gaussian sphere, an isothermal plane parallel atmosphere and an isothermal sphere respectively in their publications. In Chapters III–IV a generalisation of their models is analysed together with a description of the stability of the bending jets.

§6 Alignment effect in radio galaxies

HST observations of a sample of 28 3CR radio galaxies with redshifts z in the interval $0.6 < z < 1.3$ were carried out by Best et al. (1996) and are described in detail by Best (1996). The programme had the intention of imaging almost all 3CR radio galaxies in this redshift interval. These 3CR radio galaxies were observed in wavebands corresponding to rest–frame U and B. Additionally, all images were mapped at 1.8 GHz using the VLA, with a resolution of 0.18 arcsec. These galaxies were also observed at $2.2\,\mu$m with the IRCAM3 of the UKIRT at a resolution of 1 arcsec. From these set of observations, Best (1996) produced figs.(I.7)-(I.8). The figures show eight 3CR radio galaxies in the interval $1 < z < 1.3$. The reason as to why this redshift interval was chosen is because within it, all radio galaxies have more or less the same intrinsic radio luminosity. Before analysing in more detail those images, it is important to note that, in general terms, a standard $L^\star$ elliptical galaxy at a redshift $z \sim 1$ is a diffuse low surface brightness object and only objects of high surface brightness, or flat spectra will appear clearly on the images in the optical waveband.

The radio images of these galaxies show the standard picture of a classical FR II source. Two radio lobes extend in opposite directions from the central core. The infrared images show the old stellar populations in these galaxies and they indicate that the host galaxy appears to be an elliptical galaxy, as should be expected. However, the optical images show little resemblance to what should be an elliptical host galaxy. Instead, the optical structures observed in the images align to a high degree with the radio jet axis. This effect, the so called *radio/optical alignment effect* in radio galaxies was first observed by Chambers et al. (1987); McCarthy et al. (1987).

Synchrotron aging arguments have suggested that the greater the separation of the radio source from the nucleus, the older the sources are. This is consistent with a picture in which the sources are powered by a roughly constant energy supply throughout their lifetime. Also, according to the unification scenarios mentioned in section §3, the radio axes of radio galaxies are observed within 45° to the plane of the sky. This implies that the difference between the observed and actual hotspot separations would not be very big and also that the observed structures should lie more or less in the plane of the sky.

As it is seen from the optical images, the oldest radio galaxies do not show a very strong optical structure aligned with the radio jet axis. However, the small, young radio galaxies show a very pronounced effect. This means that the radio/optical alignment effect is relatively short lived. In fact, Best (1996) calculated the ages of the radio galaxies

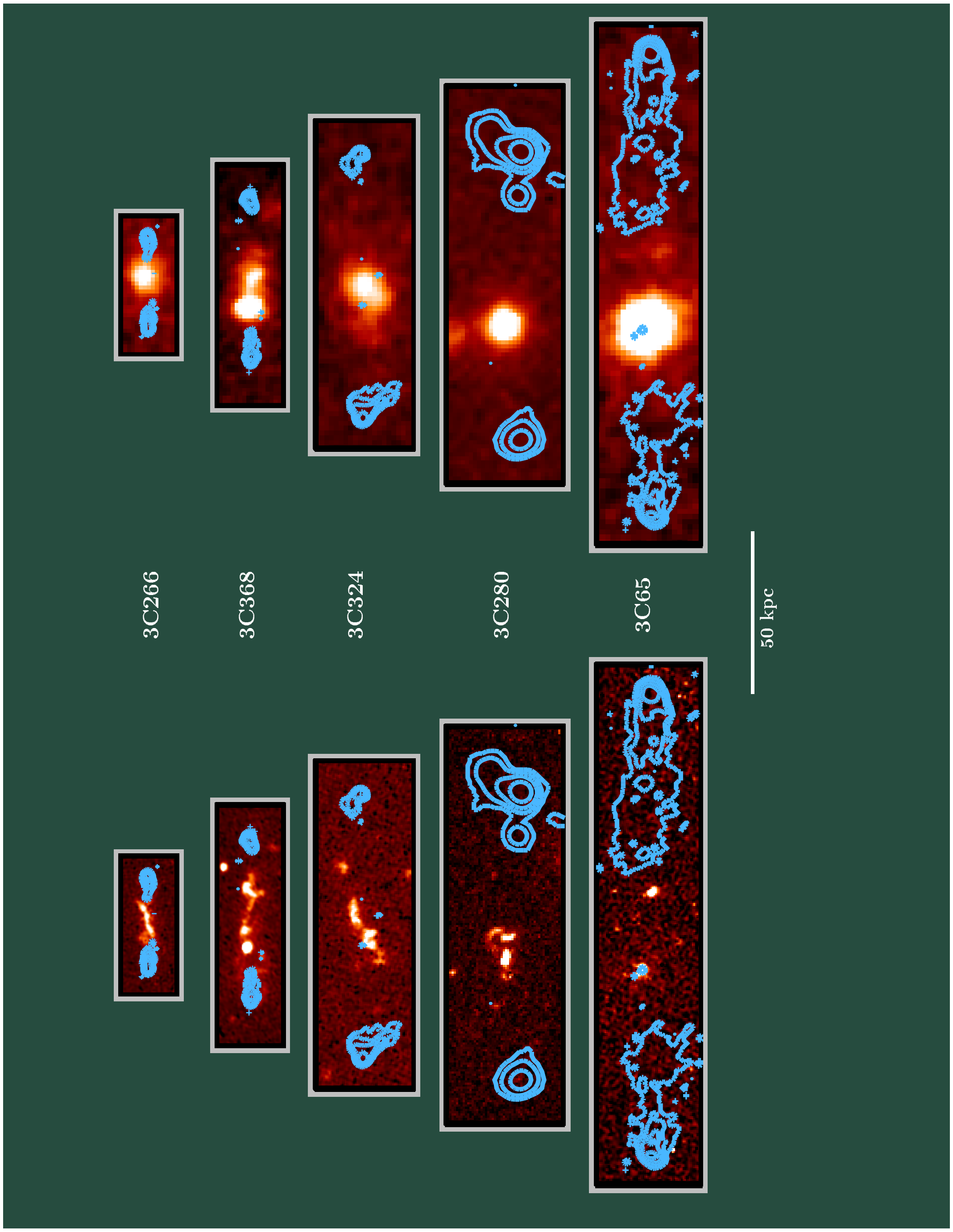

Figure I.7: Five small radio galaxies in the redshift range $1 \lesssim z \lesssim 1.3$ at the same physical scale. The left images show HST images whilst the right ones are UKIRT K-band images. The radio contours had been overlaid on both sets of images. The evolution of the sources with linear size is apparent from the images. These set of images were kindly provided by Philip Best and they are described by Best (1996).

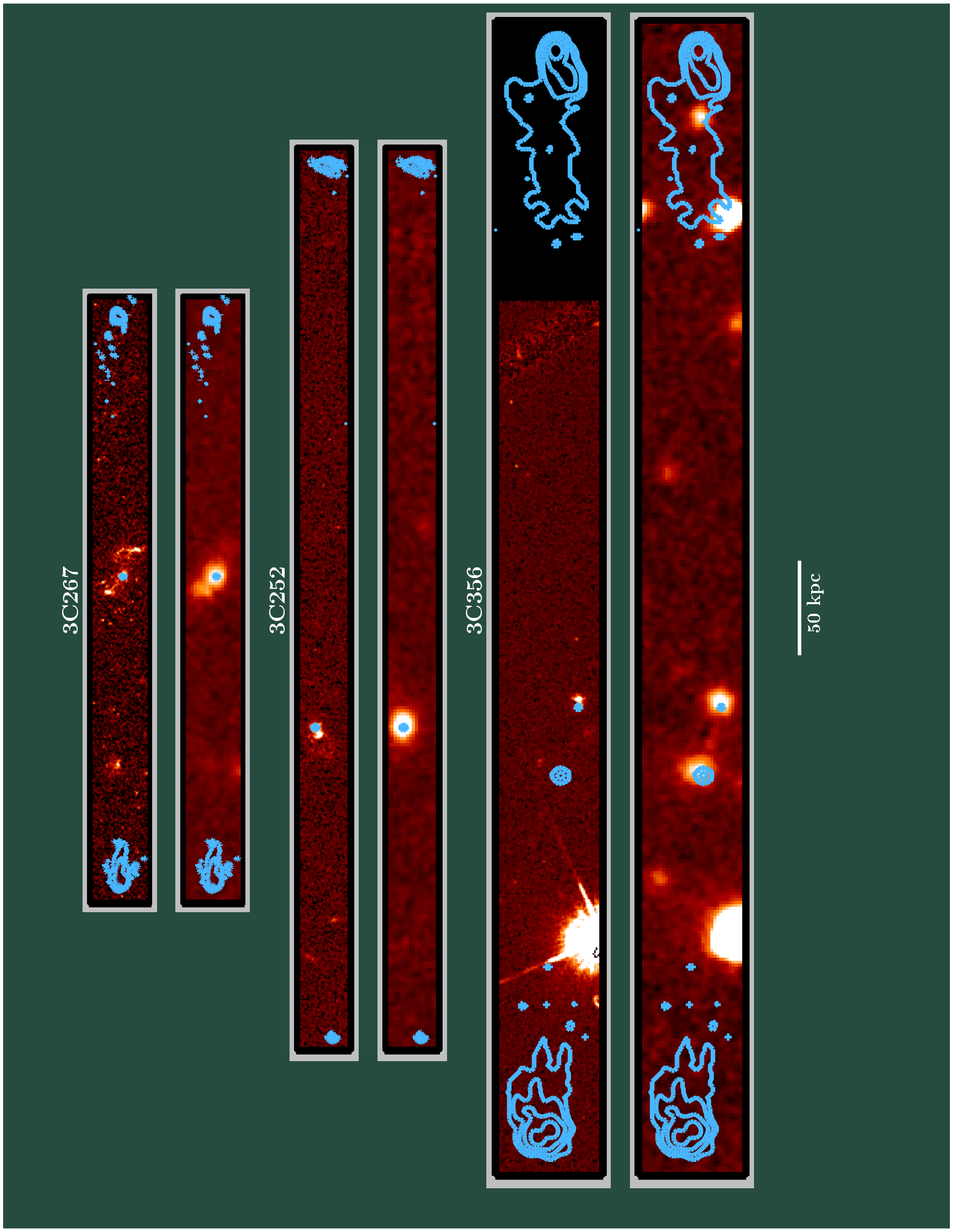

Figure I.8: Three large radio galaxies in the redshift range $1 \lesssim z \lesssim 1.3$ at the same physical scale. For each galaxy, the upper panel shows the HST image, and the lower one the UKIRT K-band image. Radio contours have been overlayed on both images. These images were kindly provided by Philip Best and they are described by Best (1996).

using synchrotron aging arguments and concluded that the activity is completed in about 10 Myr.

All these observations suggest that the aligned optical structures are a short lived phenomena, which is induced by the passage of the radio jet as it expands through the interstellar and intergalactic medium. It seems that, among all the different models that have been proposed in the literature (see Best, 1996, and references therein for a complete description of the different models), there is no single theory that can account for all of the observed features of the alignment between the optical and radio emission (Longair et al., 1995). The observation of polarised optical emission from some of these sources suggests that scattering of light from an obscured quasar could be responsible for these optical structures. A centrally obscured quasar would be responsible to the illumination of pre–existing dust and gas clouds. However, it seems extremely natural that the primary cause must be the interaction of the jet with cool interstellar clouds surrounding the parent galaxy as well as in the intergalactic medium.

McCarthy, van Breugel & Spinrad, and Chambers, Miley & van Breugel proposed that the alignment of the observed optical structures were produced because of enhanced star formation induced in some way by the passage of the radio jet through the interstellar medium of the host galaxy and the intergalactic medium. According to this *jet–induced star formation* picture it would be possible to account for the change in structure with increasing physical size of the radio galaxies. The lifetime of the newly formed stars associated with HII regions would amount to $\sim 10^7$ yr. After this time the luminosities of these star–forming regions decay. The polarisation of the light would then be attributed to the scattering of the light by the dust or gas associated with the star–forming regions.

In an attempt to understand better this jet–induced star formation phenomenon, de Young (1989) performed numerical simulations of high–energy radio jets passing through dense protogalactic gas. He showed that cooling in the regions behind the shocks associated with radio jets can lead to star formation rates over $100\,\mathrm{M}_\odot\,\mathrm{yr}^{-1}$, when the total mass of gas surrounding the galaxies approaches $10^{14}\,\mathrm{M}_\odot$.

Rees (1988) made a more physical proposal about this star–formation idea. He built a model for which the interstellar and intergalactic medium which contained cold ($\sim 10^4$ K) clouds in pressure balance with a hot ($\sim 10^6$ K) medium. These cold clouds are most probably the result of cooling flows (Fabian, 2000). The expansion of the shocks associated with the radio jet expel the hot phase plasma, but leave the clouds within the lobes, where they are squeezed by the higher pressure around them. This compression drives the stable clouds into a gravitational unstable phase, triggering a burst of star formation. After the shock has passed, the clouds find themselves overpressured by a factor of $\sim M^2$, where M is the Mach number of the flow. The value of M is assumed to be ~ 100 along the jet and ~ 10 for the transverse expansion of the cocoon. Since the Jeans Mass $M_J \sim p_{\text{cloud}}^{3/2}/\rho_{\text{cloud}}^2$ (Kron et al., 1995), where p is the pressure and ρ is the density, the above considerations imply that the resultant overpressure over the clouds would trigger collapse of all clouds down to a fraction of any value that lies in the interval 0.01–0.1 of the previous Jeans Mass. This results in a very well synchronised burst of star formation enhanced by a factor of the order of the Mach number.

Begelman & Cioffi (1989) used a similar model to that by Rees, but considered the shock to be radiative. In this case, the cloud's Jeans mass decreases by a factor $(p_{\text{ambient}}/p_{\text{cloud}})^{1/2}$. Clouds which initially have masses somewhat less than the Jeans mass are driven gravitationally unstable by the compression.

Despite the fact that the idea of a jet–induced star formation model is very attractive to account for all these results, observations do not seem to favour this (Best et al., 2000). In fact, it was shown by Best et al. (2000), that for small radio sources ($\lesssim 150\,\text{kpc}$), the morphology, kinematics and ionisation properties of the emission line gas of the radio sources are dominated by the effects of the bow shock associated with the expansion of the radio source through the interstellar and intergalactic medium. Gas clouds embedded in the interstellar and intergalactic medium are accelerated by the shocks, giving rise to the distorted velocity profiles and extreme velocity dispersions observed. On the other hand, large radio sources have more settled kinematical properties. The shock fronts have passed well beyond the emission line regions and the dominant source of ionising photons appears to be the AGN. The diagram shown in fig.(I.9) by Best et al. (2000) shows the evidence for these different means of explaining the optical aligned structures. In Chapter V an analytic one dimensional model of the interaction of a shock wave with a high density region (a cloud) is developed. This one dimensional analysis provides an insight into the more physical mechanisms that might be acting on the interaction of the jet as it expands and interacts with surrounding clouds in pressure balance with the interstellar and intergalactic medium.

§7 Thesis outline

The work presented in this dissertation deals mainly with the interaction of extragalactic jets from powerful double radio sources and their environment. In Chapter II the hydrodynamics needed for all the calculations used later are described. This is achieved by converting the basic equations of relativistic hydrodynamics into useful forms for the study of jet interactions, without considerations of magnetic fields. Chapter III deals with the problem of bending of jets due to jet–cloud interactions. Chapter IV analyses the stability of curved jets against the formation of internal shocks. Chapter V deals with the problem of the collision between a shock wave and a high density region, or cloud. Finally, in Chapter VI the astrophysical implications of all the calculations presented in this dissertation are discussed.

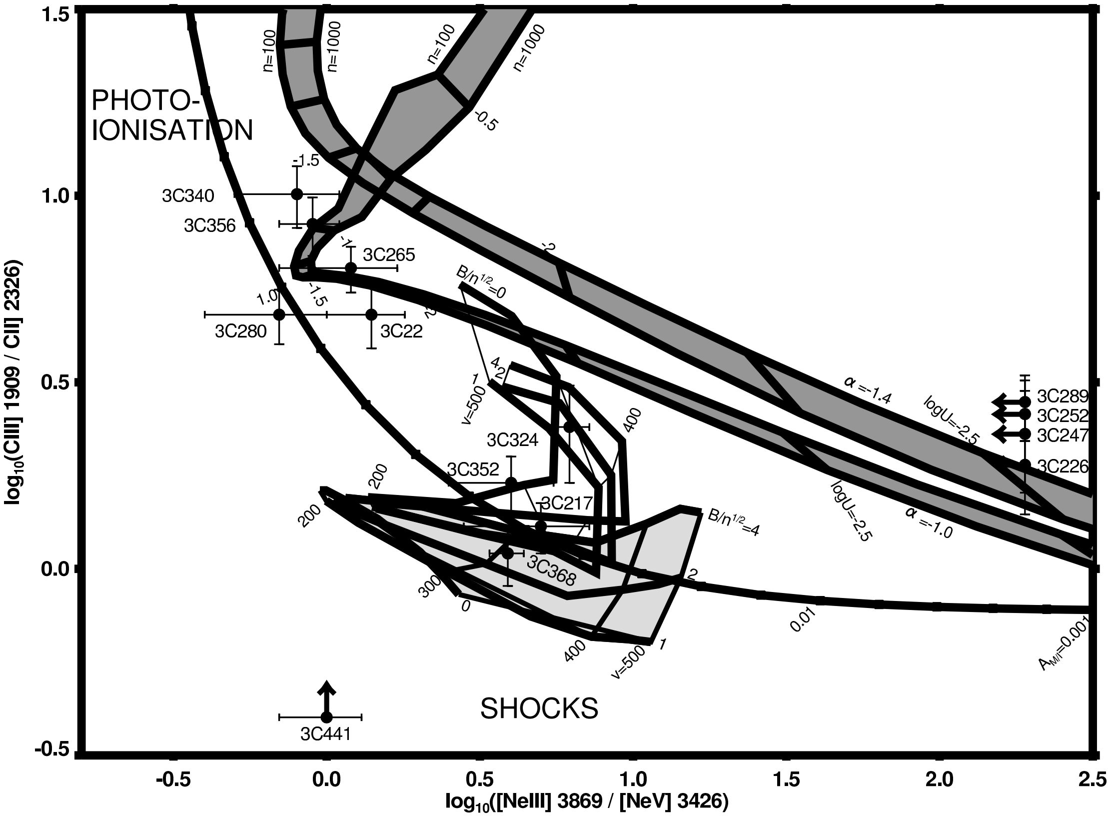

Figure I.9: Emission line diagnostic plot for a particular sample of 3CR radio galaxies, compared with theoretical predictions (Best et al., 2000). Some of these galaxies present the alignment effect shown in figs.(I.8)–(I.9). The upper shadowed regions are simple photoionisation models. The continuous curve that increases towards the right of the diagram is the model for photoionisation models including matter bounded clouds, that is, photoionisation of a composite population containing both optically thin (matter bounded) and optically thick (ionisation bounded) clouds. The lower shadowed region is predicted by shock ionisation models. The upper unshadowed region above this last one is the one for shock models including a precursor region, that is an upstream ionised region produced by photons diffusing into this preshocked gas. The five galaxies plotted at the right of the diagram have no data available for one of their emission lines.

Chapter II

Hydrodynamics

§8 Energy–momentum tensor in relativistic hydrodynamics

In order to derive the relativistic equations of motion in hydrodynamics, let us first construct the energy–momentum 4–tensor $\mathcal{T}^{ik}$ for a fluid in motion on a flat spacetime (Landau & Lifshitz, 1994a, 1995). Latin indices take the values 0, 1, 2, 3 and Greek indices 1, 2, 3. The time t and the speed of light c are related to the time coordinate x^0 by the relation $x^0 = ct$. The Galilean metric g_{ik} for a flat space time is given by $g_{00} = 1$, $g_{11} = g_{22} = g_{33} = -1$ and $g_{ik} = 0$ when $i \neq k$. The different components of the symmetric energy–momentum tensor $\mathcal{T}^{ik}$ are such that the scalar $\mathcal{T}^{00} = \mathcal{T}_{00}$ is the energy density and $\mathcal{T}^{0\alpha}/c = -\mathcal{T}_{0\alpha}/c$ is the α component of the momentum density vector. $\mathcal{T}_{\alpha\beta} = \mathcal{T}^{\alpha\beta}$ represents the 3–momentum flux density tensor and the component $c\mathcal{T}^{0\alpha}$ is the energy flux density vector. The equations of motion are described by the condition:

$$\frac{\partial \mathcal{T}_i^k}{\partial x^k} = 0. \tag{8.1}$$

Consider an element of area $df^\alpha = df_\alpha$ of a three dimensional closed surface which is at rest. Integration of eq.(8.1) over the volume enclosed by this surface gives the change in momentum per unit time –the *momentum flux*–:

$$\frac{1}{c}\frac{\partial}{\partial t}\int \mathcal{T}^{0\alpha} dV = -\oint \mathcal{T}^{\alpha\beta} df_\beta, \tag{8.2}$$

according to Gauss's theorem. The right hand side of eq.(8.2) is the amount of momentum flowing out through the bounding surface in unit time. In other words, the force exerted on an area element df^α by the fluid is $\mathcal{T}^{\alpha\beta} df_\beta$. Consider now some volume element which is at rest in its local proper (or rest) frame. In this system of reference, Pascal's law applies: "*the pressure exerted by a given portion of the fluid is the same in all directions and perpendicular to the surface on which it acts*". Mathematically this is expressed by the relation $\mathcal{T}^{\alpha\beta} df_\beta = p df^\alpha$, where p is the pressure of the fluid. This relation means that $\mathcal{T}_{\alpha\beta} = p\delta_{\alpha\beta}$ and here δ_{ik} is the unit 4–tensor for which $\delta_{ik} = 1$ if $i = k$ and $\delta_{ik} = 0$ if $i \neq k$. On the other hand, in the local proper system of reference, the component $\mathcal{T}^{00} = e$, where e is the proper internal energy density of the fluid. To calculate the remaining components note that, since the fluid is at rest in its local proper frame, the momentum component density $T^{0\alpha}$ vanishes. Therefore, the energy–momentum tensor has the form

$$\mathcal{T}^{ik} = \begin{pmatrix} e & 0 & 0 & 0 \\ 0 & p & 0 & 0 \\ 0 & 0 & p & 0 \\ 0 & 0 & 0 & p \end{pmatrix}, \tag{8.3}$$

in the local proper frame. To find out an expression for $\mathcal{T}^{ik}$ in any frame of reference we use the fact that the fluid 4–velocity u^i has the values $u^0 = 1$ and $u^\alpha = 0$ in the local rest frame. With this and eq.(8.3) it follows that

$$\mathcal{T}^{ik} = \omega u^i u^k - p g^{ik}, \tag{8.4}$$

where $\omega = e + p$ is the heat function per unit volume. Since eq.(8.4) has the same form in any system of reference, it gives the required expression for the energy-momentum 4–tensor in relativistic fluid mechanics.[†]

§9 Equations of motion in relativistic fluid dynamics

The conservation of mass in the absence of any sinks or sources is described by the relativistic continuity equation (Landau & Lifshitz, 1995):

$$\frac{\partial n^k}{\partial x^k} = 0, \tag{9.1}$$

where the particle flux 4–vector $n^k = n u^k$ and the scalar n is the proper number density of particles in the fluid. The energy-momentum tensor in eq.(8.4) does not take into account any dissipative processes and therefore the equations of motion expressed by eq.(8.1) refer to an ideal fluid.

We now project eq.(8.1) on the direction of the 4–velocity, that is, we multiply eq.(8.1) by u^i and use the fact that $u^i u_i = 1$ which implies

---

[†] When discussing relativistic fluid mechanics we take the values of the different thermodynamic quantities in their local proper frame. For example the internal energy density e, the enthalpy per unit volume ω, the entropy density σ, and the temperature T are all referred to this system of reference. The pressure p, being a relativistic invariant, could be described in any frame of reference.

$$nu^k\left\{\frac{\partial}{\partial x^k}\left(\frac{\omega}{n}\right)-\frac{1}{n}\frac{\partial p}{\partial x^k}\right\}=0. \tag{9.2}$$

By the first law of thermodynamics:

$$\mathrm{d}\,(\omega/n)=T\mathrm{d}\,(\sigma/n)+(1/n)\,\mathrm{d}p, \tag{9.3}$$

in which T is the temperature and σ the entropy per unit volume, together with the continuity equation, eq.(9.1), it follows that eq.(9.2) can be rewritten as:

$$u^k\frac{\partial}{\partial x^k}\left(\frac{\sigma}{n}\right)\equiv\frac{\mathrm{d}}{\mathrm{d}s}\left(\frac{\sigma}{n}\right)=0, \tag{9.4}$$

where the derivative $\mathrm{d}/\mathrm{d}s$ means differentiation along the world line s of the fluid element concerned and the interval $\mathrm{d}s^2=g_{ik}\mathrm{d}x^i\mathrm{d}x^k$. Eq.(9.4) means that the fluid is adiabatic.

Let us now project eq.(8.1) on a direction orthogonal to u^i. To do so, note that the tensor $\{\delta_i^l-u_iu^l\}$ is perpendicular to u^i. We can multiply eq.(8.1), that is $\partial T_l^k/\partial x^k=0$, by this tensor and find

$$\frac{\partial T_i^k}{\partial x^k}-u_iu^l\frac{\partial T_l^k}{\partial x^k}=0,$$

which is indeed a perpendicular vector to u^i. Expansion of this relation results in the equation:

$$\omega u^k\frac{\partial u_i}{\partial x^k}=\frac{\partial p}{\partial x^i}-u_iu^k\frac{\partial p}{\partial x^k}, \tag{9.5}$$

which is the 4–dimensional Euler equation. The three spatial components constitute the relativistic Euler equation:

$$\frac{\gamma\omega}{c^2}\left\{\frac{\partial \boldsymbol{v}}{\partial t}+\boldsymbol{v}\cdot\mathbf{grad}\,\boldsymbol{v}\right\}=-\mathbf{grad}\,p-\frac{\boldsymbol{v}}{c^2}\frac{\partial p}{\partial t}, \tag{9.6}$$

where $\boldsymbol{v}$ is the flow velocity and the Lorentz factor γ is given by $\gamma=1/\sqrt{(1-v^2/c^2)}$. The time component of eq.(9.5) is implied by the other three. In the case of isentropic flow, that is, when σ/n=const, and assuming the flow to be steady, the spatial components of eq.(9.5) give

$$\gamma\,(\boldsymbol{v}\cdot\mathbf{grad})\,(\gamma\omega\boldsymbol{v}/n)+c^2\mathbf{grad}\,(\omega/n)=0.$$

Scalar multiplication by $\boldsymbol{v}$ leads to $(\boldsymbol{v}\cdot\mathbf{grad})(\gamma\omega/n)=0$ which implies that along any streamline the quantity

$$\gamma\omega/n=\text{const.} \tag{9.7}$$

This is the relativistic version of Bernoulli's equation.[†]

§10 Classical equations of hydrodynamics

In order to derive the classical[‡] equations of hydrodynamics, let us first note the difference between the values of the thermodynamic quantities in the relativistic case and those used classically. To begin with, the quantities in the relativistic case are defined with respect to the proper system of reference of the fluid. In classical mechanics these quantities are referred to the laboratory frame. In the relativistic case the thermodynamic quantities, such as the internal energy density e, the entropy density σ and the enthalpy density ω are all defined with respect to the proper volume of the fluid. In classical fluid dynamics, these quantities are defined in units of the mass of the fluid element they refer to. For instance, the specific internal energy ϵ, the specific entropy s and the specific enthalpy w are all measured per unit mass in the laboratory frame. When taking the limit in which the speed of light c tends to infinity we must also bear in mind that the internal energy density e includes the rest energy density nmc^2, where m is the rest mass of the particular fluid element under consideration. Therefore the following classical limits should be taken in passing from relativistic to classical fluid dynamics:

$$\begin{aligned} mn &\xrightarrow[c\to\infty]{} \rho\sqrt{1-v^2/c^2}\approx\rho\left(1-v^2/2c^2\right), \\ e &\xrightarrow[c\to\infty]{} nmc^2+\rho\epsilon\approx\rho c^2-\frac{1}{2}\rho v^2+\rho\epsilon, \\ \frac{\omega}{n} &\xrightarrow[c\to\infty]{} mc^2+m\left(\epsilon+\frac{p}{\rho}\right)\approx m\left(c^2+w\right), \end{aligned} \tag{10.1}$$

where ρ is the mass density of the fluid in the laboratory frame. Using these limiting values, the equation of continuity eq.(9.1), Euler's equation eq.(9.6) and the conservation of entropy eq.(9.4) have their classical analogues respectively:

[†] Bernoulli's equation is also obtained directly from the time component of eq.(9.5) when the flow is steady and isentropic. The result is $\gamma(v/c)\cdot\mathbf{grad}(\omega\gamma/n)=0$, which is equivalent to eq.(9.7).

[‡] Here and in what follows we use the word "*classical*" to mean non–relativistic.

$$\frac{\partial \rho}{\partial t} + \mathrm{div}\,(\rho \boldsymbol{v}) = 0, \tag{10.2}$$

$$\frac{\partial \boldsymbol{v}}{\partial t} + (\boldsymbol{v} \cdot \mathbf{grad})\, \boldsymbol{v} = -\frac{1}{\rho}\mathbf{grad}\, p, \tag{10.3}$$

$$\frac{\partial s}{\partial t} + (v \cdot \mathbf{grad})\, s = 0 \tag{10.4}$$

In the same approximation, eq.(9.7) gives the classical version of Bernoulli's equation, that is,

$$\frac{1}{2}v^2 + w = \mathrm{const}, \tag{10.5}$$

for a given streamline. The constant in the right hand side of eq.(10.5) differs from the constant in the right hand side of eq.(9.7) by an unimportant additional term.

When gravitational effects are taken into consideration, Euler's equation, and hence Bernoulli's law, have to be changed appropriately in order to account for the force exerted by the gravity on the flow of a given fluid element:

$$\frac{\partial \boldsymbol{v}}{\partial t} + (\boldsymbol{v} \cdot \mathbf{grad})\, \boldsymbol{v} = -\frac{1}{\rho}\mathbf{grad}\, p - \mathbf{grad}\, \phi, \tag{10.6}$$

$$\frac{1}{2}v^2 + w + \phi = const, \tag{10.7}$$

where the gravitational potential ϕ is related to the gravitational acceleration $\mathbf{g}$ by the relation $\mathbf{g} = -\mathbf{grad}\, \phi$.

§11 Characteristics

Let us consider now the one dimensional problem of a relativistic flow in which dissipation processes are not taken into account, that is, the entropy remains constant as the fluid moves. For this particular case, the continuity equation, eq.(9.1) and the x–component of the equations of motion, eq.(8.1) are given by:

$$\frac{\partial}{\partial t}(\gamma n) + \frac{\partial}{\partial x}(\gamma n v) = 0, \tag{11.1}$$

and

$$\frac{1}{c^2}\frac{\partial}{\partial t}\left(\omega v \gamma^2\right) + \frac{\partial}{\partial x}\left(\frac{\omega v^2 \gamma^2}{c^2} - P\right) = 0 \tag{11.2}$$

respectively. If we define the quantities:

$$\alpha \equiv \frac{a}{c} \equiv \left(\frac{\partial P}{\partial e}\right)_{\sigma}, \tag{11.3}$$

$$\varphi \equiv \frac{1}{c}\int \frac{a}{n} dn, \tag{11.4}$$

then eq.(11.1) and eq.(11.2) can be written as:

$$\left(1-\frac{v^2}{c^2}\right)\left\{\frac{1}{c}\frac{\partial\varphi}{\partial t}+\frac{v}{c}\frac{\partial\varphi}{\partial x}\right\}+\frac{\alpha}{c}\left\{\frac{v}{c^2}\frac{\partial v}{\partial t}+\frac{\partial v}{\partial x}\right\}=0, \tag{11.5}$$

$$\alpha\left(1-\frac{v^2}{c^2}\right)\left\{\frac{v}{c^2}\frac{\partial\varphi}{\partial t}+\frac{\partial\varphi}{\partial x}\right\}+\frac{1}{c^2}\frac{\partial v}{\partial t}+\frac{v}{c^2}\frac{\partial v}{\partial x}=0. \tag{11.6}$$

Addition and substraction of these two relations gives:

$$\mathcal{D}_{\pm}\left(\frac{v}{c}\right) \pm \left(1-\frac{v^2}{c^2}\right)\mathcal{D}_{\pm}\varphi = 0, \tag{11.7}$$

where:

$$\mathcal{D}_{\pm} f \equiv \left(1 \pm \alpha\frac{v}{c}\right)\frac{1}{c}\frac{\partial f}{\partial t} \pm \left(\alpha \pm \frac{v}{c}\right)\frac{\partial f}{\partial x}, \tag{11.8}$$

for any function $f(t,x)$. From the definitions of the operator $D_{\pm}$ in eq.(11.8), it follows that:

$$\frac{\mathcal{D}_{\pm}\left(v/c\right)}{1-v^2/c^2} = \mathcal{D}_{\pm}\ln\left\{\frac{1+v/c}{1-v/c}\right\}^{1/2},$$

and hence, eqs.(11.7) become:

$$\left(1-v^2/c^2\right)\mathcal{D}_{\pm}\left\{\ln\left(\frac{1+v/c}{1-v/c}\right) \pm \varphi\right\} = 0. \tag{11.9}$$

If we now introduce the parameters:

$$\mathcal{J}_{\pm} \equiv \varphi \pm \ln\left\{\frac{1+v/c}{1-v/c}\right\}^{1/2}, \tag{11.10}$$

which are called *Riemann invariants*, then eqs.(11.9), that is, eqs.(11.1)-(11.2), become equivalent to (Taub, 1948, 1978):

$$\left[\left(1 \pm \alpha\frac{v}{c}\right)\frac{1}{c}\frac{\partial}{\partial t} \pm \left(\alpha \pm \frac{v}{c}\right)\frac{\partial}{\partial x}\right]\mathcal{J}_{\pm} = 0. \tag{11.11}$$

From this relation it follows that the Riemann invariants $\mathcal{J}_{\pm}$ are constant along the curves $\mathrm{d}x/\mathrm{d}t = \pm c(\alpha \pm v/c)/(1 \pm \alpha v/c)$ respectively. These curves $\mathcal{C}_{\pm}$ are called *characteristics* and play an essential role in fluid dynamics. The differential operators that appear inside the brackets in eq.(11.11) are the operators of differentiation along the characteristics $\mathcal{C}_{\pm}$ in the x–t plane.

In general terms, a disturbance is said to propagate as a *travelling wave* (Landau & Lifshitz, 1995; Taub, 1948) if either $\mathcal{J}_{+}$ or $\mathcal{J}_{-}$ is constant. For instance, consider the case in which $\mathcal{J}_{-}=$const, then from eq.(11.10), and eq.(11.11) it follows that (Taub, 1948):

$$\frac{1}{c}\frac{\partial\varphi}{\partial t} + \Psi(\varphi)\frac{\partial\varphi}{\partial x} = 0, \tag{11.12}$$

with

$$\Psi(\varphi) \equiv \frac{\alpha + v/c}{1 + \alpha v/c}. \tag{11.13}$$

The general solution of eq.(11.12) is

$$f(\varphi) = x - \Psi(\varphi)ct \tag{11.14}$$

in which $f(\varphi)$ is an arbitrary function. The relation eq.(11.14) means that φ is constant along straight lines with slope $\Psi(\varphi)$ in the plane x–ct. In other words, $\Psi(\varphi)$ is the velocity of propagation of φ. From the definition of Ψ in eq.(11.13) it follows that, for weak disturbances in which $v \to 0$, then $\Psi(\varphi) \to \alpha$.

The speed of sound is the velocity at which adiabatic perturbations of small amplitude in a compressible fluid move with respect to the flow. Due to the fact that $\Psi(\varphi) \to \alpha$ as $v \to 0$, it is obvious that α represents the *speed of sound* in units of the speed of light†.

The properties of *subsonic* and *supersonic* flow, that is flow with velocity less or greater than that of sound, are completely different in nature. To begin with, let us see how perturbations with small amplitudes are propagated along the flow for both, subsonic and supersonic flows. For simplicity in the following discussion we will consider two dimensional flow only. The relations obtained below are easily generalised for the general case of three dimensions.

---

†When speaking of perturbations that travel at the speed of sound with respect to the flow, we have in mind perturbations that do not involve entropy and vorticity perturbations which are transmitted with the flow itself (Landau & Lifshitz, 1995).

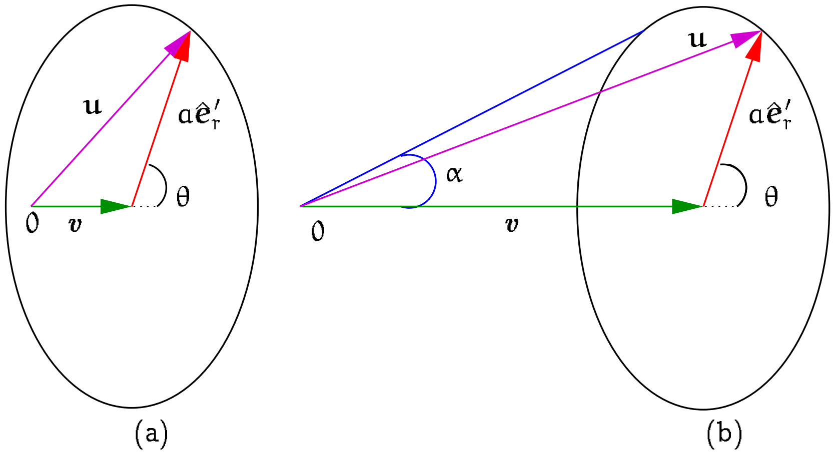

Figure II.1: Region of influence of small amplitude perturbations. A perturbation of small amplitude is produced in the flow at some point 0. This is carried by the flow which has a velocity v. In the case of subsonic flow, as shown in panel (a), the perturbation is able to propagate to the whole space. When the flow is supersonic the perturbation is propagated only downstream inside a cone with aperture angle 2α. The speed of sound a and the angle θ are measured in a frame of reference in which the flow is at rest –the proper frame of the flow. The vector $\mathbf{u}$ is the relativistic addition of vectors v and $a\hat{\mathbf{e}}'_r$, where $\hat{\mathbf{e}}'_r$ is a unit radial vector in the proper frame of the flow.

If a gas in a steady motion receives a small perturbation, this propagates through the gas with the velocity of sound relative to the flow itself. In another system of reference, the *laboratory frame*, in which the velocity of the flow is v along the x axis, the perturbation travels with an observed velocity $\mathbf{u}$ whose x and y components are given by:

$$u_x = \frac{a\cos\theta + v}{1 + av\cos\theta/c^2}, \tag{11.15}$$

$$u_y = \frac{\gamma^{-1} a \sin\theta}{1 + av\cos\theta/c^2}, \tag{11.16}$$

according to the rule for the addition of velocities in special relativity (Landau & Lifshitz, 1994a). The polar angle θ and the velocity of sound a are both measured in the proper frame of the fluid. Since a small disturbance in the flow moves with the velocity of sound in all directions, the parameter θ can have values $0 \leq \theta \leq 2\pi$. This is illustrated pictorially in fig.(II.1).

Let us consider first the case in which the flow is subsonic, as is presented in case (a) of fig.(II.1). Since by definition $v < a$ and $c^2 > av$, it follows from eqs.(11.15)-(11.16) that $u_x(\theta = \pi) < 0$ while $u_y(\theta = \pi) = 0$. In other words, the region influenced by the perturbation contains the velocity vector $\boldsymbol{v}$. This means that the perturbation originating at 0 is able to be transmitted to all the flow.

When the velocity of the flow is supersonic, the situation is quite different, as shown in case (b) of fig.(II.1). For this case it follows that $u_x(\theta = \pi) > 0$ and $u_y(\theta = \pi) = 0$.

In other words, the velocity vector $\boldsymbol{v}$ is not fully contained inside the region of influence produced by the perturbation. This implies that only a bounded region of space will be influenced by the perturbation originated at position 0. For the case of steady flow, this region is evidently a cone. Thus, a disturbance arising at any point in supersonic flow is propagated only downstream inside a cone of aperture angle 2α. By definition, the angle α is such that it is the angle subtended by the unit radius vector $\hat{\mathbf{e}}_r$ with the velocity vector $\boldsymbol{v}$ at the point in which the azimuthal unit vector $\hat{\mathbf{e}}_\alpha$ is orthogonal with the tangent vector $\mathrm{d}(a\hat{\mathbf{e}}'_r)/\mathrm{d}\theta$ to the boundary of the region influenced by the perturbation. The unit vector $\hat{\mathbf{e}}'_r$ is the unit radial vector in the proper frame of the flow. In other words, the angle α obeys the following mathematical relation:

$$\frac{\mathrm{d}\left(a\hat{\mathbf{e}}'_r\right)}{\mathrm{d}\theta}\cdot\hat{\mathbf{e}}_\alpha = 0. \tag{11.17}$$

Substitution of eqs.(11.15)-(11.16) into eq.(11.17) gives:

$$\tan\alpha = -\gamma\left\{\frac{1}{\tan\theta} + \frac{av}{c^2\sin\theta}\right\}. \tag{11.18}$$

On the other hand, since $\tan\alpha = u_y/u_x$, it follows from eqs.(11.15)-(11.16) and eq.(11.18) that:

$$\tan\theta = -\frac{v}{a}\sqrt{1-\frac{a^2}{v^2}}\,,$$

so eq.(11.18) gives a relation between the angle α, the velocity of the flow v and its sound speed a:

$$\tan\alpha = \gamma^{-1}\frac{a/v}{\sqrt{1-(a/v)^2}} \tag{11.19}$$

This variation of the angle α is plotted in fig.(II.2) for the case in which the gas is assumed to have a relativistic equation of state, that is, when $p = e/3$. The important feature to note from the plot is that the aperture angle of the cone of influence is reduced when the velocity of the flow approaches that of light.

From eq.(11.19) it follows that, as the velocity of the flow approaches that of light, the angle α vanishes. In other words, as the velocity reaches its maximum possible value, the perturbation is communicated in a very narrow region along the velocity of the flow.

In studies of supersonic motion of fluid mechanics it is very useful to introduce a dimensionless quantity M defined as:

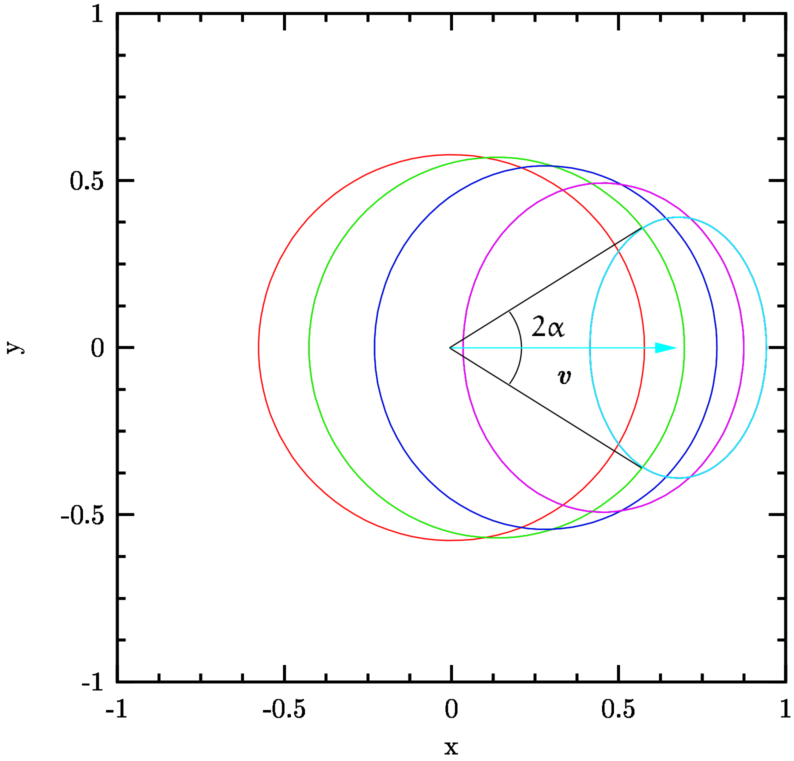

Figure II.2: Region of influence of a perturbation for different values of the velocity of a relativistic gas with a sound speed $a = c/\sqrt{3}$. From left to right the closed loops correspond to values of the velocity v of 0.0, 0.2, 0.4, ..., 0.8 in units of the speed of light c. The perturbation is assumed to originate at the origin of the proper system of reference of the flow. In the case of supersonic flow, the region of influence occurs only downstream inside a cone with aperture angle 2α. This cone surrounds the corresponding loop and is tangent to it. When the flow is subsonic, the perturbation is transmitted to all the flow. As a particular example, the cone and the velocity vector have been drawn for the case in which the velocity is $v = 0.8c$.

$$\frac{1}{M} \equiv \sin\alpha = \frac{\gamma_a}{\gamma}\frac{a}{v}, \tag{11.20}$$

according to eq.(11.19). The quantity $\gamma_a \equiv 1/\sqrt{1-(a/c)^2}$ is the Lorentz factor for the velocity of sound a. The number M has the property that $M \to 1$ as $v \to a$ and $M \to \infty$ as $v \to c$. It also follows that $M > 1$ if and only if $v > a$.

The surface bounding the region reached by a disturbance starting from the origin 0 is called a *characteristic surface* (Landau & Lifshitz, 1995). This definition of characteristic and that given above, when the Riemann invariants were introduced, are the same in the sense that the characteristics introduced here are curves in the x–y plane which cut the streamlines in this plane at the Mach angle. Those discussed above correspond to curves in the x–t plane which cut the *streamlines* (that is, the curves $x(t)$ for which $dx/dt = v$) at the Mach angle in this plane.

In the general case of arbitrary steady flow, the characteristic surface is no longer a cone. However, exactly as it was shown above, the characteristic surface cuts the streamlines at any point at the angle α.

One of the main differences between supersonic and subsonic flow is the possibility of a certain type of discontinuities in the flow, called *shock waves*. For example, from eq.(11.14) it follows that for certain functions $f(\varphi)$, which are determined by the particular boundary conditions of the problem in question, the curves $\varphi = \text{const}$ in the x–t plane intersect. Since the Riemann invariants as defined in eq.(11.10) are constant along these curves, with a different constant for each curve, it follows that for travelling waves the velocity v and the other hydrodynamical variables are multivalued. This is impossible in any physical circumstance and results in the creation of strong discontinuities (shock waves) on the flow.

Let us briefly discuss the classical limit of the different physical circumstances mentioned above. To do this, we make use of the relations presented in eq.(10.1) with $c \rightarrow \infty$ and, as it is usual in the classical case, we represent the speed of sound by c.

First of all, the speed of sound c is:

$$c = \left(\frac{\partial p}{\partial \rho} \right)_s^{1/2} . \tag{11.21}$$

The Riemann invariants $\mathcal{J}_{\pm}$ are constant along the curves $dx/dt = \pm(c \pm v)$. The dimensionless number M satisfies the following relation:

$$\frac{1}{M} = \sin\alpha \xrightarrow[c \rightarrow \infty]{} \frac{v}{c} \tag{11.22}$$

and is called in classical hydrodynamics the *Mach number.*[†]

The results obtained about the relativistic and classical Mach number M can be rewritten in the following way:

Theorem 1

The dimensionless Mach number M increases without limits as the velocity of the flow takes its maximum possible value. This maximum value is the speed of light in the relativistic case and infinity in the classical case. The Mach number tends to zero as the velocity of the flow vanishes, and tends to unity as the velocity of the flow tends to the velocity of sound. This Mach number is greater than one for supersonic flow and less than unity when the velocity of the flow is subsonic.

As a way to compare the difference between the classical and relativistic Mach numbers,

---

[†] The relativistic generalisation of the Mach number as presented in eq.(11.20) was first calculated by Chiu (1973). This was done by reducing the problem of steady relativistic gas dynamics to an equivalent Newtonian flow and by observing that the Mach number is a pseudoscalar. From eq.(11.20) it follows that this number, the *Chiu number* is in fact a definition of the *proper Mach number* since it is defined as the ratio of the three–relativistic velocity of the flow γv to the three–velocity of sound $\gamma_a a$ (Königl, 1980).

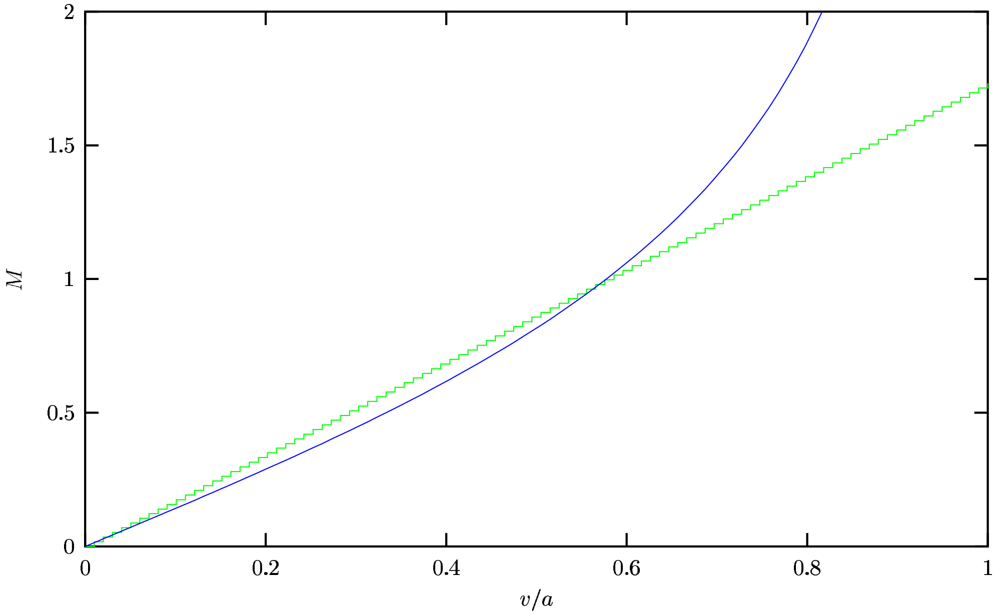

Figure II.3: Comparison between classical and relativistic Mach numbers. The green broken line is the classical Mach number and the blue continuous curve is its relativistic analogue. The intersection of both curves occurs when the Mach number in both cases is unity, that is when the velocity of the flow v is equal to the local velocity of sound. For the plot an ultrarelativistic equation of state was assumed for the gas, that is the velocity of sound $a = c/\sqrt{3}$.

a plot of both of them is presented in fig.(II.3). The intersection of both curves occurs for the case in which the Mach number tends to unity, that is when the velocity of the flows tend to the local velocity of sound according to Theorem 1. For the case of subsonic flow, the relativistic Mach number is less than its classical counterpart. However for supersonic flow the relativistic Mach number is greater than the classical one.

§12 Polytropic gases

In subsequent discussions we will consider gases with a particular behaviour in the way they change their thermodynamical quantities under quasi-statical processes. This gas, the so called *polytropic gas* was first introduced in thermodynamics by G. Zeuner (Chandrasekhar, 1958) and it is used extensively in Astrophysics.

A polytropic change on the thermodynamical quantities of a gas is said to occur if the change is done quasi-statical and is such that its specific heat remains constant during the entire process. From this definition it follows that (Chandrasekhar, 1958):

$$p \propto n^{\kappa}, \tag{12.1}$$

where the *polytropic index* κ is a constant and has a very well known value of 5/3 for an adiabatic mono atomic gas (Landau & Lifshitz, 1994b) in which relativistic effects are not taken into account. In the case of an ultrarelativistic photon gas it has a value of 4/3. The first law of thermodynamics, eq.(9.3), can be rewritten as (Stanyuokovich, 1960):

$$\frac{\mathrm{d}\ln e}{1+p/e} = \mathrm{d}\ln n. \tag{12.2}$$

The speed of sound a and the enthalpy per unit mass, *specific enthalpy*, w of a polytropic gas can then be written accordingly (Stanyuokovich, 1960):

$$a^2 = c^2 \frac{\kappa p}{e\,(1+p/e)}, \tag{12.3}$$

$$\frac{c^2}{w} = 1 - \frac{1}{\kappa - 1}\frac{a^2}{c^2}. \tag{12.4}$$

In the case of an ultrarelativistic gas, that is, when $p \sim e$ –for example, a photon gas in which $p = e/3$, it follows that (Stanyuokovich, 1960):

$$p = (\kappa - 1)\,e \tag{12.5}$$

$$a = \sqrt{\kappa - 1}\; c \tag{12.6}$$

For the case in which relativistic effects in the macroscopic motion of the gas are not considered, eqs.(12.3)-(12.4) become

$$c^2 = \kappa \frac{p}{\rho}, \tag{12.7}$$

$$w = \frac{\kappa}{\kappa - 1}\frac{p}{\rho}. \tag{12.8}$$

according to eq.(10.1).

§13 Shock waves in hydrodynamics

One of the most important physical phenomena that occur in supersonic flow is the existence of discontinuities in the different hydrodynamical quantities describing the flow. In order for the flow to possess such discontinuities, certain conditions have to be satisfied at the boundaries between the media. Mathematically, these boundaries are treated as infinitesimal, so that they may be assumed to be surfaces. For a steady flow, an element of area on a surface of discontinuity can be considered to be a plane and it can be assumed to be at rest by an appropriate choice of the system of reference. If the flow is not steady, then the argument remains valid for a short interval of time. In order to simplify the calculations, and without loss of generality, the surface of discontinuity can be chosen to be a plane which is parallel to the Oyz plane, so that the unit vector $\hat{e}_x$ in the positive x direction is normal to it.

Let us consider a closed three dimensional timelike cylinder S that intersects the surface of discontinuity. The axis of the cylinder is such that it is parallel to the normal to the plane of the surface of discontinuity, in the direction of the x axis. Integrating eq.(8.1) and eq.(9.1) along the volume enclosed by this hypersurface and using Gauss's theorem we obtain:

$$\oint \mathcal{T}^{i\alpha} df_\alpha = 0, \tag{13.1}$$

$$\oint n u^\alpha df_\alpha = 0. \tag{13.2}$$

with df_α the area element along the surface S. Taking the limit when the volume enclosed by the area S tends to zero gives:

$$[\mathcal{T}^{i1}] = 0, \qquad [nu^1] = 0. \tag{13.3}$$

where the difference between the values on either side of the discontinuity (sides 1 and 2) are represented by $q_1 - q_2 \equiv [q]$ for any quantity q. As we saw in section §8, $c\mathcal{T}^{0\alpha}$ represents the energy flux vector, diag$(\mathcal{T}_{\alpha\beta})$ is the 3–momentum flux density vector and nu^k is the particle flux 4–vector. From this it follows that the particle flux, the energy flux and the momentum flux vectors are conserved across the surface of discontinuity according to eq.(13.3):

$$[nu^x] = 0, \qquad [\mathcal{T}^{xx}] = [w(u^x)^2 + p] = 0, \qquad c[\mathcal{T}^{0x}] = c[\omega u^0 u^x] = 0, \tag{13.4}$$

and

$$[\mathcal{T}^{yx}] = [\omega u^x u^y] = 0, \qquad [\mathcal{T}^{zx}] = [\omega u^x u^z] = 0. \tag{13.5}$$

where x, y, and z are Cartesian coordinates. From eqs.(13.4)-(13.5) it follows that it is possible to define two types of discontinuities. In the first place, those in which there is no particle flux through the surface of discontinuity. That is, $n_1 u^x_1 = n_2 u^x_2 = 0$. Since the particle number densities on both sides of the discontinuity are non–zero it follows that the velocities $u^x_1 = u^x_2 = 0$. This satisfies identically all relations in eq.(13.5) as well as the first and third of eq.(13.4). The second relation in eq.(13.4) implies $[p] = 0$. That is, a discontinuity for which the mass flux through its surface is zero is such that its normal velocity components are zero and the pressure is continuous across it:

$$v_{x_1} = v_{x_2} = 0, \qquad [p] = 0. \tag{13.6}$$

The values of the other hydrodynamical quantities can take any value across this surface of discontinuity. A discontinuity of this kind is called a *tangential discontinuity.*[†]

The second type of discontinuity occur when the particle flux through the surface is non–zero. According to eqs.(13.4)-(13.5), this implies that the tangential component of the velocity is preserved across the surface of discontinuity:

$$[v_x] = 0, \qquad [v_y] = 0. \tag{13.7}$$

Such discontinuities are called *shock waves.* Substitution of the 4–velocity components in eq.(13.4) gives:

$$v_1\gamma_1/V_1 = v_2\gamma_2/V_2 \equiv j, \tag{13.8}$$

$$\omega_1 v_1^2\gamma_1^2/c^2 + p_1 = \omega_2 v_2^2\gamma_2^2/c^2 + p_2, \tag{13.9}$$

$$\omega_1 v_1\gamma_1^2 = \omega_2 v_2\gamma_2^2, \tag{13.10}$$

in which $V \equiv 1/n$ is the proper volume per particle number. From eq.(13.8) and eq.(13.10) it follows that the particle number flux j is given by:

$$j^2 = (p_2 - p_1)c^2/(\omega_1 V_1^2 - \omega_2 V_2^2). \tag{13.11}$$

Algebraic manipulation of eqs.(13.8)-(13.10) imply that (Taub, 1948; Landau & Lifshitz, 1995):

$$\omega_1^2 V_1 - \omega_2 V_2 + (p_2 - p_1)(\omega_1 V_1^2 + \omega_2 V_2^2) = 0, \tag{13.12}$$

which is called the *relativistic shock adiabatic* relation or *Taub adiabatic.* For a given p_1, V_1, the shock adiabatic gives a relation between p_2, V_2.

Writing $v/c = \tanh\varphi$, so that $\gamma = \cosh\varphi$, the velocities of the gas on either side of the discontinuity can be easily shown to be:

[†] In classical hydrodynamics tangential discontinuities are shown to be unstable and spread out to form a turbulent region. However, this stability arguments do not apply for the particular case in which the velocity of the flow is continuous across the surface of discontinuity. A tangential discontinuity with this properties is called a *contact discontinuity.*

$$\frac{v_1}{c} = \sqrt{\frac{(p_2 - p_1)(e_2 + p_1)}{(e_2 - e_1)(e_1 + p_2)}}, \qquad \frac{v_2}{c} = \sqrt{\frac{(p_2 - p_1)(e_1 + p_2)}{(e_2 - e_1)(e_2 + p_1)}}, \tag{13.13}$$

while their relative velocity is

$$v_{12} = \frac{v_1 - v_2}{1 - v_1 v_2 / c^2} = c\sqrt{\frac{(p_2 - p_1)(e_2 - e_1)}{(e_1 + p_2)(e_2 + p_1)}} \tag{13.14}$$

according to the relativistic rule for addition of velocities. The entropy density, as any other thermodynamic quantity, is discontinuous across a shock wave. From the law of the increase of the entropy it follows that the entropy can only increase across a shock wave. It is possible to show under very general arguments (Thorne, 1973; Landau & Lifshitz, 1995) that the shock wave is a *compression wave*, that is $p_2 > p_1$, if

$$\left(\partial^2(\omega V^2)/\partial p^2\right)_{\sigma V} > 0. \tag{13.15}$$

When $p_2 > p_1$ it follows from eqs.(13.8)-(13.10) that $V_1 > V_2$. Using the definition of the particle number flux in eq.(13.8), this implies that $v_1 > v_2$. In other words, provided that the inequality in eq.(13.15) is satisfied, then a shock wave satisfies:

$$p_2 > p_1, \qquad V_1 > V_2 \quad \text{and} \quad v_1 > v_2. \tag{13.16}$$

Very general arguments about the stability of shock waves (Landau & Lifshitz, 1995) show that, for any shock wave, whatever the thermodynamic conditions of the gas:

$$v_1 > a_1 \quad \text{and} \quad v_2 < a_2, \tag{13.17}$$

for a gas with sound speed a.

In order to derive the classical expressions of the relations written above, we take the limit $c \to \infty$ and use eq.(10.1). It is common practice in classical hydrodynamics to use the mass flux density j as opposed to the particle number density j, and the inverse of the mass density, the volume per unit mass $\mathcal{V}$, instead of the volume per unit particle V.

The mass density flux j is then given by:

$$j^2 = (p_2 - p_1)/(\mathcal{V}_1 - \mathcal{V}_2) = 0. \tag{13.18}$$

The shock adiabatic relation, also called Hugoniot adiabatic in classical fluid dynamics, is:

$$w_1 - w_2 + \frac{1}{2}(V_1 + V_2)(p_2 - p_1) = 0. \tag{13.19}$$

The velocity difference in eq.(13.14) gives:

$$v_1 - v_2 = \sqrt{(p_2 - p_1)(V_1 - V_2)}. \tag{13.20}$$

All the inequalities in eqs.(13.16)-(13.17) remain valid and that in eq.(13.15) becomes $(\partial^2 V/\partial p^2)_s > 0$.

§14 One-dimensional similarity flow

In this section we will discuss the one–dimensional non–steady gas flow under the assumption that there are characteristic velocities in the flow, but not characteristic lengths. To simplify the discussion we assume that relativistic effects are not taken into account.

The state of the flow at any time is defined by the characteristic velocity parameter and by some other parameters which describe the state of the gas, for example the pressure and density at an initial instant. With these parameters alone it is not possible to find a combination which has the dimensions of length or time. By applying the Π–Theorem of dimensional analysis (Sedov, 1993) it follows that the distribution of the different hydrodynamical quantities can only depend on the position x and time t through the ratio $x/t \equiv \xi$ only. In other words, if the lengths are measured in a unit that increases proportional with time, the pattern produced by the flow remains unchanged. Such a flow is called a *similarity flow* (Landau & Lifshitz, 1995).

Using the fact that all quantities in the problem depend only on the single variable ξ, for which $\partial/\partial x = (1/t)d/d\xi$ and $\partial/\partial t = -(\xi/t)d/d\xi$, we obtain from the equation of conservation of the entropy, eq.(10.4), $(v_x - \xi)s' = 0$. The prime denotes differentiation with respect to ξ. From this equation it follows that $s' = 0$, otherwise as it is obvious from the equations presented below in eq.(14.1) a contradiction will be obtained. This implies that the entropy $s = \text{const}$ and so, similarity flow in one dimension which is adiabatic must also be isentropic. In exactly the same way, the x and y components of Euler's equation imply that the velocity in the x and y components are constant and we can take them as zero by an appropriate choice of the system of reference.

The x component of Euler's equation, eq.(10.3), and the continuity equation eq.(10.2) can be written as:

$$(v-\xi)\rho' + \rho v' = 0, \tag{14.1}$$

$$(v-\xi)v' = -p'/\rho = -c^2\rho'/\rho. \tag{14.2}$$

Here v denotes the velocity in the x direction and we will use that convention in what follows. The trivial solution of this last set of equations is that of a uniform flow with $\rho = \text{const}$, $v = \text{const}$. The non–trivial solution is found by eliminating ρ' and v' from the equations, giving $(v-\xi)^2 = c^2$, so that $\xi = v \pm c$. We take the plus sign in the following discussion, which means that we have taken the direction of the positive x axis in a definite manner:

$$x/t = v + c \tag{14.3}$$

Substituting eq.(14.3) into eq.(14.1) we obtain $\rho \mathrm{d}v = c\mathrm{d}\rho$. In order to integrate this relation we recall that the velocity of sound is a function of the thermodynamical state of the gas. We can thus take this velocity as a function of the entropy and the mass density. Since the entropy is constant it follows that the velocity of sound can be considered as a function of the density only. In other words (Landau & Lifshitz, 1995):

$$v = \int c(\rho)\mathrm{d}\rho/\rho = \int \mathrm{d}p/c(\rho)\rho, \tag{14.4}$$

which can be rewritten as:

$$v = \int \sqrt{-\mathrm{d}p\mathrm{d}V}, \tag{14.5}$$

where the choice of the independent variable remains open.

Let us briefly discuss some general properties of the solution. Differentiating eq.(14.3) with respect to x gives:

$$t\frac{\partial\rho}{\partial x}\frac{\mathrm{d}(v+c)}{\mathrm{d}\rho} = 1. \tag{14.6}$$

The derivative of $v + c$ can be calculated from eq.(14.4) which gives:

$$\frac{\mathrm{d}(v+c)}{\mathrm{d}\rho} = \frac{c}{\rho} + \frac{\mathrm{d}c}{\mathrm{d}\rho} = \frac{1}{\rho}\mathrm{d}(\rho c)\mathrm{d}\rho,$$

and

$$\rho c = \rho\sqrt{(\partial p/\partial \rho)} = 1/\sqrt{-\partial V/\partial p}.$$

Differentiation of this relation results in:

$$d(\rho c)/d\rho = c^2 d(\rho c)/dp = \rho^3 c^5 (\partial^2 V/\partial p^2)_s/2,$$

so that eq.(14.6) takes the form:

$$d(\rho c)/d\rho = c^2 d(\rho c)/d\rho = \rho^2 c^5 (\partial^2 V/\partial p^2)_s/2 > 0. \tag{14.7}$$

Substitution of eq.(14.7) into eq.(14.6) implies that $\partial\rho/\partial x > 0$ for $t > 0$. Because $\partial p/\partial x = c^2 \partial p/\partial x$, it follows that $\partial p/\partial x > 0$. Also, since $\partial v/\partial x = (c/\rho)\partial\rho/\partial x$ according to eq.(14.4), the inequality $\partial v/\partial x > 0$ holds. In other words, we have proved that the following relations are valid in a flow for which eq.(14.3) holds:

$$\partial\rho/\partial x > 0, \qquad \partial p/\partial x > 0, \qquad \partial v/\partial x > 0. \tag{14.8}$$

In order to understand the meaning of these inequalities, let us rewrite them not as variations of the position x but as variations of the of time for a given fluid element as it moves. This variation is given by the total derivative of the corresponding quantity with respect to time. Thus, for the density it follows from the equation of continuity and eq.(14.8) that: $d\rho/dt = \partial\rho/\partial t + v\partial\rho/\partial x = -\rho\partial v/\partial x < 0$. This implies that $dp/dt = c^2 d\rho/dt < 0$ also. On the other hand, Euler's equation implies that $dv/dt < 0$. It is important to note that this last inequality does not mean that the magnitude of the velocity decreases as the fluid moves about, since v can be negative. We have proved that, as the fluid moves, the following inequalities are satisfied:

$$d\rho/dt < 0, \qquad dp/dt < 0, \qquad dv/dt < 0. \tag{14.9}$$

This means that, as the fluid moves, its pressure and density decreases. To put it differently, the gas is continuously rarefied as the fluid moves. Such a flow is called a *rarefaction wave*.

A rarefaction wave can only be propagated a finite distance along the x axis. This follows from the fact that $v \to \pm\infty$ as $x \to \pm\infty$. As a result, we can apply eq.(14.3) at the boundaries of a rarefaction wave. For this case, the ratio x/t is the velocity of the boundary relative to a fixed system of coordinates. The velocity relative to the flow itself is $x/t - v$ which is equal to the local velocity of sound c according to eq.(14.3). This result

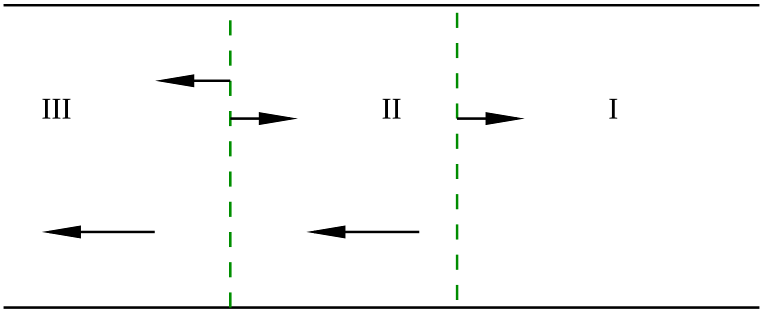

Figure II.4: Rarefaction wave (region II) bounded by two tangential discontinuities (dashed lines). The gas to the right of the rarefaction wave in region I has been chosen to be at rest. The arrows in the figure represent direction of motion of the flow and of the weak discontinuities.

implies that the boundaries of a rarefaction wave are *weak discontinuities.*[†]

The choice of sign in eq.(14.3) is now clear. It must be such that the weak discontinuities, bounding the rarefaction wave, are assumed to be moving in the positive x direction relative to the gas. By an appropriate choice of the system of reference we can choose the region, region I, to the right of the rarefaction wave to be at rest, as it is shown in fig.(II.4). Region II is the rarefaction wave and region III has gas moving with constant velocity. The arrows in the figure represent the direction of the flow and of the weak discontinuities. Due to the fact that the weak discontinuities move to the right relative to the gas, the weak discontinuity at the right of the diagram moves to the right. However, the weak discontinuity on the left might move in either direction. The direction depends on the value of the velocity reached in the rarefaction wave (Landau & Lifshitz, 1995).

For a polytropic gas eq.(14.4) gives:

$$v = \frac{2}{\gamma - 1} \int dc = \frac{2}{\gamma - 1}(c - c_0), \tag{14.10}$$

in which the constant of integration c_0 corresponds to the value of the velocity of sound when the velocity of the rarefaction wave vanishes. Here and in what follows we denote by the suffix 0 the region of the flow where the gas is at rest. Using the Poisson adiabatic for a polytropic gas, and rewriting eq.(14.10), we find that:

[†] Weak discontinuities are surfaces of discontinuities for which the hydrodynamical quantities, which are continuous across this surface, are not regular functions of the coordinates. This irregularity might be of various forms, for example the first spatial derivatives (or any other higher derivative) might be discontinuous across the surface or have an infinite value on it. These discontinuities are called weak as opposed to the strong ones (such as shock waves and tangential discontinuities) in which the hydrodynamical quantities themselves are discontinuous. Since the values of each hydrodynamical quantity are continuous across the surface of discontinuity, they can be "smoothed" by modifying them only near this surface and by very small amounts, in such a way that the smoothed functions lack of singularity. The true distribution of the pressure, say, can be represented as a superposition of a completely smoothed function p_0 and a very small perturbation p' near the weak discontinuity which contains the singularity. This perturbation, like any other perturbation in the flow, moves with the velocity of sound with respect to the gas.

$$c = c_0 - \frac{1}{2}(\gamma - 1)|v|, \tag{14.11}$$

$$\rho = \rho_0 \left\{ 1 - \frac{1}{2}(\gamma - 1)|v|/c_0 \right\}^{2/(\gamma-1)}, \tag{14.12}$$

$$p = p_0 \left\{ 1 - \frac{1}{2}(\gamma - 1)|v|/c_0 \right\}^{2\gamma/(\gamma-1)} \tag{14.13}$$

The value of the velocity as a function of the ratio x/t is obtained by substituting eq.(14.11) in eq.(14.3):

$$|v| = \frac{2}{\gamma + 1}\left(c_0 - x/t\right). \tag{14.14}$$

Lastly we mention that from eq.(14.11), since the velocity of sound is non negative, the following inequality has to be satisfied:

$$|v| \leq 2c_0/(\gamma - 1). \tag{14.15}$$

When the velocity reaches this limiting value, the pressure, density and velocity of sound in the gas become zero.

Chapter III

Jet–cloud interactions: bent jets

In section §5 various different mechanisms were described which can result in a considerable curvature of a radio jet in the plane of the sky as a result of kinetic effects of the host galaxy –*mirror symmetric* sources– or by the precession of the jets along a cone –*inversion symmetric* sources. Real hydrodynamic deflections can be caused either by the force produced by a wind of gas in a cluster of galaxies –*radio trails* sources– and also when the jet interacts with a stratified density region (such as a galaxy or a cloud). In this chapter, the physical mechanisms which produce the deflection of a jet which expands adiabatically are analysed. First of all, the case is discussed in which the velocities of the gas in the jet are non–relativistic and the jet interacts with an isothermal gas sphere and a cloud of gas which is in equilibrium with a dark matter halo. In both cases, the self gravity of the cloud is taken into account. The same calculations are repeated for the case in which the velocities of the gas inside the jet are relativistic. In this case, for simplicity, the self gravity of the corresponding stratified density region is not taken into consideration.

§15 Background to jet–cloud interactions

Jet–cloud interactions were first invoked to account for the sharp deflections observed in wide-angle tail (WAT) sources (Burns, 1986). Numerical simulations by de Young (1991) using the *beam scheme* (Sanders & Prendergast, 1974; de Young, 1986) showed that the jet can be considerably decelerated in a collision with the cloud. The cloud appears to be destroyed within a few million years and the jet adjusts itself in order to return to its original direction. The conclusion was that the interaction was not sufficiently long lived to produce a tail. Norman (1993) made a similar analysis using a *RIEMANN* code. He showed that a De Laval nozzle (see section §4) was formed which efficiently re–accelerated the jet in a different direction with respect to its original trajectory.

These contradictory results were reconciled by the 3D simulations performed by Higgins et al. (1999) using the *Godunov* method of Falle (1991). This reconciliation came about because in their models it was possible to vary two fundamental parameters: the Mach number of the jet and the density contrast η, defined as the ratio of the jet density to that of the environment. Higgins et al. were able to reproduce the structures shown by de Young using a fast, heavy jet model in their simulations (de Young used a Mach number $M \approx 25$ and a density contrast $\eta = 1$). On the other hand, for the case of light jets with low velocities, Higgins et al. reproduced the overall structure of the deflections shown by Norman (the simulations performed by Norman were for a jet with Mach number $M = 4$ and a density contrast $\eta = 0.2$).

§16 Initial stages of the interaction

The collision of a 2D Herbig–Haro jet with a cloud, in which the characteristic size of the cloud is much greater than the jet radius, has been studied in its initial stages by Raga & Cantó (1995). Their calculations were performed analytically and with a 2D numerical code. The analytical description of the problem was formulated as follows. Imagine a well collimated high Mach number flow (a *jet*) incident on a cold region of high density which is in pressure equilibrium with its surroundings (a *cloud*). Under the assumption that the jet radius is much smaller than the physical size of the cloud, the former can be thought as a plane parallel high density region. This assumption is essential for two reasons. First, the interaction of the jet with the cloud will result in a non significant disruption of the cloud, and second it allows a simple analytical formulation of the problem.

As shown in fig.(III.1), consider a jet which is incident onto a cloud at an angle θ to the plane of its surface. The interaction produces two shocks S_1 and S_2 which move with velocities v_1 and v_2 respectively.[†] The shock S_1 deflects the material in the jet to a direction parallel to the boundary of the cloud.

Under the assumption that shocks S_1 and S_2 are strong, and because the pressure in the region between shocks S_1 and S_2 has to be the same, then (Raga & Cantó, 1995):

$$v_2 = \sqrt{\frac{\rho_j}{\rho_c}}\, v_1, \tag{16.1}$$

where the uniform density of the cloud ρ_c is greater than that of the density of the jet ρ_j. Since $v_1 \leq v_j$ and $\rho_j \ll \rho_c$ it follows from eq.(16.1) that $v_2 \ll v_j$. In other words, for a very dense cloud, the shock S_2 moves into the cloud at very low velocities, causing the deformation of its boundary to occur very slowly. In the limit of very high cloud densities, it is safe to assume that the surface of the dense cloud effectively behaves as a rigid obstacle and its shape does not change as a result of the interaction (Raga & Cantó, 1995). This means that the jet is essentially interacting with a flat, rigid surface. The standard Rankine–Hugoniot conditions for a strong shock imply that the velocity of the jet after and before the collision are related to each other by:

[†] Shock S_1 is formed as a result of the interaction and is able to deflect the material of the jet at an angle α to the cloud. The high pressure behind this shock drives a secondary shock S_2 into the cloud.

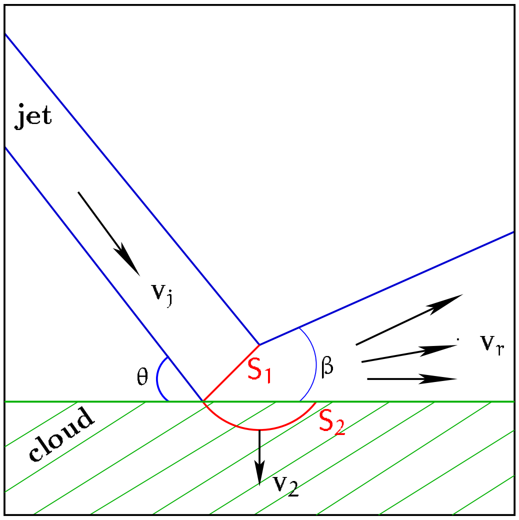

Figure III.1: Material within a jet travelling at velocity v_j collides with a dense obstacle, or cloud, which is in pressure equilibrium with its environment. The jet makes an angle θ with the tangent to the cloud before impact. The interaction produces two shocks S_1 and S_2, which move with velocities v_1 and v_2 respectively. The motion of S_2 through the cloud starts to drill a passage through it. The interaction produces a deflection of the jet making it curve at an angle β with respect to the cloud boundary. The velocity of the flow inside the reflected jet is v_r.

$$v_r \approx v_j \cos\theta, \tag{16.2}$$

as can be seen from the geometry of fig.(III.1). Eq.(16.2) means that the Mach number in the jet has decreased, and in fact, it is clear from that relation that a fraction $1 - \sin^2\theta$ of the initial kinetic energy of the jet is lost in the collision. The region behind the shock S_1 is highly overpressured and this means that the material moving away from the region where the collision occurred expands inside a Mach cone of angle β, which is given by (Cantó et al., 1988):

$$\sin\beta \approx \frac{2}{(\kappa - 1)\, M_j \cos\theta}, \tag{16.3}$$

where

$$M_j = v_j / c, \tag{16.4}$$

is the Mach number, c the speed of sound and κ the polytropic index of the flow inside the incident jet. In other words, the reflected beam looses collimation as a result of the interaction. This reduction on the collimation of the jet can be severe and could lead to a complete disruption of the jet beam. Indeed, from the conditions at the boundary of shock S_1 it follows that the angles β and θ are related to one another by the following relation (Cantó et al., 1988):

$$\tan\alpha = \frac{(1-\xi) - \sqrt{\left\{(1-\xi)^2 - 4\xi\tan^2\theta\right\}}}{2\tan\theta}. \tag{16.5}$$

and the inverse of the compression factor ξ is:

$$\xi = \frac{\kappa - 1}{\kappa + 1}, \tag{16.6}$$

This relation has a critical value when the angle $\theta \equiv \theta_c$. The critical angle θ_c is such that for $\theta > \theta_c$ no real solutions are found and its value is:

$$\tan\theta_c = \frac{(1-\xi)}{2\sqrt{\xi}} \qquad \text{and} \qquad \tan\alpha_c = \sqrt{\xi} \tag{16.7}$$

for a strong adiabatic shock. The critical angles in eq.(16.7) imply that for values of $\theta > \theta_c$, where:

$$\theta_c = \pi/2 - 2\alpha_c \tag{16.8}$$

the flow after the S_1 shock is subsonic (Cantó et al., 1988; Raga & Cantó, 1995). This means that the jet will not expand inside a Mach cone, but will escape from the region of the interaction between the jet and the cloud in all directions. In other words, a complete disruption to the jet has occurred.

For the case of Herbig–Haro jets in which the shock S_1 is isothermal, Raga & Cantó (1995) made 2D numerical simulations which show the overall structure mentioned with the very simple analytical arguments mentioned above. An example of their simulation is shown in fig.(III.2).

As a short summary, what all this means is that the initial stages of a jet–cloud interaction are determined by the incidence angle θ and by the cloud to jet density ratio. This ratio determines the velocity to which the jet begins to drill a hole into the dense cloud. Whatever the final steady configuration will be, it will certainly show a jet going through a passage made by the jet as a result of the collision. If the radius of the jet is considerably smaller than the characteristic size of the cloud, the drilling of the jet through the cloud will not cause a strong effect on the overall structure of the cloud.

Eventually, the jet–cloud collision will reach a steady state in which the jet penetrates the cloud at a certain position and travels through it inside a channel drilled as a result of the interaction. The trajectory of the jet is determined by the condition that the jet maintains pressure equilibrium with the surrounding environment. In other words, as the

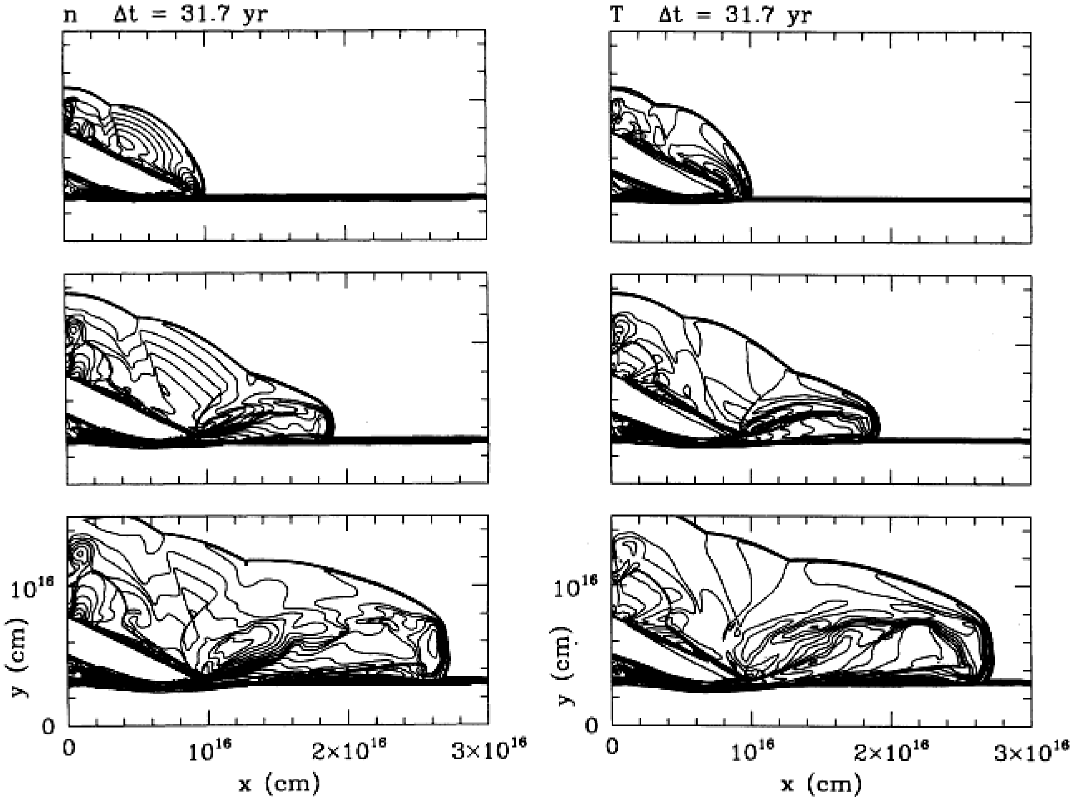

Figure III.2: Two dimensional time dependent numerical simulation of a Herbig–Haro jet by Raga & Cantó (1995). A jet directed at angle $\theta = 25^{\circ}$ towards the x–axis is injected from the left of the diagram. The cloud is in pressure equilibrium with its surroundings and its density is assumed to be 1000 times greater than the density of the incident jet. This simulations show the presence of a shock S_2 (see also fig.(III.1)) which starts to drill a hole into the cloud slowly. The initial velocity of the jet is $v_j = 100\,\mathrm{km\,s^{-1}}$, the particle number densities of the jet, external medium and cloud are 5, $0.5\,\mathrm{and}\,5 \times 10^2\,\mathrm{cm^{-3}}$ respectively. The temperatures of the corresponding regions is 1×10^3, 1×10^4 and $1\,\mathrm{K}$. Both diagrams show a time sequence of the particle number density (left) and temperature (right) stratification. The successive frames are taken at time intervals of 31.7 yr and the logarithmic contours correspond to factors of $\sqrt{2}$.

material in the jet moves, it adjusts its pressure in such a way that it is in equilibrium with the internal pressure of the cloud.

In what follows it will be assumed that this steady configuration has been achieved by the jet as it penetrates the cloud and that its expansion takes place adiabatically. The analysis will be carried out for cases in which the material in the jet moves at non–relativistic velocities and also when it expands relativistically. In order to compare with real astronomical objects, the structure of the cloud is modelled as an isothermal gas sphere (for collisions with hydrogen clouds, most probably in the interstellar medium) and also as gas which is in pressure equilibrium within a dark matter halo (for collisions with galaxies).

§17 Classical analysis

Once the steady state is reached, the jet penetrates the cloud and expands adiabatically. Because of this, the trajectory of the jet is determined by Euler's equation, eq.(10.6), which can be written as:

$$\hat{\boldsymbol{v}}\left(\boldsymbol{v}\cdot\mathbf{grad}\right)v+\mathsf{k}v^2\hat{\boldsymbol{n}}=-\mathbf{grad}\left(w+\phi\right), \tag{17.1}$$

where w and $\boldsymbol{v}$ represent the heat function per unit mass and the velocity of the flow inside the jet. The gravitational forces produced by the mass of the cloud in the moving jet is given by the gradients of the gravitational potential ϕ. The curvature k of the trajectory appears in the term which is proportional to its normal direction $\hat{\boldsymbol{n}}$. These two terms are proportional to the gradients of the unit tangent vector $\hat{\boldsymbol{v}}$ in the following way: $v\left(\boldsymbol{v}\cdot\mathbf{grad}\right)\hat{\boldsymbol{v}}=\mathsf{k}\hat{\boldsymbol{n}}$. From eq.(17.1) there are two equivalent ways of finding the required trajectory. The first is due to Icke (1991) and is as follows. Multiplying eq.(17.1) by the normal unit vector $\hat{\boldsymbol{n}}$ to the jet trajectory one finds:

$$\mathsf{k}v^2=\frac{v^2}{\mathsf{R}}=-\hat{\boldsymbol{n}}\cdot\mathbf{grad}\left(w+\phi\right), \tag{17.2}$$

where R is the radius of curvature to the trajectory. Eq.(17.2) simply means that the normal components of the gradients of the pressure in the jet (right hand side of that equation) have to balance the centrifugal acceleration produced by the curvature of the jet (left hand side of that equation).

The second method used to find the trajectory to the jet is due to Cantó & Raga (1996) and Raga & Cantó (1996). Instead of performing scalar multiplication of eq.(17.1) with a normal vector, contraction is carried out with a tangent vector $\hat{\boldsymbol{v}}$. This implies that $\hat{\boldsymbol{v}}\cdot\mathbf{grad}\,\left(v^2/2+w+\phi\right)=0$, that is, the path of the jet is described by Bernoulli's theorem eq.(10.7).

It is straightforward to show that if the flow in the jet is irrotational (as it is for the case we are going to consider, according to the results presented below), both relations, eq.(17.2) and Bernoulli's law are equivalent. For, if the vorticity is zero, then from the relation:

$$\boldsymbol{v}\times\mathbf{curl}\,\boldsymbol{v}=\frac{1}{2}\mathbf{grad}\,v^2-\boldsymbol{v}\cdot\mathbf{grad}\,\boldsymbol{v}$$

combined with Euler's equation, it follows that $\mathbf{grad}\,\left(v^2/2+w+\phi\right)=0$, which is a particular form of Bernoulli's law. Multiplication of this relation by the normal unit vector $\hat{\boldsymbol{n}}$ gives eq.(17.2). Since it is natural to work with energies, the approach by Cantó

& Raga (1996) and Raga & Cantó (1996) will be used in what follows.

Let us show now that under the conditions we have previously described, the trajectory of the jet is two dimensional. From Euler's equation, it follows that the left hand side of eq.(10.6) is simply the force per unit mass experienced by a fluid particle as it moves. Since all quantities in the right hand side of that equation depend only on the distance from the cloud's centre r, vector multiplication of the radius vector $\mathbf{r}$ with eq.(10.6) implies $\mathbf{r}\times \mathrm{d}\boldsymbol{v}/\mathrm{d}t=0$. In other words, the specific angular momentum $\mathbf{l}=\mathbf{r}\times\boldsymbol{v}$ is conserved as the fluid moves. Since the radius vector is perpendicular to the angular momentum vector, the motion is two dimensional, and so, polar coordinates (r, φ) are used in the following analysis.

Consider a situation in which the jet enters the cloud parallel to the x axis at a distance r_0, so that its velocity vector is initially given by:

$$\boldsymbol{v}_0 = -v_0\boldsymbol{e}_x = -v_0 \left(\cos\varphi_0\, \boldsymbol{e}_r - \sin\varphi_0\, \boldsymbol{e}_\varphi\right), \tag{17.3}$$

where $\boldsymbol{e}_x$, $\boldsymbol{e}_r$ and $\boldsymbol{e}_\varphi$ are unit vectors in the directions x, r and φ respectively. Because angular momentum is conserved and the motion is two dimensional, the velocity is most simply written using eq.(17.3) as:

$$\boldsymbol{v} = v_r\boldsymbol{e}_r + \frac{r_0}{r}v_0 \sin\varphi_0\, \boldsymbol{e}_\varphi, \tag{17.4}$$

in which $v_r = \mathrm{d}r/\mathrm{d}t$ represents the velocity in the radial direction.

Since the steady flow of the jet expands adiabatically, we can calculate the path of the jet by means of Bernoulli's equation, eq.(10.7):

$$\frac{1}{2}\int \mathrm{d}v^2 + \int \mathrm{d}w + \int \mathrm{d}\phi = 0, \tag{17.5}$$

in which the line integrals are taken from the initial position of a given fluid particle. The heat function per unit mass w of the flow in the jet is given by

$$w = \Gamma^{-1}p/\rho, \tag{17.6}$$

and

$$\Gamma \equiv (\kappa - 1)/\kappa \tag{17.7}$$

for a gas with polytropic index κ.

Substitution of eq.(17.4) and eq.(17.3) into the first integral of eq.(17.5) gives:

$$\int \mathrm{d}v^2 = \left\{ \frac{r_0}{r} \frac{v_0 \sin \varphi_0}{r} \frac{\mathrm{d}r}{\mathrm{d}\varphi} \right\}^2 + v_0^2 \left\{ \left(\frac{r_0}{r} \right)^2 \sin^2 \varphi_0 - 1 \right\}, \tag{17.8}$$

where we have used the fact that along the jet trajectory $\mathrm{d}r / v_r = r \mathrm{d}\varphi / v_\varphi$ (Landau & Lifshitz, 1995). Since the gas in the jet obeys a polytropic equation of state, we obtain for the second integral in eq.(17.5):

$$\int \mathrm{d}w = \frac{c_0^2}{\kappa \Gamma} \left\{ \left(\frac{p}{p_0} \right)^{\Gamma} - 1 \right\}, \tag{17.9}$$

in which c_0^2 is the initial sound speed of the jet material. The integral for the gravitational potential produced by the self-gravitating cloud is obtained from:

$$\int \mathrm{d}\phi = G \int \frac{M(r)}{r^2} \mathrm{d}r = 4\pi G \int \frac{\mathrm{d}r}{r^2} \int_0^r \xi^2 \rho_c(\xi) \, \mathrm{d}\xi, \tag{17.10}$$

where $M(r)$ and $\rho_c(r)$ represent the mass and density of the cloud at a distance r. Substitution of eqs.(17.8)-(17.10) into eq.(17.5) gives the relation followed by the path of the jet as it expands:

$$\begin{aligned} \frac{\mathrm{d}\eta}{\mathrm{d}\varphi} = \pm \frac{1}{\sin \varphi_0} \Bigg\{ & 1 - \eta^2 \sin^2 \varphi_0 - \frac{2}{\kappa \Gamma M_0^2} \left[\left(\frac{p}{p_0} \right)^{\Gamma} - 1 \right] - \\ & - \frac{8\pi G}{M_0^2 c_0^2} \int \frac{\mathrm{d}r}{r^2} \int_0^r \xi^2 \rho(\xi) \, \mathrm{d}\xi \Bigg\}^{1/2}, \end{aligned} \tag{17.11}$$

in which $\eta = r_0 / r$ and M_0 is the initial Mach number of the flow in the jet. The positive and negative signs for the value of the derivative $\mathrm{d}\eta / \mathrm{d}\varphi$ in eq.(17.11) have to be chosen with care. For example, if we consider the case in which no gravity and no pressure gradients are taken into account (i.e. last two terms on the right hand side of eq.(17.11) are zero, which corresponds to a straight trajectory) the derivative $\mathrm{d}\eta / \mathrm{d}\varphi < 0$ for $\eta_* < 1 / \sin \varphi_0$ and vice versa. The equality $\eta_* = 1 / \sin \varphi_0$ corresponds to the point for which a given fluid element in the jet reaches the y axis during its motion in this particular case.

In the limit of high initial supersonic motion ($M_0 \gg 1$) the third and fourth terms in the right hand side of eq.(17.11) are important only when $\eta = 1 / \sin \varphi_0$ and we can simplify eq.(17.11) by making an expansion about this point. Indeed, in general terms, if:

$$\left(\frac{p}{p_0}\right)^{\Gamma} = \alpha + \beta\eta\sin\varphi_0 + \zeta\eta^2\sin^2\varphi_0, \tag{17.12}$$

and

$$\phi - \phi_0 = 4\pi G\left(\tilde{\alpha} + \tilde{\beta}\eta\sin\varphi_0 + \tilde{\zeta}\eta^2\sin^2\varphi_0\right), \tag{17.13}$$

are the expansions of the pressure and gravitational potential respectively about $\eta = 1/\sin\varphi_0$, then eq.(17.11) takes the form:

$$\frac{d\eta}{d\varphi} = \pm\frac{1}{\sin\varphi_0}\left\{a + b\eta + e\eta^2\right\}^{1/2}, \tag{17.14}$$

in which:

$$\begin{aligned} a &\equiv 1 - \frac{2(\alpha - 1)}{\kappa\Gamma M_0^2} - \frac{8\pi G}{M_0^2 c_0^2}\tilde{\alpha}, \\ b &\equiv -\left(\frac{2\beta}{\kappa\Gamma M_0^2} + \frac{8\pi G}{M_0^2 c_0^2}\tilde{\beta}\right)\sin\varphi_0, \\ e &\equiv -\left(1 + \frac{2\zeta}{\kappa\Gamma M_0^2} + \frac{8\pi G}{M_0^2 c_0^2}\tilde{\zeta}\right)\sin^2\varphi_0, \end{aligned}$$

to second order in $\eta\sin\varphi_0$. For the cases considered below, the general solution of eq.(17.14) is (Gradshteyn & Ryzhik, 1994):

$$\eta = \frac{1}{2e}\left\{\sqrt{\Delta}\sin\left[\sqrt{-e}\left(\frac{\varphi_0 - \varphi}{\sin\varphi_0} + \frac{1}{\sqrt{-e}}\arcsin\frac{2e + b}{\sqrt{\Delta}}\right)\right] - b\right\}, \tag{17.15}$$

with $\Delta \equiv b^2 - 4ae$. The angle ψ subtended between the velocity vector of the jet streamline with the x coordinate axis on its way out of the cloud, the *deflection angle*, can be calculated from the relation $\tan\psi = (v_y/v_x)_{\text{exit}}$. In other words:

$$\psi = \arctan\left(\frac{\sin\varphi_e\,(d\eta/d\varphi)_e - \cos\varphi_e}{\cos\varphi_e\,(d\eta/d\varphi)_e + \sin\varphi_e}\right) + \pi, \tag{17.16}$$

where the subindex e labels the values of different quantities at the position where the jet exits the cloud. The exit azimuthal angle φ_e is given by:

$$\varphi_e = \varphi_0 + \frac{\sin\varphi_0}{\sqrt{-e}}\left\{2\arcsin\frac{2e + b}{\sqrt{\Delta}} + \pi\right\}, \tag{17.17}$$

for not very strong deflections. The derivative $(d\eta/d\varphi)_e$ is evaluated at $\eta = 1$, with a negative choice of sign in eq.(17.11).

§18 Isothermal cloud

Let us consider now the case of an isothermal cloud, for which the density in the cloud ρ_c varies as a function of the position r in the following way (Binney & Tremaine (1997)):

$$\rho_c = \frac{\xi}{r^2}. \tag{18.1}$$

where ξ is a constant of proportionality. In other words, because the jet and cloud are maintained in pressure balance, the pressure acting on the jet is given by:

$$\frac{p}{p_0} = \left(\frac{r_0}{r} \right)^2 . \tag{18.2}$$

For this isothermal case, it is easy to verify that the factors in the expansions for the gravitational potential ϕ and the pressure P as defined by eqs.(17.12)–(17.13) are given by:

$$\begin{aligned} \alpha &= \frac{1 - \Gamma(3 - 2\Gamma)}{\sin^{2\Gamma}\varphi_0}, & \tilde{\alpha} &= \xi \ln(\sin\varphi_0) + \frac{3}{2}\xi, \\ \beta &= \frac{4\Gamma(1-\Gamma)}{\sin^{2\Gamma}\varphi_0}, & \tilde{\beta} &= 2\xi, \\ \zeta &= \frac{\Gamma(2\Gamma - 1)}{\sin^{2\Gamma}\varphi_0}, & \tilde{\zeta} &= \frac{\xi}{2}. \end{aligned} \tag{18.3}$$

This solution corresponds to that found by Raga & Cantó (1996) for the case in which no gravity is present, i.e. $\tilde{\alpha} = \tilde{\beta} = \tilde{\zeta} = 0$. From the solutions obtained above in eq.(17.14) and eq.(18.3) it follows that the dimensionless parameter Λ defined as[†]:

$$\Lambda \equiv G \frac{\xi}{M_0^2 c_0^2} = G \frac{\rho_0 r_0^2}{M_0^2 c_0^2}. \tag{18.4}$$

is a number that parametrises the required solution.

The deflection of jets in isothermal clouds may be important for interstellar molecular clouds and the jets associated with Herbig-Haro objects. For this case we can obtain a

---

[†] The parameter Λ is an important number which can be obtained by dimensional analysis. For, the problem in question is characterised by the gravitational constant G, a "characteristic length" r_0 and the values of the velocity of the jet and the density at this point which are v_0 and ρ_0 respectively. Three independent dimensions (length, time and mass) describe the whole hydrodynamical problem. Since four independent physical quantities (G, ρ_0, v_0, and r_0) are fundamental for the problem we are interested, the Buckingham Π–Theorem (Sedov, 1993) of dimensional analysis demands the existence of only one dimensionless parameter Λ, which is given by eq.(18.4).

value for the parameter Λ . If we adopt a particle number density of $n_H \sim 10^2\,\mathrm{cm}^{-3}$, and a temperature $T \sim 10\,\mathrm{K}$ for a cloud with radius $r_0 \sim 1\,\mathrm{pc}$ (Spitzer, 1998; Hartmann, 1998), then

$$\Lambda \sim \frac{10^{-2}}{M_0^2} \left(\frac{r_0}{1\,\mathrm{pc}} \right)^2 \left(\frac{n_0}{10^2\,\mathrm{cm}^{-3}} \right) \left(\frac{T}{10\,\mathrm{K}} \right)^{-1} . \tag{18.5}$$

The same calculation can be made for the cases of radio jets interacting with the gas inside a cluster of galaxies. For this case, typical values are $n_H \sim 10^{-2}\,\mathrm{cm}^{-3}$, $T \sim 10^7\,\mathrm{K}$ and $r_0 \sim 100\,\mathrm{kpc}$ (Longair, 1992, 1998). With these values, the parameter $\Lambda \sim 10^{-2}/M_0^2$, exactly as eq.(18.5).

The fact that jets are formed in various environments such as giant molecular clouds and the gaseous haloes of clusters of galaxies with the same values of the dimensionless parameter Λ provides a clue as to why the jets look the same in such widely different environments.

From its definition, the parameter Λ can be rewritten as $\Lambda = (3/4\pi)(GM/r)(1/v_0^2)$, where M is the mass within a sphere of radius r_0. This quantity is roughly the ratio of the gravitational potential energy from the cloud acting on a fluid element of the jet, to its kinetic energy at the initial position r_0. The parameter Λ is thus an indicator of how large the deflections due to gravity are going to affect the trajectory of the jet. The bigger the number Λ, the more important the deflection caused by gravity will be. In other words, when the parameter $\Lambda \gg 1$ the jet becomes ballistic and bends towards the centre of the cloud. When $\Lambda \ll 1$ the deflections are dominated by the pressure gradients in the cloud and the jets bend away from the centre of the cloud.

Fig.(III.3) shows plots for three different values of Λ with initial Mach numbers of $M_0 = 5$ and $M_0 = 10$. A comparison with a numerical integration of eq.(17.14) using a fourth–order Runge–Kuta method is also presented in the figures by dashed lines. This comparison shows that as long as the deflections are sufficiently small, or as long as the Mach number of the flow in the jet is sufficiently large, the analytic approximations discussed above are a good approximation to the exact solution.

§19 Gas within a dark matter halo

Let us consider next the case of a galaxy dominated by a dark matter halo for which its density is given by the relation (Binney & Tremaine, 1997):

$$\rho_d = \frac{\rho_{d_\star}}{1 + (r/a)^2}, \tag{19.1}$$

in which a is the core radius and quantities with a star refer to the value at the centre of

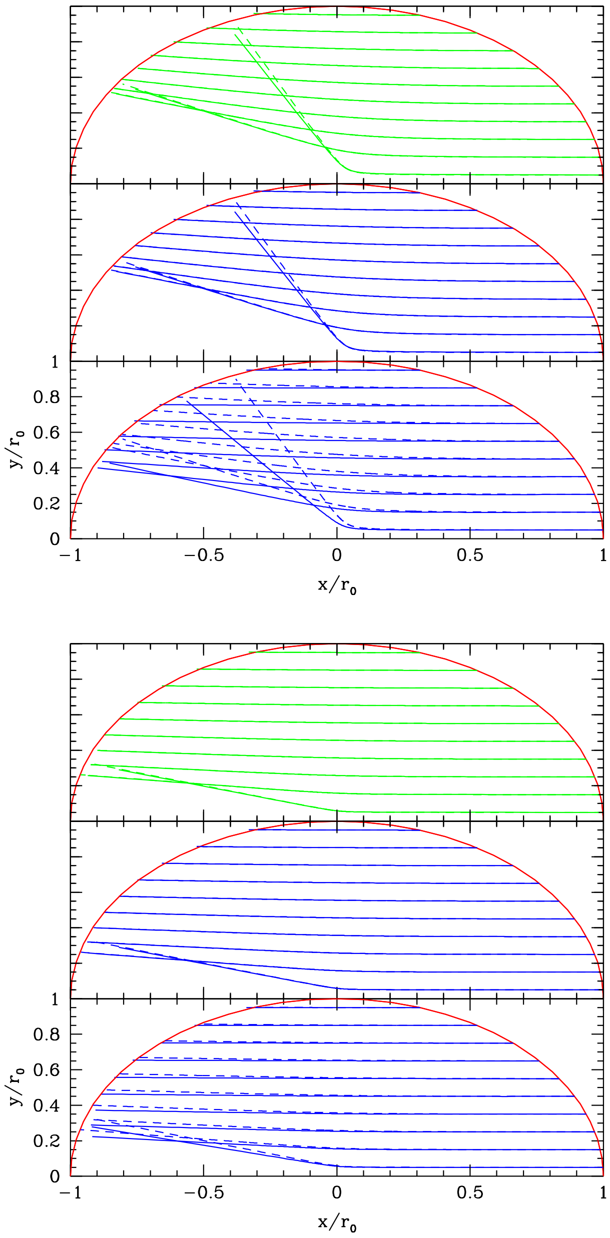

Figure III.3: Deflection produced in a jet due to the collision with an isothermal cloud (semicircle) of radius r_0. The jet penetrates the cloud from the right, parallel to the x axis. Different trajectories are shown in each diagram for different initial heights of $y/r_0 = 0.05$, $0.15, \ldots, 0.95$ as measured from the x/r_0 axis. In each figure the top diagram corresponds to the case in which gravitational effects are not considered (Raga & Cantó, 1996). The middle and bottom diagrams represent trajectories for which gravitational effects are taken into account and the parameter Λ has values of 10^{-6}, 0.01 respectively in units of the square of the initial Mach number M_0^2 of the jet (see text). For the plots, a polytropic index $\kappa = 5/3$ for the flow in the jet was assumed. The diagrams at the top and bottom correspond to initial Mach numbers for the jet flow $M_0 = 5$ and $M_0 = 10$ respectively. The dashed lines in the graphs represent the direct numerical integration of the equation of motion. The continuous lines are the analytic approximations discussed in the text.

the galaxy.

The potential resulting from such a density profile can be calculated by means of eq.(17.10),

$$\phi_d - \phi_{d_\star} = 4\pi G \rho_{d_\star} a^2 \left\{ \frac{1}{2} \ln \left[1 + \left(\frac{r}{a} \right)^2 \right] + \frac{a}{r} \arctan \left(\frac{r}{a} \right) - 1 \right\}, \tag{19.2}$$

in which the value of the gravitational potential $\phi_{d_\star}$ has been evaluated at the centre of the galaxy $r_\star = 0$. If the gas in the galaxy is in hydrostatic equilibrium with the dark matter halo, then $\mathbf{grad}\, p = -\rho\, \mathbf{grad}\, \phi_d$. In this case, the enthalpy of the isothermal gas is given by:

$$w - w_\star = -\phi_d + \phi_{d_\star} = c_\star^2 \ln \left(\frac{p}{p_\star} \right), \tag{19.3}$$

and so the pressure takes the value:

$$p = p_\star \, \exp \left\{ \left(-\phi_d + \phi_{d_\star} \right) / c_0^2 \right\}. \tag{19.4}$$

It is possible to simplify the above expressions by using the fact that for astronomical cases $r_0 \gg a$. In other words:

$$\frac{p}{p_0} = \eta^{-k}, \tag{19.5}$$

where the dimensionless parameter k is given by[†]:

$$k \equiv -4\pi G \frac{\rho_{d_\star} a^2}{c_\star^2}. \tag{19.6}$$

Adopting these approximations, the required analytic solutions can be found:

$$\begin{aligned} \alpha &= \frac{1}{2} \left(k\Gamma + 1 \right) \left(k\Gamma + 2 \right) \sin^{k\Gamma} \varphi_0, \\ \beta &= -k\Gamma \left(2 + k\Gamma \right) \sin^{k\Gamma} \varphi_0, \\ \zeta &= \frac{1}{2} k\Gamma \left(k\Gamma + 1 \right) \sin^{k\Gamma} \varphi_0, \end{aligned} \tag{19.7}$$

where for simplicity it was assumed that $\tilde{\alpha} = \tilde{\beta} = \tilde{\zeta} = 0$. In other words, the gravitational

---

[†] In exactly the same form as it was done in the footnote of p.52, the dimensionless parameter k (apart from an unimportant proportionality factor of -4π) can be calculated by standard dimensional analysis. In this case the important parameters in the problem are the gravitational constant G, the characteristic length a and the sound speed $c_\star$ together with the density $\rho_\star$ evaluated at the centre of the cloud.

field induced by the mass of the cloud has been neglected. Using typical values (Binney & Tremaine, 1997) for galaxies then $\rho_\star \sim 0.1\,\mathrm{M}_\odot\,\mathrm{pc}^{-3}$, $a \sim 1\,\mathrm{kpc}$. Taking central values for the gas in the galaxy as $n_\star \sim 1\,\mathrm{cm}^{-3}$ and $T_\star \sim 10^5\,\mathrm{K}$ then $k \sim -10$. Fig.(III.4) shows plots for different values of M_0 and k.

The number k can be rewritten as $k = -\left(4/(4-\pi)\right)(GM/a)(1/c_\star^2)$, where M is the mass of a sphere with radius a. This quantity is proportional to the gravitational energy of the cloud evaluated at the core radius divided by the sonic kinetic energy that a fluid element in the jet has. In other words, in the same way as in Section §18, the dimensionless number k is an indicator as to how big deflections produced by gravity are.

§20 Relativistic analysis

Let us consider the case in which relativistic effects are included in the collision between a relativistic jet and a stratified high density region. In order to simplify the problem, the self gravity of the cloud acting on the jet is ignored. For this case, the relativistic generalisation of Euler's equation is given by eq.(9.6), in which ω and p are the enthalpy per unit volume and the pressure of a given fluid particle in its proper frame of reference respectively. The speed of light is c and γ is the standard Lorentz factor.

The arguments used to prove the conservation of the angular momentum of the jet in section §17 can be generalised for the relativistic case in the following way. The term in brackets in the left hand side of eq.(9.6) represents the classical force per unit mass acting on an element of fluid as it moves. By considering steady flow and because the pressure depends only on the radial coordinate r, vector multiplication of the radius vector $\mathbf{r}$ with eq.(9.6) shows that the quantity $\mathbf{l} = \mathbf{r} \times \boldsymbol{v}$ is conserved during the motion of the fluid. This quantity corresponds to the specific angular momentum in classical mechanics, but is not its relativistic counterpart, which is given by $\mathbf{r} \times \gamma \boldsymbol{v}$. The constancy of $\mathbf{l}$ implies that motion is two dimensional and so eqs.(17.3)-(17.4) are valid in the relativistic case as well.

Multiplication of eq.(9.6) by the unit tangent vector $\hat{\boldsymbol{v}}$ for steady adiabatic flow, shows that the trajectory of the jet is described by Bernoulli's law (eq.(9.7)):

$$\int \mathrm{d}\left(\frac{\gamma w}{n}\right) = 0. \tag{20.1}$$

The line integral is taken from the initial position of a given fluid particle to its final position. The particle number per unit proper volume is n and we assume that the electrons in the jet are ultrarelativistic, so that the equation of state is given by $p = e/3$ with e being the internal energy density of the plasma. The requirement that the pressure of the jet equals that of the cloud, together with the fact that $p \propto n^{4/3}$, makes it possible to integrate eq.(20.1) giving:

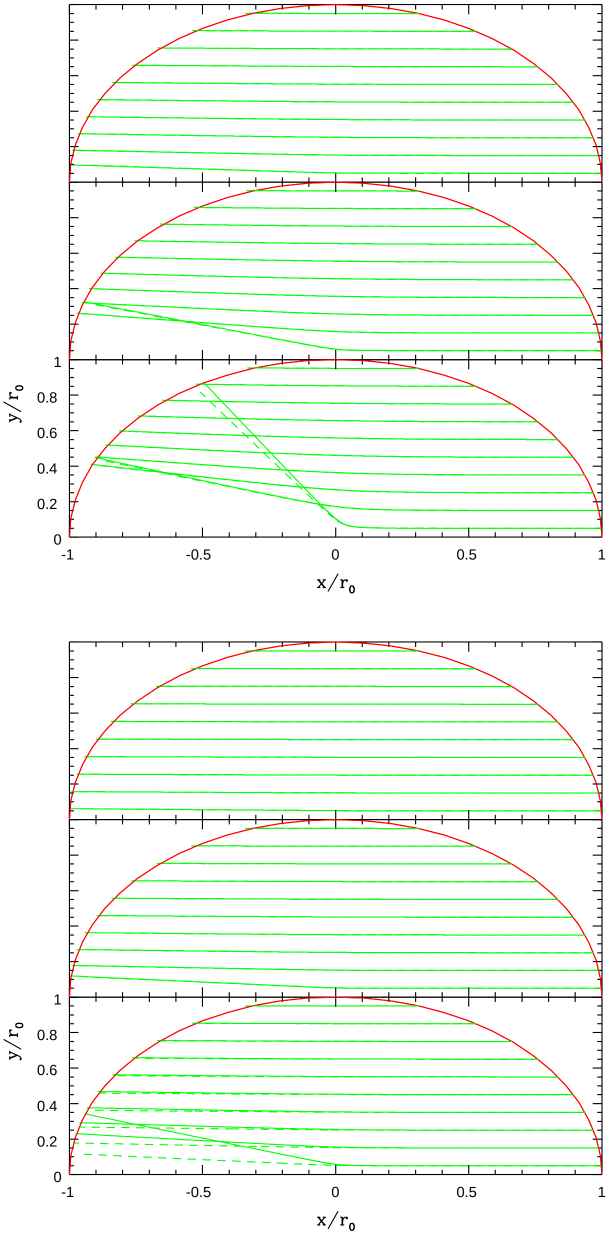

Figure III.4: Deflection produced in a jet as it travels across a galaxy, for which its gravitational potential is dominated by a dark matter halo. The jet penetrates the galaxy parallel to the x/r_0 axis. Various trajectories are shown in each diagram for different initial heights $y/r_0 = 0.5$, $0.15, \ldots, 0.95$ measured from the x/r_0 axis. The top and bottom diagrams were calculated for the case of a non relativistic jet with an initial Mach number of $M_0 = 10$ and $M_0 = 20$ respectively. For each of this diagrams a value of $k = -1$, -2, -3 was used for the top, middle and bottom panels respectively (see text). The dashed lines in the figures represent the direct numerical integration of eq.(17.14) with the pressure given by eq.(19.4) for the case in which the ratio of the core radius a to the initial radius r_0 is given by $a/r_0 = 10^{-3} \ll 1$. The continuous lines are analytic approximations found under this conditions.

$$\frac{d\eta}{d\varphi} = \pm \frac{c}{v_0 \sin\varphi_0} \left\{ 1 - \frac{v_0^2}{c^2}\eta^2 \sin^2\varphi_0 - \gamma_0^{-2} \left(\frac{p}{p_0} \right)^{1/2} \right\}^{1/2}, \tag{20.2}$$

in which $\eta \equiv r_0/r$. The sign of $d\eta/d\varphi$ in eq.(20.2) varies as the jet crosses the cloud. For example, for the ultrarelativistic case, in which a straight trajectory is expected, it is positive for $\eta_* > 1/\sin\varphi_0$, and negative when the inequality is inverted. A general analytic solution of eq.(20.2) can be found because, for high relativistic velocities, the third term on the right hand side of eq.(20.2) is important only for $\eta = 1/\sin\varphi_0$. In other words, the pressure stratification of the cloud can be written as eq.(17.12) with the substitution $\Gamma \rightarrow 1/2$. We can therefore expand eq.(20.2) about $\eta = 1/\sin\varphi_0$ to obtain a relation like eq.(17.14) but with:

$$\begin{aligned} a &= 1 - \frac{\alpha}{\gamma_0^2}, \\ b &= -\frac{\beta}{\gamma_0^2}\sin\varphi_0, \\ e &= -\left(\frac{\zeta}{\gamma^2} + 1 \right)\sin^2\varphi_0. \end{aligned} \tag{20.3}$$

§21 Isothermal cloud and dark matter halo

As in section §18, consider the case of an isothermal cloud being penetrated by the jet. In this case, it is possible to find an exact solution to the problem, since eq.(18.2) and eq.(20.2) can be used to show that:

$$\frac{d\eta}{d\varphi} = \pm \frac{1}{\sin\varphi_0} \left\{ \frac{c^2}{v_0^2}\left(1 - \eta\gamma_0^{-2} \right) - \eta^2 \sin^2\varphi_0 \right\}^{1/2}. \tag{21.1}$$

In other words, the solution is the same as that already found in eq.(17.14) and eq.(17.15) but with:

$$a = \left(\frac{c}{v_0} \right)^2, \qquad b = -\left(\frac{c}{v_0} \right)^2 \gamma^{-2}, \qquad e = -\sin^2\varphi_0. \tag{21.2}$$

Fig.(III.5) shows plots of the trajectory of the jet for different values of its initial velocity.

Let us now consider the case in which the gas in a galaxy is in hydrostatic equilibrium with a dark matter halo. As it was shown in section §19, for $r_0 \gg a$, the variation of the pressure in the galaxy is given by eq.(19.5) and the trajectory of the path of the jet is given by eq.(17.14) and eq.(17.15) together with eq.(19.7) and the substitution $\Gamma \rightarrow 1/2$. Fig.(III.6) shows plots of this for $k = -3$ and different values of the initial velocity of the

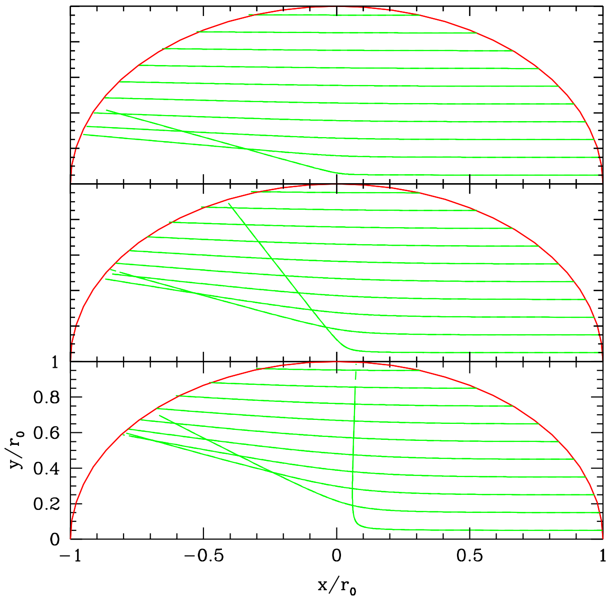

Figure III.5: Deflection of a relativistic jet produced by its collision with an isothermal cloud (semicircle). The jet is assumed to travel parallel to the x axis at the moment it enters the cloud from the right. In each plot different trajectories are shown for different values of the initial height of the jet $y/r_0 = 0.05$, $0.15, \dots, 0.95$ as measured from the x/r_0 axis. The top, middle and bottom panel plots were calculated for values of the initial velocity of the jet v_0 in units of the speed of light c of 0.99, 0.97, 0.95 respectively.

jet v_0.

§22 Discussion

Once an observed deflection is given, it is possible to work backwards and find useful properties concerning the initial interaction of a jet with a stratified density region. For example, by taking the "standard" values mentioned in sections §18 and §19 for the pressure and density in the stratified gas it is possible to calculate the initial azimuthal angle φ_0 for a given initial velocity of the jet. In order to illustrate this, consider eq.(17.16) and eq.(17.17). Because the derivative $(d\eta/d\varphi)_e$ has a negative value at the point at which the jet leaves the cloud, it is possible to find the value of the deflection angle $\cos\psi$. This angle is a function of the velocity of the jet v_0 and the initial azimuthal angle φ_0. To visualise this, an example is shown in fig.(III.7) for the case in which a relativistic jet interacts with an isothermal cloud. The contour levels for which $\cos\psi = \text{const}$ give the required relation between the initial velocity and azimuthal angle. Fig.(III.8) shows two examples of these contours.

Different combinations of the various parameters involved (or the known observables) in the problem can be assumed so that, for a given deflection, the other quantities can be calculated. For instance one can ask for the values of the central density of the gas in the

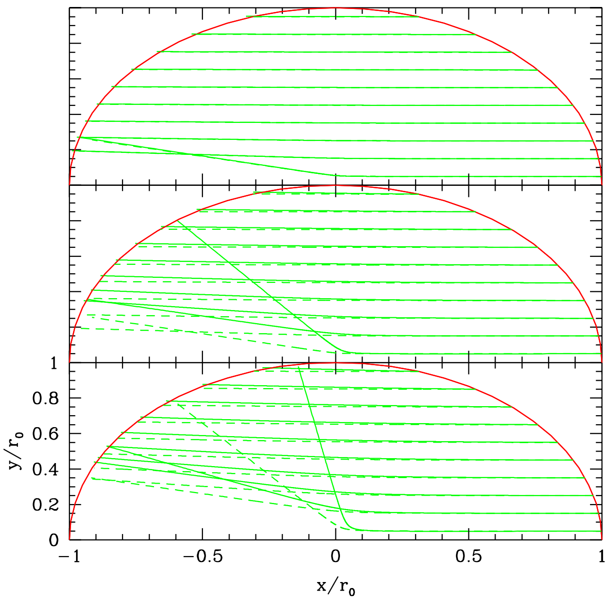

Figure III.6: Trajectory of a relativistic jet as it crosses a galaxy. The gas in the galaxy is assumed to be in hydrostatic equilibrium with a gravitational potential given by a dark matter halo in the galaxy. It is assumed that the jet enters the galaxy parallel to the x axis at a height of $y/r_0 = 0.05, 0.15, \ldots, 0.95$ in different cases. The plots were calculated for the case in which the parameter $k = -3$ and the initial velocity of the jet in units of the speed of light is 0.999, 0.995 and 0.99 from top to bottom. Continuous lines are analytic approximations to the problem and dashed ones are direct numerical solutions.

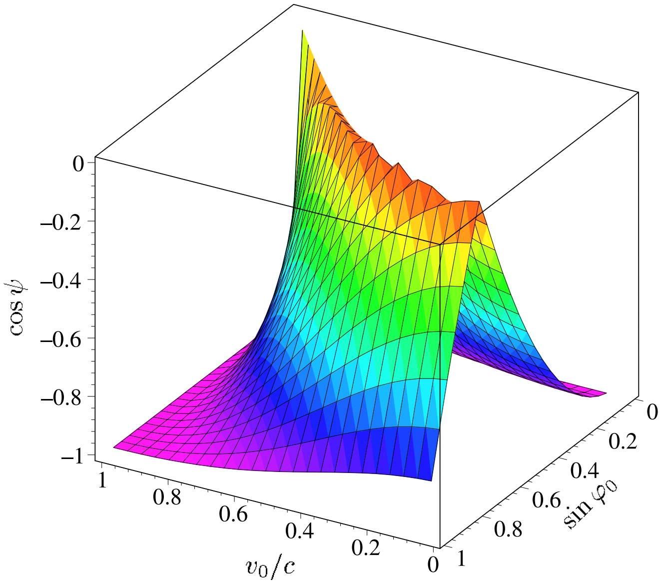

Figure III.7: Three dimensional plot showing the variations of the deflection angle ψ which is defined as the azimuthal angle the velocity of the flow makes with the x axis at the moment it leaves the cloud. The deflection angle is a function of the initial velocity of the jet v_0 and the initial azimuthal angle φ_0. The plot was produced for the case in which a relativistic jet interacts with an isothermal cloud.

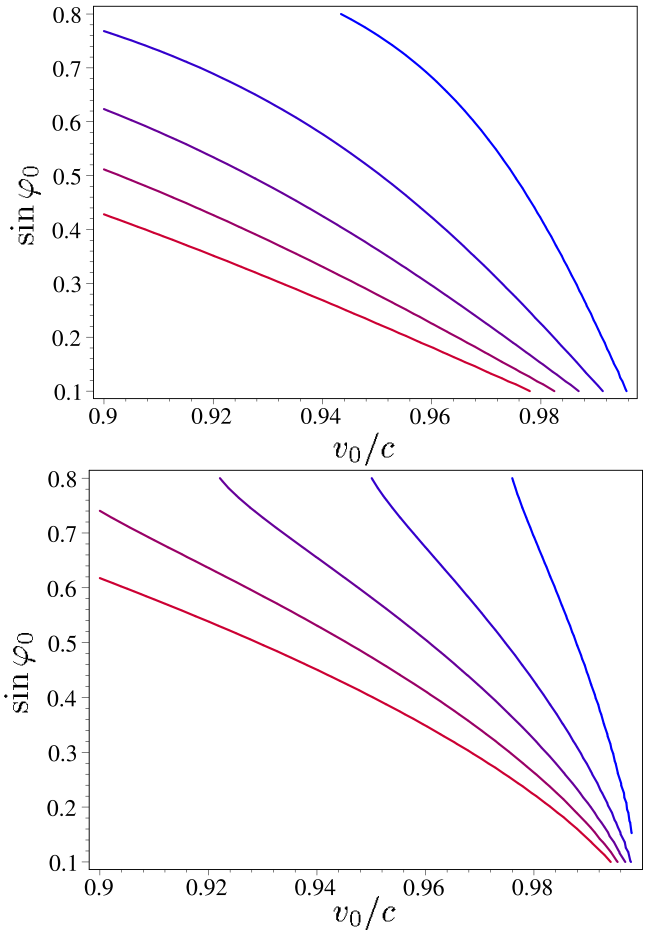

Figure III.8: Variations of initial azimuthal angle φ_0 as a function of velocity v_0 in units of the speed of light c for constant values of the deflection angle ψ. The angle ψ is the azimuthal angle the velocity vector of the flow in the jet makes with the x axis at the moment it leaves the cloud. Every plot was calculated for $\cos\psi = \text{const}$ with values of ψ given by $175\,°$, $170\,°, \ldots, 155\,°$. The gradient of ψ decreases towards the lower left part of each diagram. In other words, deflections become stronger as the curves approach this region on the diagram. An isothermal sphere and an isothermal gas in hydrostatic equilibrium with a dark matter halo were assumed for the top and bottom diagrams respectively in the case of a relativistic jet.

cloud, the density in the jet, etc.

The most important consequence of the calculations presented in this chapter is the sensitivity of the deflection angles to variations in velocity –see for example fig.(III.8). This sensitivity is due to the fact that the force applied to a given fluid element in the jet (due to pressure and gravitational potential gradients) is the same independent of the velocity of the flow in the jet. However, as the velocity of the flow in the jet increases, there is not enough time for this force to change the curvature of the jet soon enough, giving rise to very straight jets.

Chapter IV

Stability of non-straight jets

In section §5, we discussed the possible mechanisms which directly affect the shape of a jet. However, these mechanisms may not last for a long time and may result in instabilities. The most obvious problem would be if the collimation of the jet were no longer achieved efficiently. This occurs when the Mach number of the flow decreases to such an extent that it becomes subsonic. The most natural way of making a supersonic flow to become subsonic is through the creation of a strong discontinuity in the hydrodynamical quantities, that is, through a shock wave.

When a jet bends it is naturally in direct contact with its surroundings and entrainment from the external gas might cause disruption to its structure (Icke, 1991). However, if that problem is bypassed, for example, by an efficient cooling, there remains a high Mach number collimated flow within a curved jet. When a supersonic flow bends, the characteristics emanating from it tend to intersect at a certain point in space (Landau & Lifshitz, 1995; Courant & Friedrichs, 1976). Since the hydrodynamical values of the flow along non–parallel characteristic lines have different constant values, this intersection causes the different values of these quantities to be multivalued. This situation cannot occur in nature and a shock wave is formed to overcome this problem.

The formation of internal shocks inside the jet is potentially extremely dangerous since the flow behind the shock is subsonic and collimation is no longer possible. If the characteristics intersect outside the jet, then a shock wave is not formed and it seems that in this case the jet can survive a bending. However, as will be shown in this chapter, the Mach number decreases in a bend and the rate of change of the Mach angle with respect to the bending angle, defined as the angle the jet makes with its original straight trajectory, increases without bounds as the Mach number tends to unity. This means that there is a stage in which the Mach angle increases faster than the bending angle. This causes the characteristics in the jet to intersect and form a terminal shock. The aim of this chapter is to investigate these physical mechanisms, in particular, to investigate the formation of internal shocks in the structure of a jet.

§23 Prandtl–Meyer flow

Let us describe briefly the exact solution of the equations of hydrodynamics for plane steady flow depending on one angular variable ϕ only. This problem was first investigated by Prandtl and Meyer in 1908 (Landau & Lifshitz, 1995; Courant & Friedrichs, 1976) for the case in which relativistic effects were not taken into account. The full relativistic solution to the problem is due to Kolosnitsyn & Stanyukovich (1984).

For this case, Euler's equation, eq.(9.5) and the continuity equation, eq.(9.1) can be written:

$$v_\phi = \frac{\mathrm{d} v_r}{\mathrm{d}\phi}, \tag{23.1}$$

$$v_r n \gamma + \frac{\mathrm{d}\left(v_\phi n \gamma\right)}{\mathrm{d}\phi} = 0, \tag{23.2}$$

$$\omega\gamma/n = \text{const}, \tag{23.3}$$

where v_r and v_ϕ are the components of the velocity in the radial and azimuthal directions respectively. Eq.(23.3) is the Bernoulli equation, eq.(9.7), for this problem.

Using the definition of the speed of sound, eq.(11.3), in eq.(23.2) with the aid of eq.(23.3) it is found that:

$$v_r + \frac{\mathrm{d} v_\phi}{\mathrm{d}\phi} + v_\phi \left(1 - \frac{a^2}{c^2}\right) \frac{c^2}{a^2} \frac{\mathrm{d}}{\mathrm{d}\phi} \ln\left(\omega/n\right) = 0. \tag{23.4}$$

On the other hand, differentiation of γ^{-2} with respect to the azimuthal angle ϕ and using eq.(23.3), gives:

$$v_\phi \left(v_r + \frac{\mathrm{d} v_\phi}{\mathrm{d}\phi}\right) + c^2 \left(1 - \frac{v_r^2 + v_\phi^2}{c^2}\right) \frac{\mathrm{d}}{\mathrm{d}\phi} \ln\left(\omega/n\right) = 0. \tag{23.5}$$

Multiplication of eq.(23.4) by v_ϕ and substracting this from eq.(23.5) gives:

$$v_\phi^2 = a^2 \left(1 - \frac{v_r^2}{c^2}\right). \tag{23.6}$$

On the other hand, Bernoulli's equation, eq.(23.3), together with the value of the specific enthalpy for a polytropic gas given in eq.(12.4), can be rewritten

$$\left(1 - \frac{v_r^2 + v_\phi^2}{c^2}\right) \left(1 - \frac{1}{\kappa - 1} \frac{a^2}{c^2}\right)^2 = \left(1 - \frac{1}{\kappa - 1} \frac{a_0^2}{c^2}\right)^2, \tag{23.7}$$

in which it has been assumed that at some definite point, the flow velocity vanishes and the speed of sound has a value a_0 there. It is always possible to make the velocity zero at a certain point by a suitable choice of the system of reference.

Eqs.(23.6)-(23.7) can be solved in terms of v_r and v_ϕ:

$$v_r^2/c^2 = 1 - F^2(a), \tag{23.8}$$

$$v_\phi^2 = a^2 F^2(a), \tag{23.9}$$

where

$$F^2(a) = \left(1 - \frac{1}{\kappa - 1}\frac{a_0^2}{c^2}\right)^2 \left(1 - \frac{a^2}{c^2}\right)^{-1} \left(1 - \frac{1}{\kappa - 1}\frac{a^2}{c^2}\right)^{-2}. \tag{23.10}$$

Because $v_r dv_r = c^2 F(a) F'(a) da$, eq.(23.1) gives the required solution (Kolosnitsyn & Stanyukovich, 1984):

$$\phi + \phi_0 = \pm c \int \frac{F'(a)da}{a\sqrt{1 - F^2(a)}}. \tag{23.11}$$

This equation gives the speed of sound as a function of the azimuthal angle. From eqs.(23.8)-(23.9) it follows that the radial and azimuthal velocities can be obtained as a function of the same angle ϕ. Because of this, all the remaining hydrodynamical variables can be found. The sign in eq.(23.11) can be chosen to be negative by measuring the angle ϕ in the appropriate direction and we will do that in what follows.

Let us consider now the case of an ultrarelativistic gas and integrate eq.(23.11) by parts, to obtain:

$$\phi + \phi_0 = \frac{c}{a} \arccos F(a) + c \int \frac{da}{a^2} \arccos F(a). \tag{23.12}$$

For the case of an ultrarelativistic gas, the speed of sound a is given by eq.(12.6). In other words, this velocity is constant and so the integral in eq.(23.12) is a Lebesgue integral. Since this integral is taken over a bounded and measurable function over a set of measure zero, its value is zero.

Using eqs.(23.8)-(23.9) and eq.(23.12) the desired solution is obtained (Kolosnitsyn & Stanyukovich, 1984; Königl, 1980):

$$v_r = c \sin\left\{\sqrt{\kappa - 1}\,(\phi + \phi_0)\right\}, \tag{23.13}$$

$$v_\phi = \sqrt{\kappa - 1}\; c \cos\left\{\sqrt{\kappa - 1}\,(\phi + \phi_0)\right\}, \tag{23.14}$$

for an ultrarelativistic equation of state of the gas.

For the classical case, in which $c \to \infty$, eq.(23.11) gives for a polytropic gas with polytropic index κ:

$$\phi + \phi_0 = -\sqrt{\frac{\kappa+1}{\kappa-1}} \int \frac{d\zeta}{\sqrt{1-\zeta^2}},$$

where

$$\zeta \equiv \frac{a}{c} \sqrt{\frac{\kappa+1}{\kappa-1}} \left\{ 1 - \left(1 - \frac{1}{\kappa-1} \frac{a_0^2}{c^2} \right)^2 \right\}^{-1/2},$$

and so, the required solution is (Kolosnitsyn & Stanyukovich, 1984):

$$\phi + \phi_0 = \sqrt{\frac{\kappa+1}{\kappa-1}} \arccos \left(\frac{c}{c_*} \right), \tag{23.15}$$

where the speed of sound a has been rewritten as c to be consistent in the non–relativistic case. The *critical velocity of sound* c_* is given by (Landau & Lifshitz, 1995):

$$c_*^2 = \frac{2}{\kappa+1} c_0^2. \tag{23.16}$$

The value for the velocities can thus be calculated from eq.(23.1) and eq.(23.9) with $F(a) = 1$:

$$v_r = \sqrt{\frac{\kappa+1}{\kappa-1}} c_* \sin \sqrt{\frac{\kappa-1}{\kappa+1}} \left(\phi - \phi_0 \right), \tag{23.17}$$

$$v_\phi = c = c_* \cos \sqrt{\frac{\kappa-1}{\kappa+1}} \left(\phi - \phi_0 \right). \tag{23.18}$$

Some important inequalities must be satisfied for the flow under consideration. First of all, eq.(23.11) together with eq.(12.4) and the first law of thermodynamics imply that $dp/d\phi < 0$. Using this inequality and the fact that $de = c^2 dp/a^2$ combined with the first law of thermodynamics, it follows that $dn/d\phi < 0$. Also, using eqs.(23.8)-(23.9) it follows that $dv/d\phi \propto -da/d\phi$ and necessarily $dv/d\phi > 0$.

On the other hand, the angle χ that the velocity vector makes with a definite axis is related to the velocity and the azimuthal angle ϕ by:

$$\chi = \phi + \arctan \left(v_\phi / v_r \right) \tag{23.19}$$

as it is seen from fig.(IV.1). Thus, since the ϕ component of Euler's equation, eq.(9.5)

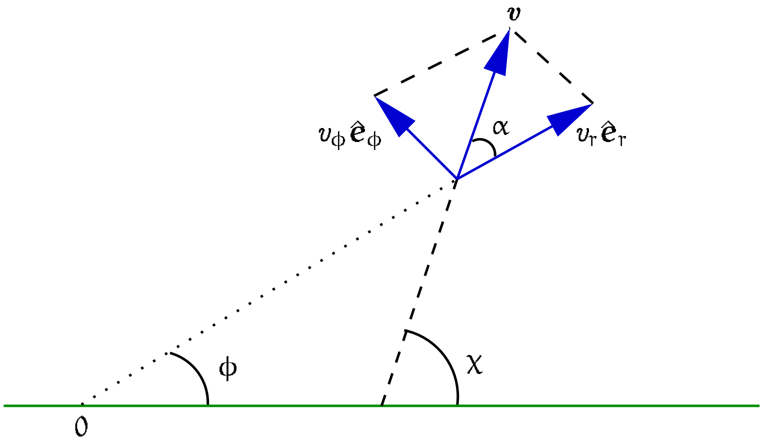

Figure IV.1: Relation between the velocity vector $v = v_r \hat{e}_r + v_\phi \hat{e}_\phi$ and the angle χ, as a function of the azimuthal angle ϕ. χ is the angle that the velocity vector makes with certain fixed axis with origin O.

implies that:

$$\left(v_r + \frac{\partial v_\phi}{\partial \phi} \right) \frac{\gamma^2 v_\phi \omega}{n} + c^2 \frac{\partial \left(\omega / n \right)}{\partial n} = 0,$$

it follows that $d\chi / d\phi = - \left(v^2 \gamma^2 \omega / c^2 \right)^{-1} dp / d\phi$.

In other words, we have proved that for the flow for which we are concerned, the following inequalities are satisfied:

$$dp/d\phi < 0, \quad dn/d\phi < 0, \quad dv/d\phi > 0, \quad d\chi/d\phi > 0. \tag{23.20}$$

A flow with these properties is often described as a *rarefaction wave* (Landau & Lifshitz, 1995) and we will use this name in what follows.

Another, very important property of this rarefaction wave is that the lines at constant ϕ intersect the streamlines at the Mach angle, that is, they are characteristics. Indeed, from fig.(IV.1), it follows that the angle α between the line $\phi = \text{const}$ and the velocity vector v is given by $\sin \alpha = v_\phi / v$. Using eqs.(23.8)-(23.10) it follows that this relation can be written as eq.(11.20). Because all quantities in the problem are functions of a single variable, the angle ϕ, it follows that every hydrodynamical quantity is constant along the characteristics.

§24 Steady simple waves

Let us consider now the two dimensional problem of steady plane parallel flow at infinity which turns through an angle as it flows round a curved profile. A particular case of this problem occurs when the flow turns through an angle (Landau & Lifshitz, 1995). For this particular situation the Prandtl-Meyer flow is obviously the solution and so, the hydrodynamical quantities depend on a single variable, the angle ϕ measured from a defined axis at the onset of the curvature. Because of this, all quantities can be expressed as functions of each other. Since this case is a particular solution to the general problem, it is natural to seek the solutions of the equations of motion in which the quantities p, n, v_x, v_y can be expressed as a function of each other. Evidently this imposes a restriction on the solution of the equations of motion since for two dimensional flow, any quantity depends on two coordinates, x and y, and so any chosen hydrodynamical variable can be written as a function of any other two.

Because of the fact that the flow is uniform at infinity, where all quantities are constant, particularly the entropy, and because the flow is steady, the entropy is constant along a streamline. Thus, if there are no shock waves in the flow, the entropy remains constant along the whole trajectory of the flow and in what follows we will use this result.

In this case, Euler's equation, eq.(9.6), and the continuity equation, eq.(9.1), are respectively:

$$\begin{aligned} v_x \frac{\partial v_x}{\partial x} + v_y \frac{\partial v_x}{\partial y} &= -\frac{c^2}{\gamma\omega} \frac{\partial p}{\partial x}, \\ v_x \frac{\partial v_y}{\partial x} + v_y \frac{\partial v_y}{\partial y} &= -\frac{c^2}{\gamma\omega} \frac{\partial p}{\partial y}, \\ \frac{\partial}{\partial x} \left(\gamma v_x n \right) + \frac{\partial}{\partial y} \left(\gamma v_y n \right) &= 0. \end{aligned}$$

Rewriting these equations as Jacobians[†] we obtain:

$$\begin{aligned} v_x \frac{\partial(v_x, y)}{\partial(x, y)} - v_y \frac{\partial(v_x, x)}{\partial(x, y)} &= -\frac{c^2}{\gamma\omega} \frac{\partial(p, y)}{\partial(x, y)}, \\ v_x \frac{\partial(v_y, y)}{\partial(x, y)} - v_y \frac{\partial(v_y, x)}{\partial(x, y)} &= +\frac{c^2}{\gamma\omega} \frac{\partial(p, x)}{\partial(x, y)}, \\ \frac{\partial(\gamma v_x n, y)}{\partial(x, y)} - \frac{\partial(\gamma v_y n, x)}{\partial(x, y)} &= 0. \end{aligned}$$

We now take the coordinate x and the pressure p as independent variables. To make this transformation we have to multiply the previous set of equations by $\partial(x, y)/\partial(x, p)$. This multiplication leaves the equations the same, but with the substitution $\partial(x, y) \rightarrow \partial(x, p)$. Expanding this last relation and because all quantities are now functions of the pressure p but not of x, it follows that:

[†] The Jacobian $\partial(a, b)/\partial(x, y)$ is defined as:

$$\frac{\partial(a, b)}{\partial(x, y)} = \det \begin{bmatrix} \partial a/\partial x & \partial a/\partial y \\ \partial b/\partial x & \partial b/\partial y \end{bmatrix},$$

It is obvious that $\partial(a, y)/\partial(x, y) = \partial a/\partial x$, and that $\partial(a, b)/\partial(x, y) = -\partial(b, a)/\partial(x, y)$

$$\left(v_y - v_x \frac{\partial y}{\partial x} \right) \frac{d v_x}{dp} = \frac{c^2}{\gamma \omega} \frac{\partial y}{\partial x},$$

$$\left(v_y - v_x \frac{\partial y}{\partial x} \right) \frac{d v_y}{dp} = -\frac{c^2}{\gamma \omega} \frac{\partial y}{\partial x},$$

$$\left(v_y - v_x \frac{\partial y}{\partial x} \right) \frac{d\,(\gamma n)}{dp} + \gamma n \left\{ \frac{d v_y}{dp} - \frac{\partial y}{\partial x} \frac{d v_x}{dp} \right\} = 0.$$

Here we have taken $\partial y / \partial x$ to mean the derivative at constant pressure: $(\partial y / \partial x)_p$. Since every hydrodynamic quantity is assumed to be a function of the pressure, then in the previous set of equations it necessarily follows that $\partial y / \partial x$ is a function which depends only on the pressure, that is $(\partial y / \partial x)_p = f_1(p)$. Therefore:

$$y = x f_1(p) + f_2(p). \tag{24.1}$$

No further calculations are needed if we use the solution for the case in which a rarefaction wave is formed when flow turns around an angle (Landau & Lifshitz, 1995). This solution is given by the results of section §23. As was mentioned in that section, all hydrodynamical quantities are constant along the characteristic lines $\phi = \text{const}$. This particular solution of the flow past an angle obviously corresponds to the case in which $f_2(p) = 0$ in eq.(24.1). The function $f_1(p)$ is determined from the equations obtained in section §23.

For a given constant value of the pressure p, eq.(24.1), gives a set of straight lines in the x–y plane. These lines intersect the streamlines at the Mach angle. This is due to the fact that the lines $y = x f_1(p)$ for the particular solution of the flow through an angle have this property. In other words, one family of characteristic surfaces correspond to a set of straight lines along which all quantities remain constant. However, for the general case, this lines are no longer concurrent.

The properties of the flow as described above are analogous to the non–relativistic equivalent known as *simple waves* (Landau & Lifshitz, 1995). In what follows we will use this name to refer to such a flow.

Let us now construct the solution for a simple wave once a fixed profile is given. Consider the profile as shown in fig.(IV.1). Plane parallel steady flow streams from the left of the point O and flows around the given profile. Since we assume that the flow is supersonic, the effect of the curvature starting at O is communicated to the flow only downstream of the characteristic OA generated at point O. The characteristics to the left of OA, region 1, are all parallel and intersect the x axis at the Mach Angle α_1 given by eq.(11.20):

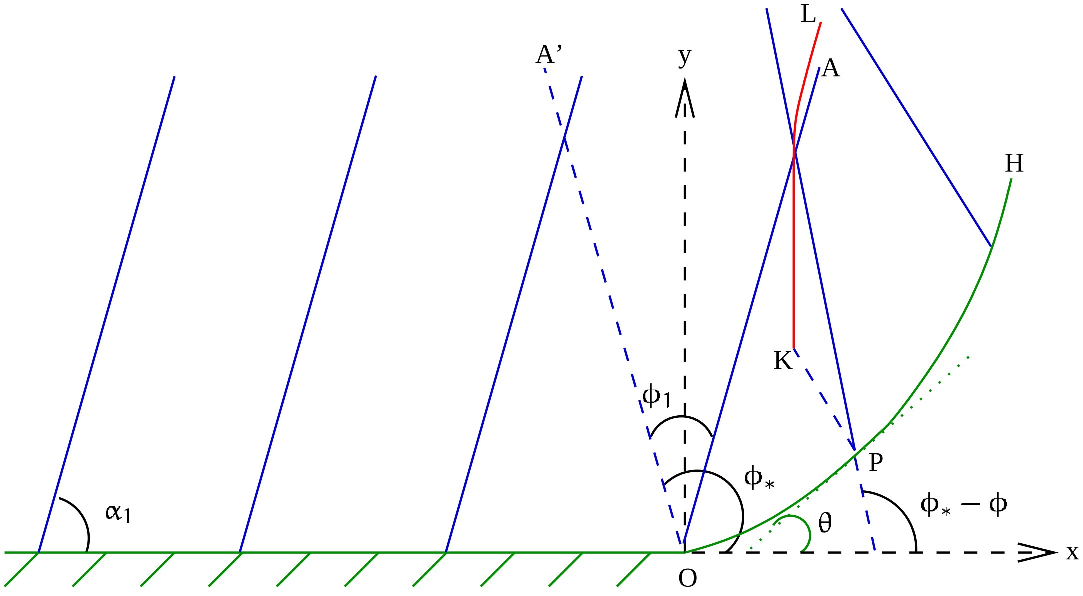

Figure IV.2: Supersonic uniform flow at the left of the diagram bends around a curved profile OH. The Mach angle α_1 is the angle made by the characteristics and the streamlines before the onset of the curvature. The characteristics make an angle ϕ_1 with the "continuation" of the rarefaction wave formed at the onset of the curvature and the angle ϕ is measured from the line 0A'. The curvature causes the characteristic lines to intersect eventually and this occurs at point K in the diagram, giving rise to a shock wave represented as the segment KL.

$$\sin\alpha_1 = \frac{\sqrt{1-(v_1/c)^2}}{\sqrt{1-(a/c)^2}}\,\frac{a}{v_1}, \tag{24.2}$$

where the velocity v_1 is the velocity of the flow to the left of the characteristic OA. In eqs.(23.11)-(23.18) the angle ϕ of the characteristics is measured with respect to some straight line in the x–y plane. As a result, we can choose for those equations the constant of integration $\phi_0 \equiv 0$. This means that the line from which the angle ϕ is measured has been chosen in a very particular way. In order to find the line which is the characteristic for $\phi = 0$, let us proceed as follows. When $\phi = 0$ and the gas is ultrarelativistic, eqs.(23.13)-(23.14) show that the velocity $v = a$ and for the classical case, it follows from eqs.(23.17)-(23.18) that the velocity takes the value $v = c$. In both cases this means that the line $\phi = 0$ corresponds to the point at which the flow has reached the value of the local velocity of sound. This, however, is not possible since we are assuming that the flow is supersonic everywhere. Nevertheless, if the rarefaction wave is assumed to extend formally into the region to the left of OA, we can use these relations and then the characteristic line must correspond to a value of ϕ given by:

$$\phi_1 = \sqrt{\frac{\kappa+1}{\kappa-1}}\arccos\left(\frac{c_1}{c_*}\right), \tag{24.3}$$

for a classical gas according to eq.(23.15), and

$$\phi_1 = \frac{c}{a}\arccos\frac{\sqrt{1-(v_1/c)^2}}{\sqrt{1-(a/c)^2}}, \tag{24.4}$$

for the ultrarelativistic case according to eq.(23.7), eq.(23.10) and eq.(23.12). The angle between the characteristics and the x axis is then given by: $\phi_* - \phi$, where $\phi_* = \alpha_1 + \phi_1$, and the angle α_1 is the Mach angle in region 1. The x and y velocity components in terms of the azimuthal angle θ are given by:

$$v_x = v\cos\theta, \qquad v_y = v\sin\theta, \tag{24.5}$$

and the values for the magnitude of the velocity, the angle θ and the pressure are given by:

$$v^2 = c_*^2\left\{1 + \frac{2}{\kappa-1}\sin^2\sqrt{\frac{\kappa-1}{\kappa+1}}\phi\right\}, \tag{24.6}$$

$$\begin{aligned}\theta &= \phi_* - \phi - \alpha,\\ &= \phi_* - \phi - \arctan\left\{\sqrt{\frac{\kappa-1}{\kappa+1}}\cot\sqrt{\frac{\kappa-1}{\kappa+1}}\phi\right\},\end{aligned} \tag{24.7}$$

$$p = p_*\cos^{2\kappa/(\kappa-1)}\sqrt{\frac{\kappa-1}{\kappa+1}}\phi, \tag{24.8}$$

for a classical gas according to eqs.(23.15)-(23.18) and using the fact that the Poisson adiabatic for a polytropic gas means that: $pc^{-2\kappa/(\kappa-1)} = \text{const}$. In the case of an ultrarelativistic gas, eqs.(23.12)-(23.14) together with Bernoulli's equation and the fact that the enthalpy density $\omega = \kappa p/(\kappa-1)$ give:

$$v^2 = c^2\left\{1 - (2-\kappa)\cos^2\sqrt{\kappa-1}\phi\right\}, \tag{24.9}$$

$$\begin{aligned}\theta &= \phi_* - \phi - \alpha,\\ &= \phi_* - \phi - \arctan\left\{\sqrt{\kappa-1}\cot\sqrt{\kappa-1}\phi\right\},\end{aligned} \tag{24.10}$$

$$p = p_0(2-\kappa)^{-\kappa/2(\kappa-1)}\cos^{-\kappa/(\kappa-1)}\sqrt{\kappa-1}\phi. \tag{24.11}$$

Since the angle $\phi_* - \phi$ is the angle between the characteristics and the x axis, it follows that the line describing the characteristics is:

$$y = x \tan\left(\phi_* - \phi\right) + G(\phi). \tag{24.12}$$

The function $G(\phi)$ is obtained from the following arguments for a given profile of the curvature (Landau & Lifshitz, 1995). If the equation describing the shape of the profile is given by the points X and Y where $Y = Y(X)$, the velocity of the gas is tangential to this surface, and so:

$$\tan\theta = \frac{dY}{dX}. \tag{24.13}$$

Now, the equation of the line through the point (X, Y) which makes an angle $\phi_* - \phi$ with the x axis is:

$$y - Y = (x - X)\tan\left(\phi_* - \phi\right). \tag{24.14}$$

Eq.(24.14) is the same as eq.(24.12) if we set:

$$G(\phi) = Y - X\tan(\phi_* - \phi). \tag{24.15}$$

If we start from a given profile $Y = Y(X)$ then, using eq.(24.13) we can find the parametric set of equations: $X = X(\theta)$ and $Y = Y(\theta)$. Substitution of $\theta = \theta(\phi)$ from eq.(24.7) or eq.(24.10) depending of whether the gas is classical or ultrarelativistic, we find $X = X(\phi)$ and $Y = Y(\phi)$. Substitution of this in eq.(24.15) gives the required function $G(\phi)$.

If the shape of the surface around which the gas flows around is convex, the angle θ that the velocity vector makes with the x axis decreases downstream. The angle $\phi - \phi_*$ between the characteristics leaving the surface and the x axis also decreases monotonically. In other words, characteristics for this kind of flow do not intersect and we form a continuous and rarefied flow.

On the other hand, if the shape of the surface is concave as shown in fig.(IV.2), the angle θ increases monotonically and so does the angle the characteristics make with the x axis. This means that there must exist a region in the flow in which characteristics intersect. The value of the hydrodynamical quantities is constant for every characteristic line. This constant however changes for different non–parallel characteristics. In other words, at the point of intersection different hydrodynamical quantities –for example, the pressure– are multivalued. This situation can not occur and results in the formation of a shock wave. This shock wave cannot be calculated from the above considerations, since they were based on the assumption that the flow had no discontinuities at all –the entropy was assumed to be constant. However, the point at which the shock wave starts, that is point K in fig.(IV.2), can be calculated from the following considerations. We can work out the inclination of the characteristics ϕ as a function of the coordinates x and y. This function $\phi(x, y)$ becomes multivalued when these coordinates exceed certain fixed values, say x_0 and y_0. At a fixed $x = x_0$ the curve giving the value of ϕ as a function of y becomes multivalued. That is, the derivative $(\partial\phi/\partial y)_x = \infty$, or $(\partial y/\partial\phi)_x = 0$. It is evident that at the point $y = y_0$ the curve $\phi(y)$ must lie in both sides of the vertical tangent, else the function $\phi(y)$ would already be multivalued. This means that the point (x_0, y_0) cannot be a maximum, or a minimum of the function $\phi(y)$ but it has to be an inflection point. In other words, the coordinates of point K in fig.(IV.2) can be calculated from the set of equations (Landau & Lifshitz, 1995):

$$\left(\frac{\partial y}{\partial\phi}\right)_x = 0, \qquad \left(\frac{\partial^2 y}{\partial\phi^2}\right)_x = 0. \tag{24.16}$$

When the profile is concave, the streamlines that pass above the point O in fig.(IV.2) pass through a shock wave and the simple wave no longer exist. Streamlines that pass below this point seem to be safe from destruction. However, the perturbing effect from the shock wave KL influences this region also, and so it is not possible to describe the flow there as a simple wave. Nevertheless, since the flow is supersonic, the perturbing effect of the shock wave is only communicated downstream. This means that the region to the left of the characteristic PK (which corresponds to the other set of characteristics emanating from point P) does not notice the presence of the shock wave. In other words, the solution mentioned above, in which a simple wave is formed around a concave profile is only valid to the left of the segment PKL.

§25 Curved jets

Let us now use the results obtained in sections §23 and §24 and apply them to the case of jets that are curved due to any mechanism, for example the interaction of the jet with a cloud as was discussed in Chapter III.

The greatest danger occurs when a jet is bent and forms internal shock waves. This is because, after a shock, the normal velocity component of the flow to the surface of the shock becomes subsonic and the jet flares outward. Nevertheless, as we have seen in section §24, the shock that forms when gas flows around a curved profile (such as a bent jet due to external pressure gradients) does not start from the boundary of the jet. It actually forms at an intermediate point to the flow. In other words, it is possible that, if a jet does not bend too much the intersection of the characteristic lines actually occurs outside the jet and the flow can curve without the production of internal shocks.

As we have seen in section §24 the Mach angle of the flow, relativistic and non-relativistic, does not remain constant in the bend –see for example eq.(24.7) and eq.(24.10).

The Mach number monotonically decreases as the bend proceeds.

Eq.(24.7) and eq.(24.10) imply that:

$$\tan\alpha = -\mu \cot \mu \left(\alpha + \theta - \phi_*\right). \tag{25.1}$$

where

$$\mu \equiv \begin{cases} \sqrt{(\kappa - 1)/(\kappa + 1)} & \text{if the gas is classical,} \\ \sqrt{\kappa - 1} & \text{for an ultrarelativistic gas.} \end{cases} \tag{25.2}$$

As was mentioned above, if the jet is sufficiently narrow, it appears that it can safely avoid the formation of an internal shock. However, differentiation of eq.(25.1) with respect to the angle the velocity vector makes with the x axis, that is the *deflection angle* θ, implies that:

$$\frac{d\alpha}{d\theta} = \frac{1}{2}\left(\Gamma - 1 + \frac{\Gamma + 1}{M^2 - 1}\right), \tag{25.3}$$

with

$$\Gamma \equiv \begin{cases} \kappa & \text{if the gas is classical,} \\ \kappa/(2 - \kappa) & \text{for an ultrarelativistic gas.} \end{cases} \tag{25.4}$$

The Mach number M is given by eq.(11.22) and eq.(11.20) respectively. As the Mach number $M \to 1$, then the derivative $d\alpha/d\theta \to \infty$. This means that the rate of change of the Mach angle with respect to the deflection angle grows without limit as the Mach number decreases and reaches unity. On a bend, the Mach number decreases and care is needed, otherwise characteristics will intersect at the end of the curvature. There is only one special shape for which this effect is bypassed and this occurs when the increase of θ matches exactly with the increase of α (Courant & Friedrichs, 1976), but of course, this is quite a unique case. It appears however, that whatever the thickness of the jet it cannot be bent more than the point at which $d\alpha/d\theta$ exceeds the rate of change of θ with respect to the bending angle θ. In other words, $d\alpha/d\theta \leq d\theta/d\theta = 1$. From this last inequality and eq.(25.3) a value of the Mach number can be obtained (Icke, 1991):

$$M_\star = \frac{2}{\sqrt{3 - \Gamma}}. \tag{25.5}$$

If the Mach number in the jet decreases in such a way that the value $M_\star$ is reached, then a *terminal shock* is produced and the jet structure is likely to be disrupted. It is important to note that this terminal shock is weak since $M \gtrsim 1$ and so, it might not be too disruptive. Nevertheless, this monotonic decrease of the Mach number makes the jet to flare outwards, even if the terminal shock is weak.

Let us now calculate an upper limit for the maximum deflection angle for which jets do not produce terminal shocks. In order to do so, we rewrite eq.(25.1) in the following way:

$$-\theta = \arcsin\frac{1}{M} + \frac{1}{\mu}\arctan\left\{\mu\sqrt{M^2-1}\right\} - \phi_* \tag{25.6}$$

To eliminate the constant ϕ_* from all our relations, we can compare the angle θ evaluated at the minimum possible value of the Mach angle $M = M_*$ with θ evaluated at its maximum value $M = \infty$. In other words, the angle θ_{max} defined as:

$$\theta_{\text{max}} \equiv \theta(M = M_*) - \theta(M = \infty) = \begin{cases} 74.21^\circ & \text{for the classical case,} \\ 47.94^\circ & \text{for an ultrarelativistic gas.} \end{cases} \tag{25.7}$$

is an upper limit to the deflection angle. Jets which bend more than this limiting value θ_{max} develop a terminal shock and the jet will flare outward.

This upper limit however, does not mean that the jet is immune from developing an internal shock if it is bent by a smaller angle. Indeed, let us suppose that the jet bends and that the curvature it follows is a segment of a circle as it is shown in fig.(IV.3). According to the figure, the equation of the characteristic OA that emanates from the point O, where the curvature starts is:

$$y = x\tan\alpha \tag{25.8}$$

Once the flow has curved $d\theta$ degrees, the characteristic at this point is given by:

$$\begin{aligned} y &= (x - Rd\theta)\tan(\alpha + d\alpha + d\phi) \\ &\approx x\tan\alpha + x(d\alpha + d\theta)/\cos^2\alpha - Rd\theta\tan\alpha, \end{aligned}$$

where R is the radius of curvature of the circular trajectory. The intersection of this characteristic and that given by eq.(25.8) occurs when the y coordinate has a value:

$$D = \frac{R\sin^2\alpha}{1 + d\alpha/d\theta}.$$

Substitution of eq.(25.3) gives (Icke, 1991):

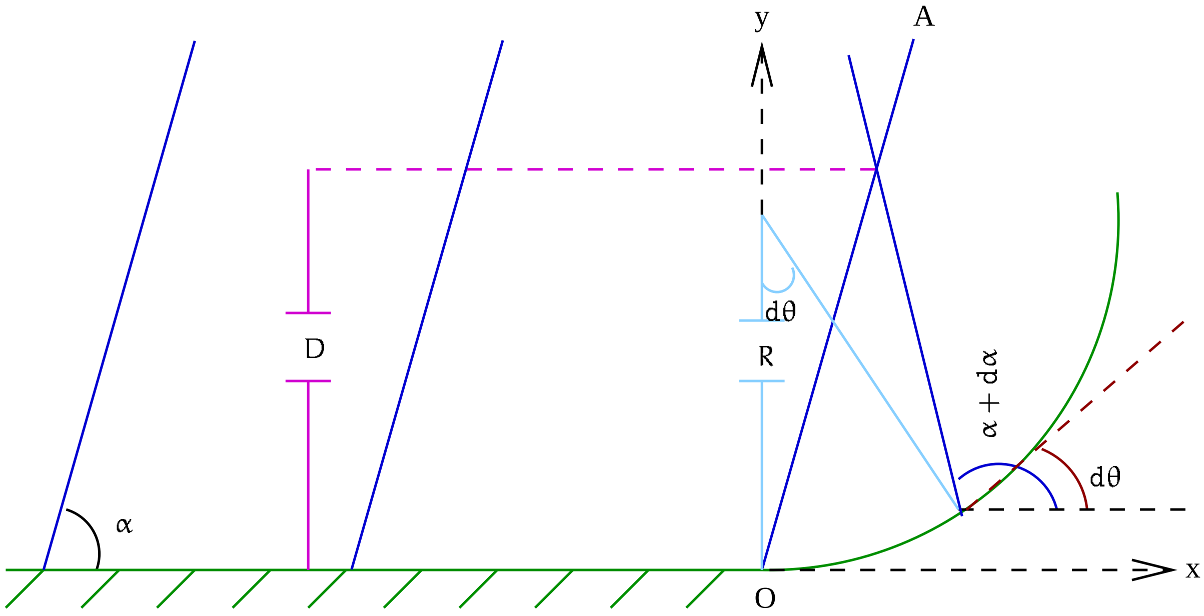

Figure IV.3: Sketch of a curved jet of radius D that develops a shock at the beginning of the curvature. The curve is assumed to be a circle with radius R. The Mach angle of the jet is α at the left of the characteristic OA that emanates from the point where the bending starts.

$$\frac{D}{R} = \frac{2}{\Gamma + 1} \left(M^2 - 1 \right) M^{-4}. \tag{25.9}$$

Using eq.(25.6) and eq.(25.9) it is possible to make a plot in which two zones separate the cases for jets which develop shocks at the onset of the curvature, and the ones that do not. Indeed, we can plot the ratio of the width of the jet D to radius of curvature R as a function of the difference $\theta - \theta_\star$ between the deflection angle θ and the maximum deflection angle $\theta_\star \equiv \theta(M_\star)$, as is shown in fig.(IV.4).

Jets for which the ratio D/R lies below the curve do not develop any shocks at all. For example, consider a jet with a given Mach number for which its ratio D/R is given. As the width of the jet increases (or the radius of curvature of the profile decreases), it comes a point in which a shock at the onset of the curvature is produced. In the same way, jets with a fixed ratio D/R for a given Mach number which are initially stable –so that they lie below the curve– can develop a shock at the beginning of the curvature by increasing the bending angle of the curve.

The relativistic Mach angle is smaller for a given value of the velocity of the flow than its classical counterpart as it was proved in Section §11 –see for example fig.(II.2). This fact is extremely important when analysing the possibility of the intersection of different characteristics in a jet that bends. For a relativistic flow, the characteristics, which make an angle equal to the Mach angle to the streamlines, are always *beamed* in the direction of the flow. Thus, when a jet starts to bend the possibility of intersection between some

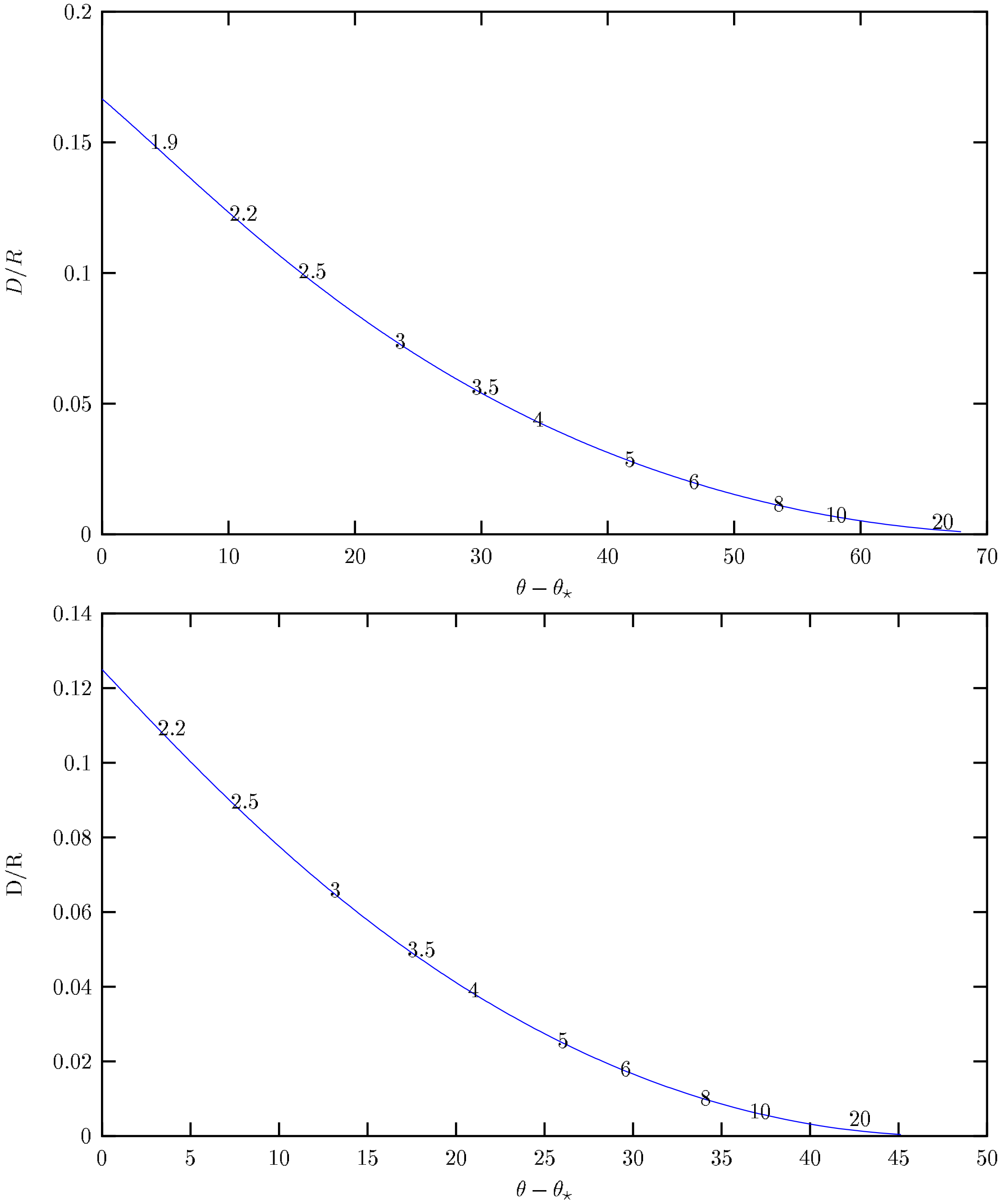

Figure IV.4: Plot of the maximum ratio D/R as a function of the difference $\theta - \theta_\star$ where θ is the deflection angle and $\theta_\star$ is the maximum bending angle a jet can have in order not to produce a terminal shock. The plot refers to the points for which a shock at the beginning of the curvature (which was assumed to be a circle) has developed. Jets with parameters which lie below the curve in any case do not develop any internal shocks at all for this particular circular trajectory. The plot at the top was calculated using the results in which the gas is classical and its polytropic index is 5/3. The plot at the bottom was made by considering the gas to be ultrarelativistic and relativistic effects in the bulk motion of the flow were taken into account. For this second plot, the polytropic index was assumed to be 4/3. The numbers in every plot correspond to the values of the Mach number in the flow.

characteristic line in the curved jet and the ones before the flow has curved, become more probable than their classical counterpart.

This difference results in a severe overestimation of the maximum bending angle θ_{max}. For example, Icke (1991) used the classical analysis in the discussion of the generation of internal shocks due to bending of jets. Using the classical equations described above, but with a polytropic index $\kappa = 4/3$, then $\theta_{\mathrm{max}} = 134.16\,^{\circ}$. This is much greater than the value of $\theta_{\mathrm{max}} = 74.21\,^{\circ}$ obtained with a full relativistic treatment which is impossible.

The analysis made by Icke (1991) is important for jets in which the microscopic motion of the flow inside the jet is relativistic, but the bulk motion of the flow is non–relativistic.

Chapter V

Shock–cloud collisions

In Chapter I different physical mechanisms to account for the alignment effect in radio galaxies were discussed. Whatever the physical mechanism responsible for this effect, it seems that shock waves (Best et al., 2000) are the most important mechanism for producing the observed radiation, at least for the cases of the small double radio sources.

These shock waves might be due to different causes, but the obvious one is the interaction of the shock at the leading edge of the expanding jet of the radio source with cold clouds embedded in the intergalactic medium. In order to describe these collisions, the simplest model is the one described by the interaction of a plane shock wave with a self gravitating cloud in which magnetic fields and relativistic effects may be present. This problem requires unattainable computer power in three dimensions and has not been achieved so far. The best simulation that has been carried out to date is the one in which a plane parallel shock hits a two dimensional spherical cloud of constant density (Klein et al., 1994) in which relativistic effects and magnetic fields are not taken into account. This is of course a very simplified version of the problem, but has a very important conclusion: the cloud is destroyed due to instabilities after the interaction.

In this chapter we describe a simplified solution to the problem as compared with that described by Klein et al. (1994). We analyse the interaction of a one dimensional plane parallel shock which collides with a cold high density region bounded by two tangential discontinuities (a *cloud*). Magnetic fields and self gravity of the cloud are not taken into account. This oversimplification has made it possible to give a complete analytic description of the interaction.

§26 Background to shock–cloud collisions

The problem of the collision of a shock wave with a cloud has been intensively investigated in the past by several authors (see for example Klein et al. 1994 and references therein). The simplest assumption is to consider a cloud for which gravitational effects can be neglected, magnetic fields are non-important and radiative losses are negligible. The fact that gravity is not taken into account, makes it possible to consider the density of the cloud to be uniform. The complete 3D hydrodynamical problem is extremely complicated, even under the simplifications mentioned above. However, numerical simulations have been carried out for this case which ultimately give rise to instabilities causing a complete disruption of the cloud (Klein et al., 1994).

This chapter describes how the solution of the one dimensional problem can be obtained. It has been argued in the past that at least for the case in which the density contrast is high, i.e. the ratio of the cloud's density to that of the external environment is high, the problem has to be very similar to that found in the problem of a collision of a plane parallel shock with with a solid wall (Spitzer 1982, McKee 1988).

With these considerations in mind, the present discussion aims to give a simple approach to solve a particular case of the whole problem. In the description of the solution of the problem of the collision between a plane parallel shock and a plane parallel cloud, it is assumed that the specific volume in the cloud is a first order quantity. In other words solutions are given for the case in which the density of the cloud is much greater than that of the surrounding environment.

§27 General description of the problem

Consider two plane parallel infinite tangential discontinuities. The cloud, or internal region to the tangential discontinuities has uniform pressure p_c and density ρ_c. The environment, or external region to the cloud has also uniform values of pressure p_1 and density ρ_1 respectively. A plane parallel shock wave is travelling in the positive x direction and eventually will collide with the left boundary of the cloud at time $t = t_0 < 0$. By definition, the density of the cloud is greater than that of the environment. Knowing the pressure p_2 and density ρ_2 behind the shock wave, it is possible to solve the hydrodynamical problem thus defined.

The problem of the collision of a shock wave and a tangential discontinuity is well known (Landau & Lifshitz, 1995) and was first discussed by Hugoniot in 1885. Since at the instantaneous time of collision the values of, say, the density in front and behind the shock are ρ_c and ρ_2 respectively, the standard jump conditions for a shock no longer hold. A discontinuity in the initial conditions (first initial discontinuity) occurs.

When a discontinuity in the initial conditions occurs, the values of the hydrodynamical quantities need not to have any relation at all between them at the surface of discontinuity. However, certain relations need to be valid in the gas if stable surfaces of discontinuity are to be created. For instance, the Rankine-Hugoniot relations have to be valid in a shock wave. What happens is that this initial discontinuity splits into several discontinuities, which can be of one of the three possible types: shock wave, tangential discontinuity or weak discontinuity. These newly formed discontinuities move apart from each other with respect to the plane of formation of the initial discontinuity.

Very general arguments show that only one shock wave or a pair of weak discontinuities bounding a rarefaction wave can move in opposite directions with respect to the point in which the initial discontinuity took place. For, if two shock waves move in the same direction, the shock at the front would have to move, relative to the gas behind it, with a velocity less than that of sound. However, the shock behind must move with a velocity greater than that of sound with respect to the same gas. In other words, the leading shock will be overtaken by the one behind. For exactly the same reason a shock and a rarefaction wave cannot move in the same direction, due to the fact that weak discontinuities move at the velocity of sound relative to the gas they move through. Finally, two rarefaction waves moving in the same direction cannot become separated, since the velocities of their boundaries with respect to the gas they move through is the same.

Boundary conditions demand that a tangential discontinuity must remain at the point where the initial discontinuity took place. This follows from the fact that the discontinuities formed as a result of the initial discontinuity must be such that they are able to take the gas from a given state at one side of the initial discontinuity to another state in the opposite side. The state of the gas in any one dimensional problem in hydrodynamics is given by three parameters (say the pressure, the density and the velocity of the gas). A shock wave however, is represented by only one parameter as can be seen from the shock adiabatic relation (Hugoniot adiabatic) for a polytropic gas (c.f. eq.(13.19)):

$$\frac{V_b}{V_f} = \frac{(\kappa+1)p_f + (\kappa-1)p_b}{(\kappa-1)p_f + (\kappa+1)p_b}, \tag{27.1}$$

where p and V stand for pressure and specific volumes respectively, κ is the polytropic index of the gas and the subscripts f and b label the flow in front of and behind the shock. For a given thermodynamic state of the gas (i.e. for given p_f and V_f) the shock wave is determined completely since, for instance, p_b would depend only on V_b according to the shock adiabatic relation. On the other hand, a rarefaction wave is also described by a single parameter. This is seen from the equations which describe the gas inside a rarefaction wave which moves to the left with respect to gas at rest beyond its right boundary (c.f. eqs.(14.11)-(14.14)):

$$c_R = c_4 + \frac{1}{2}(\kappa_c - 1)w_R, \tag{27.2}$$

$$\rho_R = \rho_4 \left\{ 1 + \frac{1}{2}\frac{(\kappa_c - 1)w_R}{c_4} \right\}^{2/(\kappa_c - 1)}, \tag{27.3}$$

$$p_R = p_4 \left\{ 1 + \frac{1}{2}\frac{(\kappa_c - 1)w_R}{c_4} \right\}^{2\kappa_c/(\kappa_c - 1)}, \tag{27.4}$$

$$w_R = -\frac{2}{\kappa_c + 1}\left(c_4 + \frac{x}{t} \right). \tag{27.5}$$

where c_4 and c_R represent the sound speed behind and inside the rarefaction wave respectively. The magnitude of the velocity of the flow inside the rarefaction wave is w_R in that system of reference. The quantities p_4 and p_R are the pressures behind and inside the rarefaction wave respectively. The corresponding values of the density in the regions just mentioned are ρ_4 and ρ_R.

With two undetermined parameters, it is not possible to give a description of the thermodynamic state of the gas. It is the tangential discontinuity, which remains where the initial discontinuity was produced, that accounts for the third parameter needed to describe the state of the fluid.

When a shock wave hits a tangential discontinuity, a rarefaction wave cannot be transmitted to the other side of the gas bounded by the tangential discontinuity. For, if there were a transmitted rarefaction wave to the other side of the tangential discontinuity, the only possible way the boundary conditions could be satisfied is if a rarefaction wave is reflected back to the gas. In other words, two rarefaction waves separate from each other in opposite directions with respect to the tangential discontinuity that is left after the interaction. In order to show that this is not possible, consider a shock wave travelling in the positive x direction, which compresses gas 1 into gas 2 and collides with a tangential discontinuity. After the interaction two rarefaction waves separate from each other and a tangential discontinuity remains between them. In the system of reference where the tangential discontinuity is at rest, the velocity of gas 2 is given by $v_2 = -\int_{p_3}^{p_2} \sqrt{-\mathrm{d}p\,\mathrm{d}V}$, according to eq.(14.5), where p_3 is the pressure of gas 3 surrounding the tangential discontinuity. Accordingly, the velocity of gas 1 in the same system of reference is $v_1 = -\int_{p_3}^{p_1} \sqrt{-\mathrm{d}p\,\mathrm{d}V}$. Since the product $-\mathrm{d}p\,\mathrm{d}V$ is a monotonically increasing function of the pressure and $0 \leq p_3 \leq p_1$ then:

$$-\int_0^{p_2} \sqrt{-\mathrm{d}P\,\mathrm{d}V} \leq v_2 - v_1 \leq \int_0^{p_1} \sqrt{-\mathrm{d}P\,\mathrm{d}V} - \int_{p_1}^{p_2} \sqrt{-\mathrm{d}P\,\mathrm{d}V}.$$

The difference in velocities $v_1 - v_2$ has the same value in any system of reference and so, it follows that $v_1 \leq v_2$, in particular in a system of reference in which the incident shock is at rest. However, for the incident shock to exist, it is necessary that $v_1 > v_2$, and so two rarefaction waves cannot be formed as a result of the interaction.

So far, it has been shown that after the collision between the shock and the boundary of the cloud, a first initial discontinuity is formed. This situation cannot occur in nature and the shock splits into a shock which penetrates the cloud and either one of a shock, or a rarefaction wave (bounded by two weak discontinuities) is reflected from the point of collision. With respect to the point of formation of the initial discontinuity, the boundary conditions demand that a tangential discontinuity must reside in the region separating the discontinuities previously formed.

In a shock wave, the velocities (v) in front and behind the shock are related to one another by their difference:

$$v_{\rm f} - v_{\rm b} = \sqrt{(\mathrm{p_b} - \mathrm{p_f})(V_{\rm f} - V_{\rm b})}, \tag{27.6}$$

according to eq.(13.20) where the subscripts f and b label the flow of the gas in front and behind the shock wave.

If after the first initial discontinuity two shock waves separate with respect to the point of collision, then according to eq.(27.6) the velocities of their shock front flows are given by $v_{\rm c} = -\sqrt{(\mathrm{p}_3 - \mathrm{p}_1)(V_{\rm c} - V_{3'})}$ and $v_2 = \sqrt{(\mathrm{p}_3 - \mathrm{p}_2)(V_2 - V_3)}$, where the regions 3 and $3'$ bound the tangential discontinuity which is at rest in this particular system of reference (see top and middle panels of fig.(V.1)). Due to the fact that $\mathrm{p}_3 \geq \mathrm{p}_2$ and because the difference $v_2 - v_{\rm c}$ is a monotonically increasing function of the pressure p_3, then:

$$v_2 - v_{\rm c} > (\mathrm{p}_2 - \mathrm{p}_1)\sqrt{\{2V_{\rm c}/[(\kappa_{\rm c} - 1)\mathrm{p}_1 + (\kappa_{\rm c} + 1)\mathrm{p}_2]\}},$$

according to the shock adiabatic relation. Since $v_2 - v_{\rm c}$ is given by eq.(27.6), then:

$$\frac{V_1}{(\kappa - 1) + (\kappa + 1)\mathrm{p}_2/\mathrm{p}_1} > \frac{V_{\rm c}}{(\kappa_{\rm c} - 1) + (\kappa_{\rm c} + 1)\mathrm{p}_2/\mathrm{p}_1}, \tag{27.7}$$

where κ and $\kappa_{\rm c}$ represent the polytropic indexes of the environment and the cloud respectively. V_1 and $V_{\rm c}$ are the specific volumes on the corresponding regions. In other words, a necessary and sufficient condition to have a reflected shock from the boundary of the two media, under the assumption of initial pressure equilibrium between the cloud and the environment, is given by eq.(27.7). Since for the problem in question $V_1 > V_{\rm c}$ and the polytropic indexes are of the same order of magnitude, a reflected shock is produced.

In the same way, at time $\mathrm{t} = 0$ when the transmitted shock reaches the right tangential discontinuity located at $\mathrm{x} = 0$, another (second) initial discontinuity must occur. In this case, we must invert the inequality in eq.(27.7), change κ by $\kappa_{\rm c}$ and p_2 by p_3, where p_3 is the pressure behind the shocks produced by the first initial discontinuity. Again, using the same argument for the polytropic indexes, it follows that after this interaction a rarefaction wave bounded by two weak discontinuities must be reflected from the boundary between the two media. As a result of the interaction, once again, the boundary conditions demand that a tangential discontinuity remains between the newly formed discontinuities.

This situation continues until the rarefaction wave and the left tangential discontinuity of the cloud collide at time $\mathrm{t} = \tau > 0$. At this point, two rarefaction waves separating from each other from the point of formation will be produced once a stationary situation is reached, and a tangential discontinuity will separate the newly formed discontinuities. One could continue with the solution for further reflections of the shock and rarefaction waves but, for the sake of simplicity, the calculations are stopped at this point. Fig.(V.1)

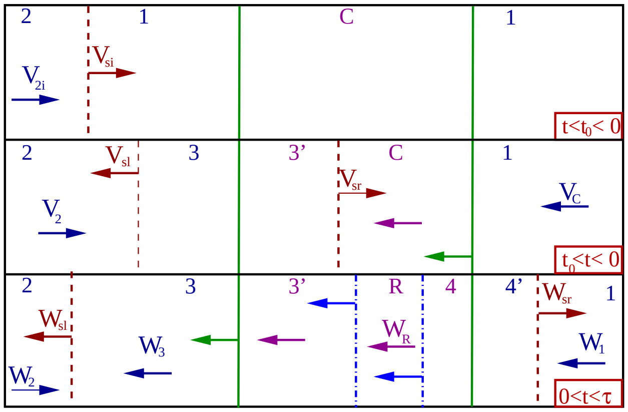

Figure V.1: An incoming shock travelling to the right (top panel) hits a tangential discontinuity at time $t_0 < 0$. This produces two shocks moving in opposite directions with respect to the place of formation (middle panel). When the transmitted shock into the cloud (region C) collides with its right boundary a reflected rarefaction wave (region R) bounded by two tangential discontinuities and a shock transmitted to the external medium (lower panel) are formed. Arrows represent direction of different boundaries, or the flow itself. The numbers in the figure label different regions of the flow. Dashed lines represent shocks, dash-dot are weak discontinuities and continuous ones are tangential discontinuities. The system of reference is chosen such that the tangential discontinuities which are left as a result of the collisions are always at rest.

shows a schematic description of the solution described above in a system of reference such that the tangential discontinuities which are left as a result of the different interactions are at rest. The numbers in the figure label different regions in the flow. A more detailed analysis follows in sections §28 and §29.

§28 First initial discontinuity

According to fig.(V.1), after the first initial discontinuity the absolute values of the velocities (v) of the flow are related by:

$$v_2 + v_c = v_{2i}. \tag{28.1}$$

With the aid of eq.(27.6), the velocities of eq(28.1) are given by:

$$v_{2i}^2 = (p_2 - p_1)(V_1 - V_2), \tag{28.2}$$

$$v_c^2 = (p_3 - p_1)(V_c - V_{3'}), \tag{28.3}$$

$$v_2^2 = (p_3 - p_2)(V_2 - V_3). \tag{28.4}$$

Inserting eqs.(28.2)-(28.4) into eq.(28.1) and substituting for the specific volumes from eq.(27.1), one ends up with a relation which relates the pressure p_3 as a function of p_2,

p_1 and the polytropic indexes in an algebraic linear form. Straightforward manipulations show that the resulting equation does not have an easy analytic solution, even for the particular cases in which a strong or weak incident shock collides with the cloud.

In order to find a set of analytic solutions, let us first describe a particular solution to the problem. If we consider a cloud with an initial infinite density -a solid wall, then eq.(28.1) takes the form $v_2 = v_{2i}$, and a "zeroth order" solution is found (Landau & Lifshitz, 1995):

$$\frac{p_{3_0}}{p_2} = \frac{(3\kappa - 1)p_2 - (\kappa - 1)p_1}{(\kappa - 1)p_2 + (\kappa + 1)p_1}, \tag{28.5}$$

where p_{3_0} is the value of the pressure behind the reflected and transmitted shocks for the case in which the cloud has specific volume $V_c = 0$. For this particular case, eq.(28.5) determines p_{3_0} as a function of p_1 and p_2, which are initial conditions to the problem. Due to the fact that the gas is polytropic, this relation is the required solution to the problem.

In order to find a solution more appropriate to the general case, we can make the approximation that V_c is a first order quantity, that is:

$$p_3 = p_{3_0} + p_3^\star, \tag{28.6}$$

$$V_3 = V_{3_0} + V_3^\star, \tag{28.7}$$

$$V_{3'} = V_{3'}^\star, \tag{28.8}$$

where the quantities with a star are of the first order and the subscript 0 represents the values at zeroth order approximation. Substituting eqs.(28.6)-(28.8) into eqs.(28.3)-(28.4) gives:

$$v_2^2 = v_{2o}^2 - V_3^\star(p_{3_0} - p_2) + p_3^\star(V_2 - V_{3_0}), \tag{28.9}$$

$$v_c^2 = (p_{3_0} - p_1)(V_c - V_{3'}^\star). \tag{28.10}$$

From the shock adiabatic relation, eq.(27.1), and eqs.(28.6)-(28.8) it follows that

$$\frac{V_{3_0}}{V_2} = \frac{(\kappa + 1)p_2 + (\kappa - 1)p_{3_0}}{(\kappa - 1)p_2 + (\kappa + 1)p_{3_0}}, \tag{28.11}$$

$$\frac{V_{3'}^\star}{V_c} = \frac{(\kappa_c + 1)p_1 + (\kappa_c - 1)p_{3_0}}{(\kappa_c - 1)p_1 + (\kappa_c + 1)p_{3_0}}, \tag{28.12}$$

$$\frac{V_3^\star}{V_2} = -\frac{4\kappa p_2 p_3^\star}{[(\kappa - 1)p_2 + (\kappa + 1)p_{3_0}]^2}. \tag{28.13}$$

Substituting eqs.(28.9)-(28.10) and eq.(28.13) in eq.(28.1) gives the required solution:

$$\frac{p_3^\star}{p_2} = -\frac{V_c}{V_2}\left(\frac{|\alpha| + \beta}{\eta}\right), \tag{28.14}$$

where:

$$\begin{aligned}
\beta &= \left(\frac{p_{3_0}}{p_2} - \frac{p_1}{p_2}\right)\left(1 - \frac{V_{3'}^\star}{V_c}\right), \\
\eta &= \left(1 - \frac{V_{3_0}}{V_2}\right) - \left(\frac{p_{3_0}}{p_2} - 1\right)\frac{(\kappa - 1) - (\kappa + 1)\,V_{3_0}/V_2}{(\kappa - 1) + (\kappa + 1)p_{3_0}/p_2}, \\
|\alpha|^2 &= 4\frac{V_2}{V_c}\left(\frac{p_{3_0}}{p_2} - 1\right)\left(\frac{p_{3_0}}{p_2} - \frac{p_1}{p_2}\right)\left(1 - \frac{V_{3_0}}{V_2}\right)\left(1 - \frac{V_{3'}^\star}{V_c}\right).
\end{aligned}$$

The specific volumes V_{3_0} and $V_{3'}^\star$ are given by eq.(28.11) and eq.(28.12) respectively. For completeness, approximations to eq.(28.14) for the case of a very strong incident shock and that of a weak incident shock are given:

$$\frac{p_3^\star}{p_2} = -\frac{4\kappa^2(\kappa + 1)}{(3\kappa - 1)(\kappa - 1)^2}\frac{V_c}{V_1}\left(\frac{3\kappa - 1}{\kappa_c + 1} + k\right), \tag{28.15}$$

$$\frac{p_3^\star}{p_1} = -2\zeta\frac{\kappa}{\kappa_c}\sqrt{\frac{V_c}{V_1}}\left(\sqrt{\frac{\kappa_c}{\kappa}} + \sqrt{\frac{V_c}{V_1}}\right), \tag{28.16}$$

where:

$$k = 2\sqrt{\frac{V_1}{V_c}\frac{(3\kappa - 1)(\kappa - 1)}{(\kappa_c + 1)(\kappa + 1)}},$$

and $\zeta \equiv (p_2 - p_1)/p_1 \ll 1$ in the weak limit. Fig.(V.2) shows a plot of the pressure p_3 as a function of the strength of the incident shock. It is interesting to note that even for very strong incident shocks the ratio p_3/p_2 differs from zero, which follows directly from eq.(28.5) and eq.(28.15). This simply means that the reflected shock is not strong, no matter what initial conditions were chosen.

There are certain important general relations which follow from these results. Firstly, by definition the pressure p_2 behind the shock is greater than the pressure p_1 of the environment. Now consider a strong incident shock. Since $p_3 > p_2 \gg p_1$, it follows that the shock transmitted into the cloud is very strong. Also, the reflected shock does not have to compress the gas behind it too much to acquire the required equilibrium and so, it is not a strong shock. This last statement is in agreement with eq.(28.15). In general, for any strength of the incident shock, since the inequality $p_3 > p_2 > p_1$ holds, continuity demands that the reflected shock cannot be strong and, more importantly, that the penetrating shock is always stronger than the reflected one.

Secondly, very general inequalities are satisfied by the velocities v_2, v_c, v_{sl} as defined

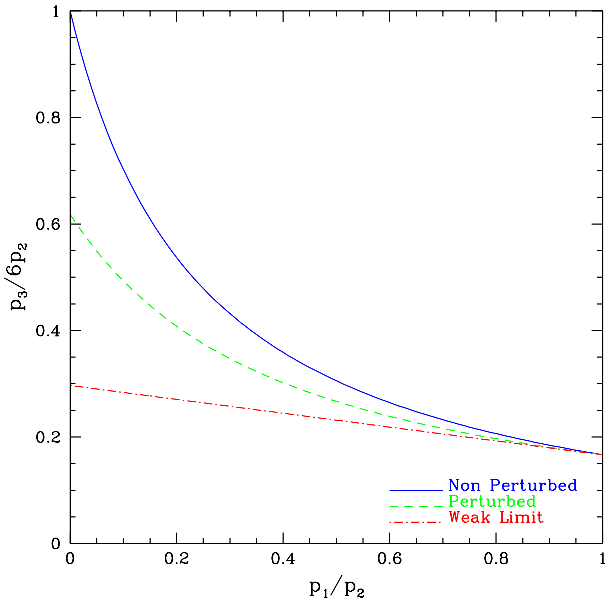

Figure V.2: Variation of the pressure p_3 behind the transmitted shock into the cloud as a function of the strength of the initial incident shock. The continuous line shows the case for which the cloud is a solid wall with infinite density. The dashed curve is the solution at first order approximation in which the cloud's specific volume is a first order quantity. The acoustic approximation in which the incident shock is weak, to the same order of accuracy, is represented by a dot-dashed curve. The perturbed solutions were plotted assuming $\rho_c/\rho_1 = 100$ for polytropic indexes $\kappa = \kappa_c = 5/3$, corresponding to a monoatomic gas.

in fig.(V.1). For instance:

$$v_{s1} > v_2. \tag{28.17}$$

This result follows from the fact that $V_3 v_2/(V_3 - V_2) > v_2$ holds, and the left hand side of this inequality is just v_{s1} according to mass flux conservation across the reflected shock.

On the other hand, from eq.(28.3) and eq.(28.4), since $p_2 > p_1$ it follows that a necessary and sufficient condition for $v_2 > v_c$ to be true is that $V_2 - V_3 > V_c - V_{3'}$. This last condition is satisfied for sufficiently small values of V_c. To give an estimate of the smallness of the cloud's specific volume needed, note that a necessary and sufficient condition for $V_2 - V_3 > V_c - V_{3'}$ to be valid is:

$$\frac{V_2(p_3 - p_2)}{(\kappa - 1)p_2 + (\kappa + 1)p_3} > \frac{V_c(p_3 - p_1)}{(\kappa_c - 1)p_1 + (\kappa_c + 1)p_3}, \tag{28.18}$$

according to the shock adiabatic relation for the transmitted and reflected shocks. Since $p_3 > p_2 > p_1$ and $V_2 < V_1$ it follows that:

$$\frac{V_1}{(\kappa-1)+(\kappa+1)p_3/p_1} > \frac{V_c}{(\kappa_c-1)+(\kappa_c+1)p_3/p_1}, \tag{28.19}$$

which is very similar to eq.(27.7). In the same fashion, under the assumption that the polytropic indexes are of the same order of magnitude, eq.(28.19) implies $V_c < V_1$, which was an initial assumption. Although eq.(28.19) is not sufficient, because V_c is a first order quantity, we can use in what follows:

$$v_2 > v_c. \tag{28.20}$$

The inequalities in eq.(28.17) and eq.(28.20) will prove to be useful later when we choose a more suitable reference system to describe the problem in question.

§29 Second initial discontinuity

Let us now analyse the situation for which $0 < t < \tau$. To begin with let us prove that:

$$w_1 < v_2 + v_c \equiv u_2, \tag{29.1}$$

where the velocities w_1, v_2 and v_c are defined in fig.(V.1). Suppose that the inequality in eq.(29.1) is not valid, then, by expressing the velocities as function of the specific volumes and pressures by means of eq.(27.6) and the fact that $p_2 > p_1$, $p_3 > p_4$ and $V_{4'} > V_3$, it follows that $\rho_3 > \rho_c$; then as the cloud's density grows without limit, so does ρ_3. Necessarily, eq.(29.1) has to be valid for sufficiently small values of the cloud's specific volume. It is important to point out that since $w_2 = |u_2 - w_1| = u_2 - w_1$, the gas in region 2 as drawn in fig.(V.1) travels in the positive x direction. According to fig.(V.1), flows in region 1 and 3 are related by

$$w_1 - w_3 = v_c, \tag{29.2}$$

Let us now prove a very general property of the solution. Regions 2 and 3 are related to one another by the shock adiabatic relation. Since the gas in regions $3'$ and 4 obey a polytropic equation of state $p_3/p_4 = (V_4/V_{3'})^{\kappa_c}$, it follows that:

$$\frac{p_4}{p_2} = \left(\frac{V_{3'}}{V_4}\right)^{\kappa_c} \frac{(\kappa+1)V_2 - (\kappa-1)V_3}{(\kappa+1)V_3 - (\kappa-1)V_2}.$$

Now, due to the fact that $V_{3'} < V_4 < V_1$, $V_3 < V_2 < V_1$ and $\kappa, \kappa_c > 1$ for a reasonable equation of state, this relation can be written

$$\frac{p_4}{p_2} < \frac{1}{2}\left[-(\kappa-1)+(\kappa+1)\frac{V_2}{V_1}\right] \rightarrow 0\,, \quad \text{as } \frac{p_1}{p_2} \rightarrow 0 \tag{29.3}$$

with the aid of the shock adiabatic relation. This result implies that most of the energy of the incoming shock has been injected to the cloud, no matter how strong the initial incident shock is. Only a very small fraction of this energy is transmitted to the external gas that lies in the other side of the cloud. Note that this result is of a very general nature since no assumptions about the initial density contrast of the environment were made. This is an important conclusion. All the energy of the shock is dissipated inside the cloud and so it is important for cloud heating.

In order to continue with a solution at first order approximation in V_c, note that we have to use eqs.(28.6)-(28.8) together with:

$$p_4 = p_1 + p_4^\star, \tag{29.4}$$

$$V_4 = V_4^\star, \tag{29.5}$$

$$V_{4'} = V_1 + V_{4'}^\star, \tag{29.6}$$

where the quantities with a star are of first order. The velocities w_1 and w_3 can be expressed as functions of the specific volumes and pressures by means of eq.(27.6), from which after substitution of eqs.(29.4)-(29.6) it follows that:

$$w_1^2 = -p_4^\star V_{4'}^\star, \tag{29.7}$$

$$w_3 = \frac{2}{\kappa_c - 1}\left(\sqrt{\kappa_c p_{3_0} V_{3'}^\star} - \sqrt{\kappa_c p_1 V_4^\star}\right). \tag{29.8}$$

The specific volumes behind the transmitted shock and the reflected rarefaction wave are obtained from the shock adiabatic relation and the polytropic equation of state for the gas inside the rarefaction wave:

$$V_{4'}^\star = -V_1 \frac{p_4^\star}{\kappa p_1}, \tag{29.9}$$

$$V_4^\star = V_{3'}^\star \left(\frac{p_{3_0}}{p_1}\right)^{1/\kappa_c}. \tag{29.10}$$

By substitution of eqs.(29.7)-(29.10) and eq.(28.4) in eq.(29.2) the required solution is found:

$$\frac{p_4^\star}{p_2} = \sqrt{\frac{\kappa p_1}{p_2}\frac{V_c}{V_1}}\left(\Gamma + \Psi\Lambda\right), \tag{29.11}$$

where:

$$\Psi = \frac{2\sqrt{\kappa_c}}{\kappa_c - 1}\sqrt{\frac{(\kappa_c+1)p_1/p_2 + (\kappa_c-1)p_{3_0}/p_2}{(\kappa_c-1)p_1/p_2 + (\kappa_c+1)p_{3_0}/p_2}}\,,$$
$$\Gamma = \frac{\sqrt{2}\,(p_{3_0} - p_1)/p_2}{\sqrt{(\kappa_c-1)p_1/p_2 + (\kappa_c+1)p_{3_0}/p_2}}\,,$$
$$\Lambda = \sqrt{\frac{p_{3_0}}{p_2}} - \sqrt{\frac{p_1}{p_2}\left(\frac{p_{3_0}}{p_1}\right)^{1/\kappa_c}}\,.$$

For completeness, the limits for the case of strong and weak incident shocks are given:

$$\frac{p_4^\star}{p_2} = \sqrt{\frac{\kappa(3\kappa-1)}{(\kappa_c+1)(\kappa-1)}\frac{p_1}{p_2}\frac{V_c}{V_1}}\left(\sqrt{2} + \xi\right), \tag{29.12}$$

$$\frac{p_4^\star}{p_2} = 6\zeta\sqrt{\frac{\kappa}{\kappa_c}}\sqrt{\frac{V_c}{V_1}}, \tag{29.13}$$

with:

$$\xi = \frac{2\sqrt{\kappa_c}}{\sqrt{(\kappa_c - 1)}}\left[1 - \left(\frac{p_1}{p_2}\frac{\kappa-1}{3\kappa-1}\right)^{(\kappa_c-1)/2\kappa_c}\right].$$

It follows from eq.(29.12) that $p_4 \ll p_2$ as the strength of the incident shock increases without limit. This result was given by the very general argument of eq.(29.3). Fig.(V.3) shows the variation of the pressure p_4 behind the shock transmitted to the environment as a function of the strength of the initial incident shock, after the second initial discontinuity.

§30 General solution

Having found values for the pressures $p_3^\star$ and $p_4^\star$ as a function of the initial conditions p_1, p_2, V_1 and V_c, the problem is completely solved. Indeed, using the shock adiabatic relation V_2 is known. With this, the values of $V_{3'}^\star$, $V_3^\star$, $V_4^\star$ and $V_{4'}^\star$ are determined by means of eq.(28.12), eq.(28.13), eq.(29.9) and eq.(29.10) respectively. The values for all the pressures and specific volumes are obtained using eqs.(28.6)-(28.8) and eqs.(29.4)-(29.6). The velocities of the flow, as defined in fig.(V.1), are calculated either by mass flux conservation on crossing a shock, or by the formula for the velocity discontinuity in eq.(27.6). The hydrodynamical values of the pressure p_R and density ρ_R inside the rarefaction wave come from eqs.(27.2)-(27.5).

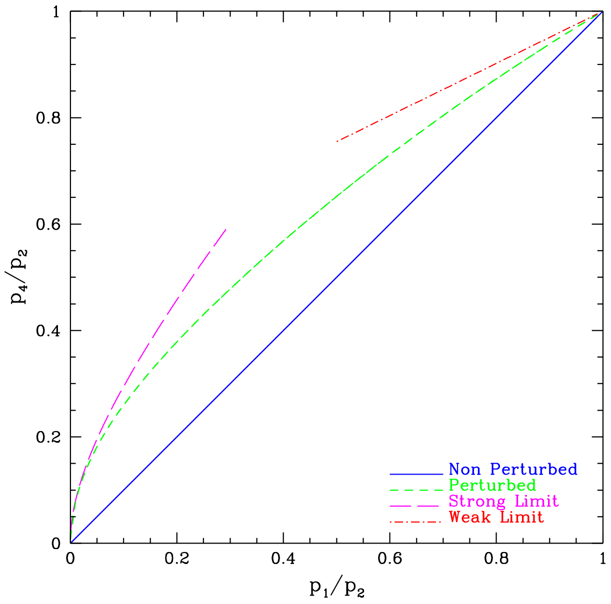

Figure V.3: Variation of the pressure p_4 behind the transmitted shock into the external medium as a function of the strength of the incident shock. The continuous line represents the case for which the cloud has infinite density and so it does not transmit any shock to the external medium. The dashed curve represents the case for which the cloud's specific volume is a quantity of the first order. The dash-dotted curve is the limit for which a strong (or weak) incident shock collides with the cloud at the same order of approximation. The perturbed curves were produced under the assumption that $\rho_c/\rho_1 = 100$ for monoatomic gases.

In order to analyse the variations of the hydrodynamical quantities as a function of position and time, let us now describe the problem in a system of reference in which the gas far away to the right of the cloud is always at rest, as illustrated in fig.(V.4). Let x_{tl} and x_{tr} be the coordinates of the left and right tangential discontinuities, x_{sl} and x_{sr} the coordinates of the reflected and transmitted shocks produced after the first initial discontinuity, χ_{sr} the position of the transmitted shock after the second initial discontinuity and x_a and x_b the left and right weak discontinuities which bound the rarefaction wave. The new velocities are defined by Galilean transformations:

$$u_2 = v_2 + v_c\,, \tag{30.1}$$

$$u_{sl} = v_{sl} - v_c\,, \tag{30.2}$$

$$u_{sr} = v_{sr} + v_c\,, \tag{30.3}$$

$$\nu_R = w_1 - w_R, \tag{30.4}$$

$$\nu_{sr} = w_1 + w_{sr}. \tag{30.5}$$

The direction of motion of the flow is shown in fig.(V.4) and it follows from eq.(28.17), eq.(28.20) and eq.(30.2) that u_{sl} points to the left in this system of reference. Since, in the

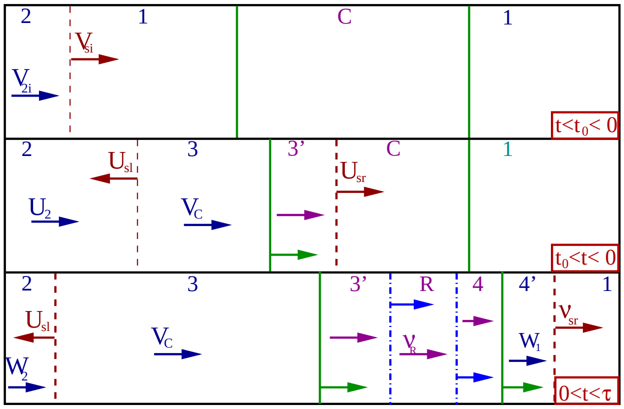

Figure V.4: Description of the problem of a collision of a shock with a cloud in a system of reference in which the gas far away to the right (at $x = \infty$) is always at rest. Originally a shock is travelling to the right and hits a tangential discontinuity (top panel). This produces a discontinuity in the initial conditions so a reflected and transmitted shock are produced; the gas in the cloud begins to accelerate (middle panel). Eventually the transmitted shock into the cloud collides with its right boundary producing a "reflected" rarefaction wave bounded by two weak discontinuities (region R) and a transmitted shock into the external medium (lower panel). In this system of reference every single discontinuity produced by means of the interaction move to the right, except for the reflected shock produced after the first collision. Arrows represent the direction of motion of various boundaries and direction of flow. Numbers label different regions of the flow. Dashed lines represent shock waves, dash-dotted ones weak discontinuities and continuous ones tangential discontinuities.

same frame, v_c and w_1 point to the right, continuity across a weak discontinuity demands v_R to behave in the same way.

The tangential discontinuities and the shocks produced by the initial discontinuities move with constant velocity throughout the gas. This implies that the time at which the first initial discontinuity takes place is:

$$t_0 = -\frac{\Delta}{u_{sr}}, \tag{30.6}$$

where Δ represents the initial width of the cloud. Hence, the positions of all different discontinuities for $t_0 < t < 0$ are:

$$x_{sr} = u_{sr} t, \tag{30.7}$$

$$x_{sl} = -\Delta - u_{sl}(t - t_0), \tag{30.8}$$

$$x_{tl} = -\Delta + v_c(t - t_0). \tag{30.9}$$

and for $0 < t < \tau$, eqs.(30.8)-(30.9) are valid together with

$$x_a = -t\left(\frac{\kappa_c + 1}{2} w_3 + c_4\right) + w_1 t, \tag{30.10}$$

$$x_b = (w_1 - c_4)\,t, \tag{30.11}$$

$$\chi_{sr} = \nu_{sr} t, \tag{30.12}$$

$$x_{tr} = w_1 t. \tag{30.13}$$

The time τ at which the left tangential discontinuity collides with the left boundary of the rarefaction wave is given by $x_{tl} = x_a$, and thus:

$$\tau c_{3'} = v_c t_0 + \Delta. \tag{30.14}$$

Fig.(V.5) shows the variation of the pressure and density as a function of time and position in a system of reference in which the gas far away to the right of the cloud is at rest.

The width of the cloud varies with time, and it follows from eq.(30.9) and eq.(30.13) that this variation is given by:

$$\bar{X}(t) = \Theta(t) w_1 t + \Delta - v_c (t - t_0), \tag{30.15}$$

where $\Theta(t)$ is the Heaviside step function. This linear relation is plotted in fig.(V.6).

§31 Summary

In the previous analysis, the problem of a collision of a plane parallel shock wave with a high density cloud bounded by two plane parallel tangential discontinuities has been discussed. Radiation losses, magnetic fields and self gravity of the cloud were neglected. General analytic solutions were found for the simple case in which the ratio of the environment's density to that of the cloud's density is a quantity of the first order.

When the shock collides with the boundary of the cloud, a discontinuity in the initial conditions is produced. This splits the incoming shock into two shock waves: one which penetrates the cloud and one which is reflected back to the external medium. When the transmitted shock into the cloud reaches the opposite boundary, another discontinuity in the initial conditions is produced, causing the transmission of a shock wave to the external medium and the reflection of a rarefaction wave from the point of collision.

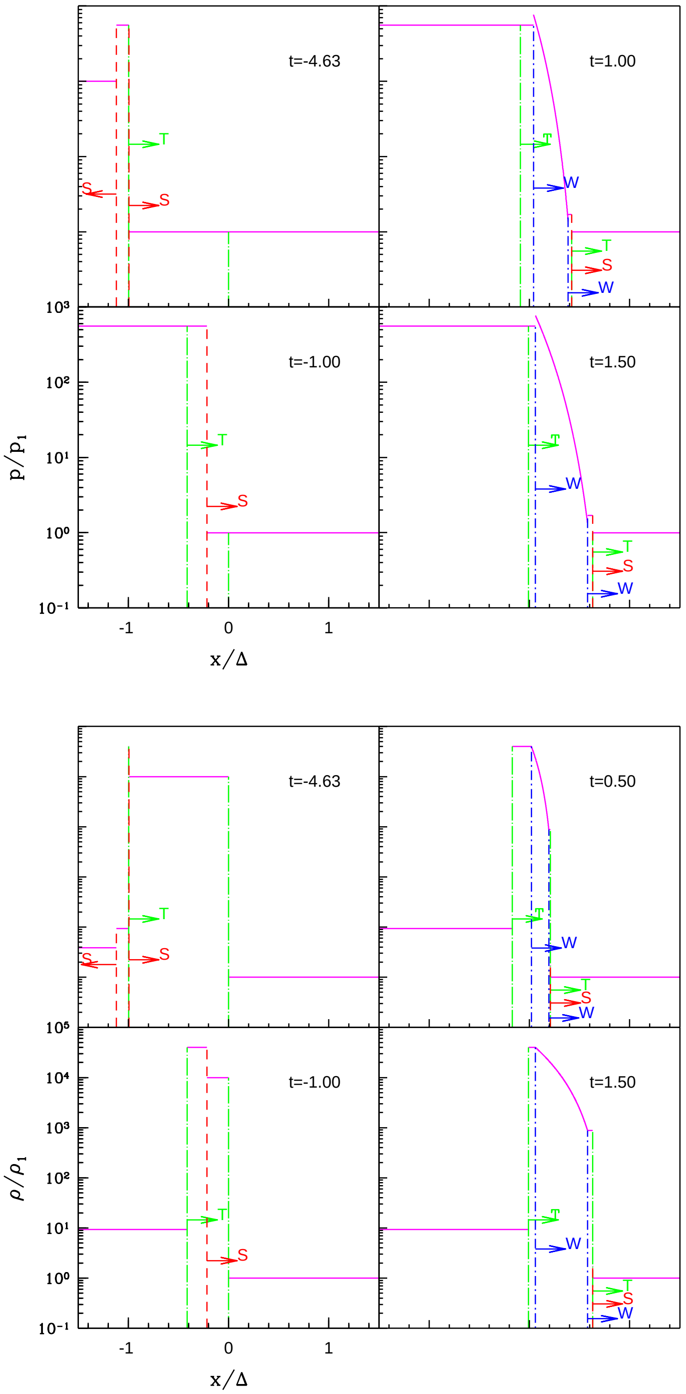

Figure V.5: Variation of the pressure p and density ρ (with respect to the initial pressure p_1 and density ρ_1 of the environment) as a function of position x (normalised to the initial width of the cloud Δ) and dimensionless time t (in units of the time Δ/c_1 –where c_1 is the speed of sound in the external medium). Dashed lines represent shock waves (S), dot-dashed lines are tangential discontinuities (T), which are boundaries of the cloud, and short-long dashed lines represent weak discontinuities (W), which bound a rarefaction wave. The system of reference was chosen so that gas far away to the right of the diagram is at rest. The diagram shows the case for which $\rho_c/\rho_1 = 10^4$, and the polytropic indices correspond to a monoatomic gas.

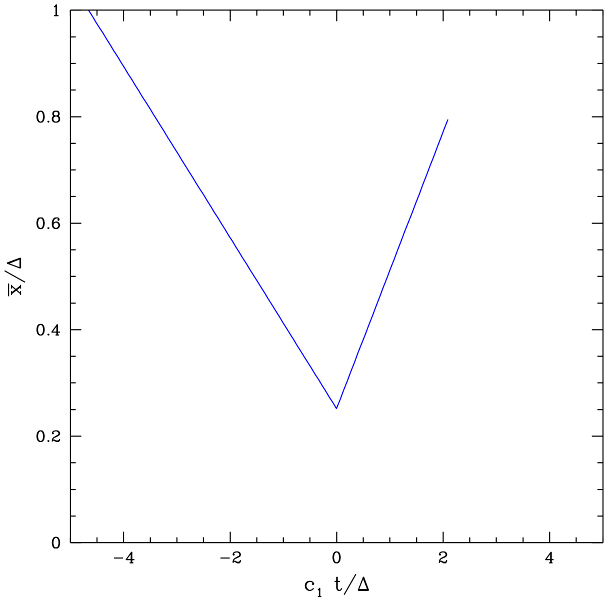

Figure V.6: Variation of the width of the cloud in units of its original size Δ as a function of the dimensionless quantity $c_1 t/\Delta$. Where c_1 represents the sound speed of the gas for the external environment and t the time. The curve was produced under the assumption that $\rho_c/\rho_1 = 10^4$. The gas was considered to be monoatomic.

Chapter VI

Astrophysical Applications

In the previous chapters we have analysed two types of interactions of radio jets with their surroundings. The radius of the jet being assumed to be much smaller than the radius of the cloud. Firstly, the steady passage of the jet through a dense stratified cloud and the consequences on its structure were discussed in Chapters III and IV. The overall structure of the cloud is not changed as a result of the interaction. Secondly, in Chapter V, the collision of a shock wave with a dense stratified region in one dimension was analysed. This is related to the initial stages of the interaction between the shock wave associated with the head of an expanding jet and a cloud. In this case, the overall structure of the cloud varies with time.

The present Chapter discusses the consequences of the results obtained so far and applies them to astronomical sources.

§32 Radio trail sources

As it was mentioned in section §5, radio trail sources show considerable "real" bending of their jets with deflection angles of about 90 ° in many cases. Fig.(I.3) and fig.(VI.1) show two typical examples of these types of radio sources. As can be seen from both of them, the jets follow semicircular paths and bend up to about 90 °. The jets seem to loose collimation after the complete bending has occurred.

Since it is the proper motion of the host galaxy with respect to the intergalactic medium that produces the curvature of the jets, the deflection angle cannot be greater than 90 °. The results presented in eq.(25.7) show that jets which have a relativistic equation of state and a bulk relativistic motion of the gas within its jet, cannot be deflected more than $\sim 50\,^\circ$. Since the deflections of radio trail sources are greater than this value, this result implies that most radio trail sources generate shocks at the end of their curvature. However, observations (see for example Eilek et al., 1984; O'Dea, 1985; de Young, 1991, and references within) show that the velocity of the material of the jets $\lesssim$ 0.2–0.3c. Therefore, the bulk motion of the flow is non–relativistic, despite the fact that the gas inside the jet has a relativistic equation of state. The calculations which resulted in eq.(25.7) can be

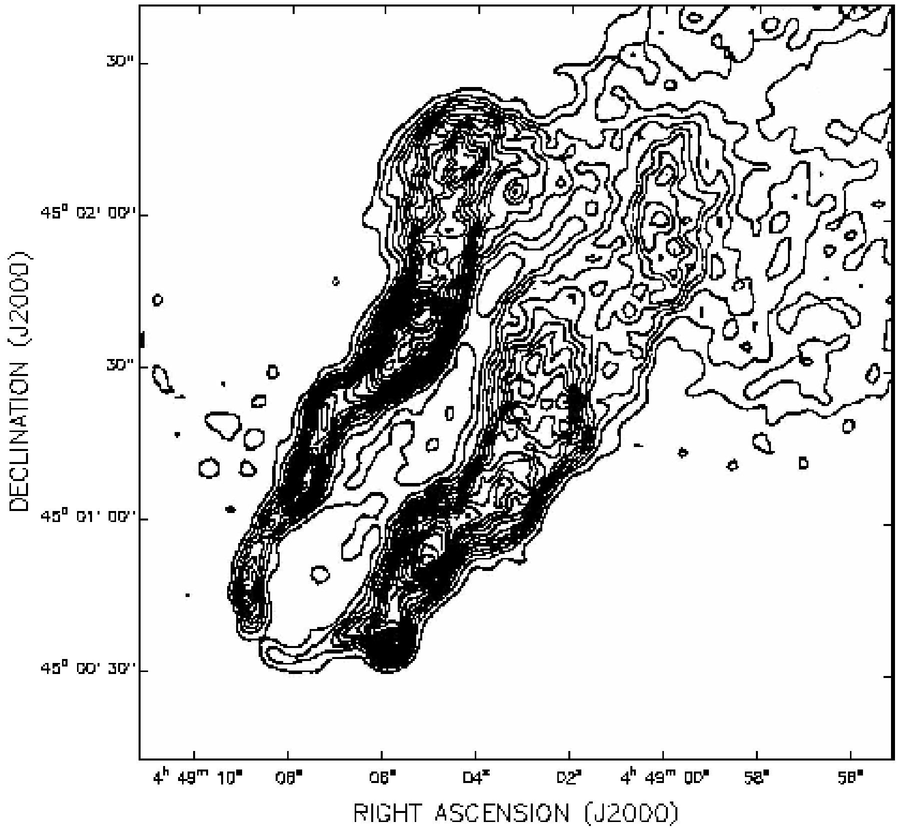

Figure VI.1: Radio trail galaxy 3C 129. The image is an NVSS (Condon et al., 1998) radio map with peak flux of $7.5414 \times 10^{-2}\,\mathrm{Jy\,beam}^{-1}$. The levels are at $7.5414 \times 10^{-4} \times (-5, 10, 15, \ldots, 95)$ (Leahy & Yin, 2000).

repeated for this circumstances. To do this, a polytropic index of 4/3 in the calculations made in section §25 has to be used for the classical case. The result is that (Icke, 1991):

$$\theta_{\mathrm{max}} = 134.16\,^{\circ}. \tag{32.1}$$

In other words, these type of jets will develop a terminal shock if their jets bend more than ~135 °. This seems to be the reason why all radio trail sources are able to bend so much without disrupting their internal structure.

As was discussed in section §25, the value of the bending angle in eq.(32.1) is an upper limit. The formation of an internal shock depends on the particular trajectory that a jet follows. In order to see if a specific jet will develop a shock at the onset of its curvature, the upper plot made in fig.(IV.4) is repeated in fig.(VI.2) for the case in which the polytropic index of the flow inside the jet has a value of 4/3.

In order to find out whether radio trail galaxies generate internal shocks at the onset of their curvature due to the deflection of their jets, we can make use of eq.(5.1), which can be rewritten as:

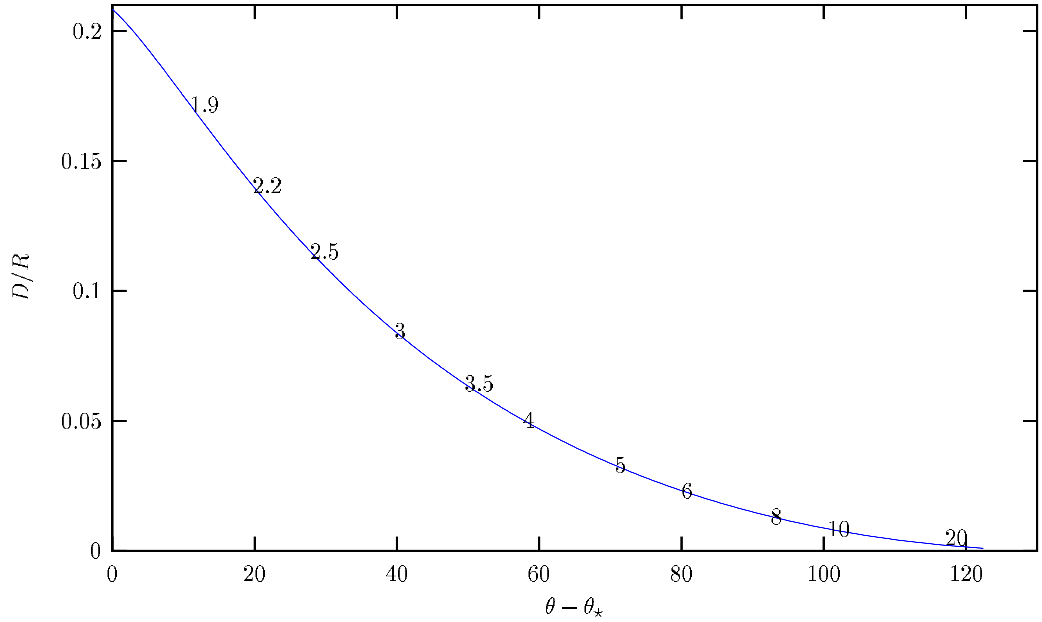

Figure VI.2: Plot of the maximum ratio D/R (D is the with of the jet and R is the radius of curvature of the curved trajectory it follows) as a function of the difference $\theta - \theta_\star$, where θ is the deflection angle and $\theta_\star$ is the maximum allowed bending angle a jet can have in order not to produce a terminal shock. This plot is similar to the ones produced in Chapter IV (see fig.(IV.4)). The trajectory of the jet was assumed to be a circumference and the plot refers to parameters such that a shock at the onset of the curvature is produced. Jets with parameters such that their values lie down below the curve are stable against the generation of internal shock waves at the beginning of the trajectory. This plot differs from the ones presented in fig.(IV.4) in that the polytropic index in the flow of the gas inside the jet is assumed to be 4/3 and the bulk motion of the flow inside the jet is considered to be non–relativistic (Icke, 1991). The numbers in the plot label the different values of the Mach number that the flow has.

$$\frac{D}{R} = \frac{\rho_e v_g^2}{\rho_j v_j^2}. \tag{32.2}$$

In this relation D and R represent the width of the jet and the radius of curvature of its trajectory respectively. The right hand side of this equation can be calculated from observations. However, it is important to mention that it is difficult to know the precise value of the width of the jet D since it is not clear in most observations that the jet is resolved. It is also difficult to fit the radius of curvature of the source because of projection effects. Nevertheless, the symmetric U shape from typical radio trail galaxies imply that the sources do not lie too far away from the plane in the sky and so, the obtained value for the radius of curvature should not differ too much from its real one. The fraction on the left hand side of this relation is the abscissa of the plot in fig.(VI.2). Typical values (Forman & Jones, 1982; Eilek et al., 1984; de Young, 1991) for radio trail galaxies, obtained using a mixture of observations and various different theoretical models for radio trail galaxies, are: a density of the intergalactic medium $n_e \sim 10^{-3}\,\mathrm{cm}^{-3}$, velocity of the host galaxy $v_g \sim 10^2\,\mathrm{km\,s}^{-1}$, particle number density of the jet $n_j \sim 10^{-1}\,\mathrm{cm}^{-3}$ and a jet velocity $v_j \sim 10^4\,\mathrm{km\,s}^{-1}$. With these values, it follows that the ratio $D/R \sim 10^{-2}$. In other words, radio trail sources are typically far below the curve in fig.(VI.2) and they will not generate internal shocks at all. This is the reason why the jets in this type of radio sources can bend so much, maintaining their collimation and avoiding the generation of internal shocks.

Let us analyse in more detail the archetypical elliptical radio galaxy NGC 1265 (3C 83.1B) which lies in the outer parts of the Perseus cluster of galaxies (see fig.(I.4)). The radial velocity of this radio galaxy with respect to the mean velocity of the Perseus cluster is $\sim 2000\,\mathrm{km\,s}^{-1}$ and the Mach number of the flow is $M \sim 2$–4 (Begelman et al., 1979; O'Dea & Owen, 1987a). As can be seen from fig.(I.3), the total bending angle is $\theta \sim 80\,^\circ$. This is much less than the maximum allowed value of $\theta_{\mathrm{max}} \sim 135\,^\circ$ calculated in eq.(32.1). In other words, no terminal shock is present in the radio source. In order to see whether a shock at the onset of the curvature is present, we make use of eq.(32.2) and the observed values for NGC 1265 (Begelman et al., 1979; O'Dea & Owen, 1987b; de Young, 1991; Sijbring & de Bruyn, 1998) of $v_j \sim 10^5\,\mathrm{km/s}$, $n_j \sim 10^{-5}\,\mathrm{cm}^{-3}$, $v_e \sim 10^3\,\mathrm{km/s}$, and $n_e \sim 10^{-1}\,\mathrm{cm}^{-3}$. With these values, the ratio $D/R \sim 10^{-3}$. Comparison of this with the plot in fig.(VI.2) indicates that the jets do not generate an internal shock at the onset of the curvature.

The ratio D/R can also be calculated geometrically from the figures themselves. For example, let us take the case of the radio trail source NGC 1265 shown in fig.(I.4). As can be seen from the figure, two major deflections in each jet are observed. The first deflection is not very strong, and bends the jet only about 20 °. The second one takes the jet from this bent angle up to ~80 °. As was mentioned above, the value of 80 ° is less than the maximum possible bending angle calculated in eq.(32.1) and so, no terminal shock is produced. From fig.(I.1) the ratio D/R at the onset of the curvature was calculated by fitting a circle to the trajectory using the nucleus of the radio source and two adjacent points around it. The width of the jet is calculated from the resolved image. It then follows that $D/R \sim 0.05$. This value is of the same order of magnitude as the value found above using eq.(32.2).

We can apply this geometrical technique to various different sources. Fig.(VI.1) shows an NVSS image of the radio source 3C 129. Just as in the radio galaxy NGC 1265, the jets seem to have two major deflections. The first curves the jets up to ~40 ° and the second deflects them to an angle of ~90 °. By taking three points on the first curved trajectory, the ratio $D/R \sim 0.07$. According to the diagram in fig.(VI.2) it follows that the jet will not develop a shock at the onset of the curvature. In other words, the jets in 3C 129 do not generate any internal shocks due to their bending.

§33 Bent jets in powerful radio sources

We have seen in the previous section how the jets in radio trail sources can be stable against the formation of internal shock waves generated because of their bending. Most powerful double radio sources, in particular radio galaxies and quasars show almost no deflection of their jets as they propagate through the interstellar and intergalactic medium. As we saw in Chapter III, this behaviour occurs because the bulk velocity of the flow inside the jet is highly relativistic (up to $0.99\,c$ in some cases according to observations). One of the best examples of this behaviour is the radio galaxy Cygnus A, shown in fig.(I.1). As can be seen in the image, the jet has a very well defined straight structure. However, when the jet approaches half the width of the radio lobe it seems to bend through $\sim 20\,^\circ$ and then goes on to the hotspots. In exactly the same way as it was done in the last section, the ratio D/R can be calculated and the result is that $D/R \sim 0.01$. This value lies well below the curve plotted in fig.(IV.4) for a bending angle $\sim 20\,^\circ$. This bending angle is also well below the upper limit of $\sim 50\,^\circ$ calculated in eq.(25.7). In other words, the deflection of the western jet in Cygnus A does not generate any internal shocks.

Fig.(VI.3) shows a VLA radio map of the FR I plumed radio galaxy 3C 31. The jets have large scale arcs before they bend an angle $\sim 30\,^\circ$. This angle is less than the maximum bending angle calculated in eq.(32.1) for a non–relativistic bulk motion of the flow. From the figure, the ratio $D/R \sim 0.1$ at the onset of the curvature, and the angle the jet bends at the onset of the curvature is $\sim 30\,^\circ$.

Applying the previous technique to radio quasars is somewhat more complicated due to orientation effects. According to unification models for strong radio sources, namely the 3CR radio quasars and radio galaxies (see section §3), the jets of radio quasars are observed within a cone of half–angle roughly $45\,^\circ$ to the line of sight. This means that whatever the deflection angle we observe on the plane of the sky, it would certainly differ from the real deflection. Figs.(VI.4)-(VI.5) show two radio quasars with very well defined deflections. Bearing in mind that the uncertainties in any calculation done for quasars with respect to their bending angle are most probably incorrect, in what follows, we discuss briefly the implications of this result.

In the case of the quasar 3C 175 shown in fig.(VI.4), the deflection angle is $\sim 25\,^\circ$ which is less than the maximum bending angle $\sim 50\,^\circ$ for relativistic flows. The ratio $D/R \sim 0.02$ and the deflection angle at the onset of the curvature is $\sim 15\,^\circ$. This pair of values lie well below the curve of the appropriate diagram of fig.(IV.4). For the quasar 3C 334 the total deflection angle is $\sim 40\,^\circ$. The ratio $D/R \sim 0.1$ and the bending angle at the onset of the curvature is $\sim 10\,^\circ$. According to eq.(25.7) and fig.(IV.4) this means that the jet does not generate internal shocks due to its deflection.

The radio galaxy 3C 34 at redshift $z = 0.69$ shown in fig.(VI.6) is very peculiar. Best et al. (1997) suggested that the western radio jet of this source has undergone a collision with a galaxy giving rise to a jet–galaxy interaction. In the top panel of fig.(VI.6), the

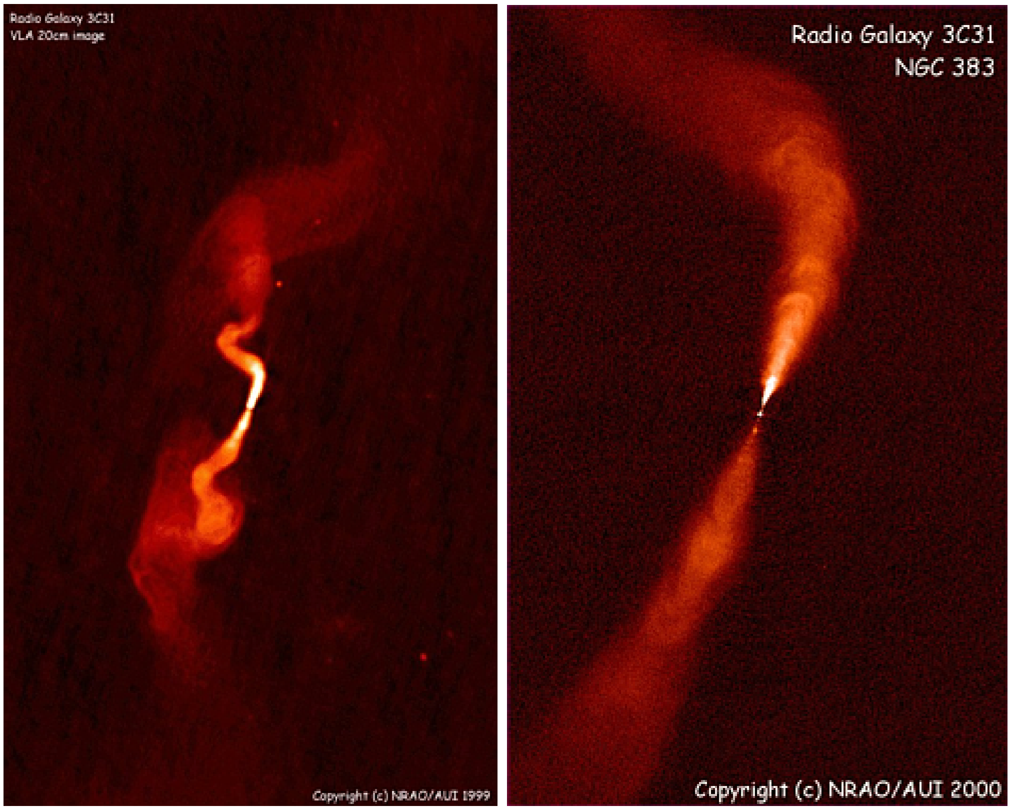

Figure VI.3: Radio Image of the radio galaxy 3C 31. This radio galaxy is an FR I (plumed) galaxy at a redshift $z = 0.0169$. The left image is a VLA 1.4 GHz radio image at 5.5 arcsec resolution. This image shows a large distortion (wiggling) of both plumes of the radio jet. The right image is a VLA 8 GHz radio image of the same radio source, but zoomed about the core. This image is a VLA radio map at 0.3 arcsec resolution. Both images taken from Laing et al. (2000); Bridle (2000).

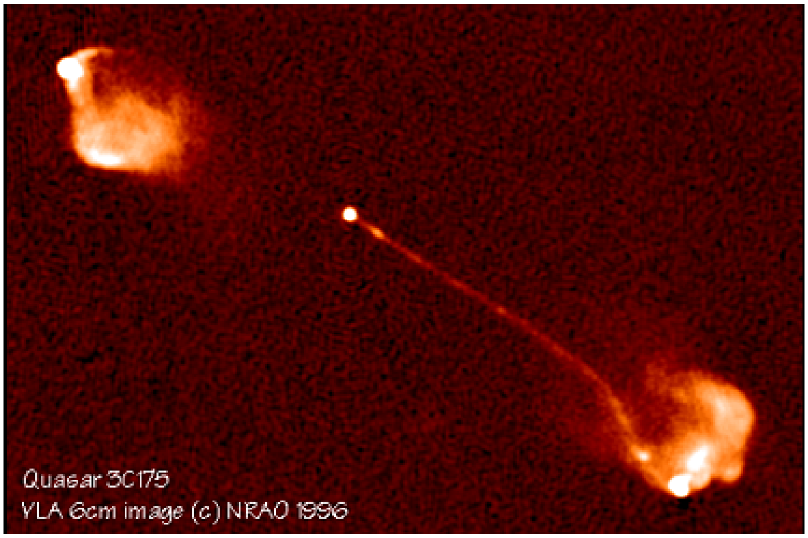

Figure VI.4: Radio Image of the quasar 3C 175. The quasar lies at a redshift of $z \sim 0.768$. The radio image was taken with the VLA at 4.9 GHz with 0.35 arcsec resolution (Bridle, 2000; Bridle et al., 1994).

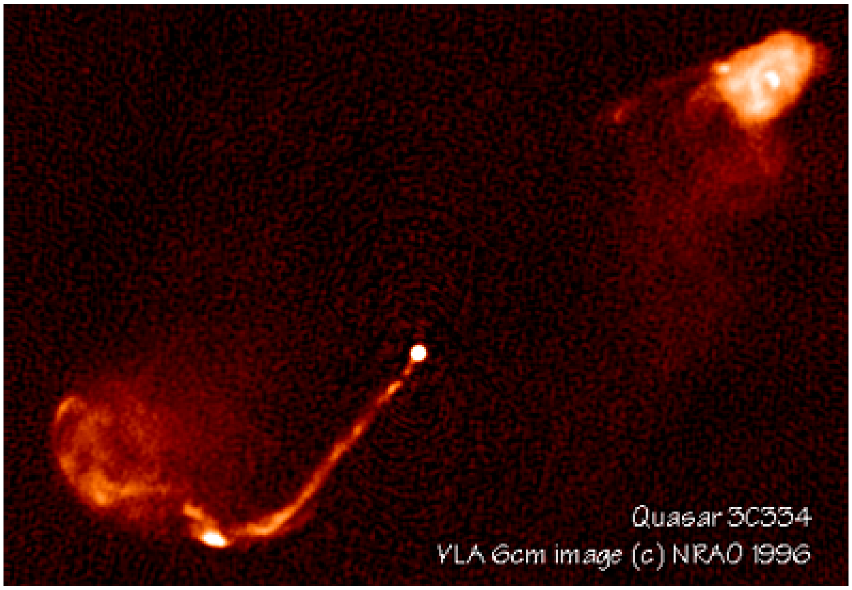

Figure VI.5: Radio Image of the quasar 3C 334. The quasar is at a redshift $z = 0.555$. This radio image was taken with the VLA at 4.9 GHz with 0.35 arcsec resolution (Bridle, 2000; Bridle et al., 1994).

emission regions labelled as n and s represent two hot spots in the western lobe of the source and the region a is what the authors identified as a galaxy which was assumed to be at the same redshift as 3C 34. The idea that object a is an ordinary galaxy in the cluster containing 3C 34 is very natural. First of all, this object presents an elongated structure along what appears to be one of the axes of the radio source (blue line in fig.(VI.6)). Secondly, the deep radio map (bottom map on fig.(VI.6)) shows an enhanced region of radio emission located to the north of object a. The radio spectral index of this area increases away from the hotspot and it is not as steep as the rest of the radio lobe. This means that this region shows a back flow emanating from the hotspot n (Blundell, 1994). This back flow seems to pass around the object a rather than through it, which is consistent with the idea that object a is in the same cluster of galaxies as the one 3C 34 belongs to.

The $1.4 - 5$ GHz spectral indices of hotspots s and n are 0.83 ± 0.03 and 0.92 ± 0.03 respectively. Since the spectral index is flatter for hotspot s, this suggests that it is younger as compared to hotspot n. For comparison, it is important to note that the spectral index of the eastern hotspot is 0.82 ± 0.03.

Cox et al. (1991) showed that a steadily precessing jet could initially make an impact on the wall of the cocoon producing a jet curvature as it feeds its primary hot spot. As the precession continues, the jet then interacts with the cocoon at a very sharp angle and it is then able to produce a new –primary– hotspot while still feeding the old –secondary– hotspot which is now located downstream. This scenario could be the explanation of the observed features in the radio galaxy 3C 34. With this model, the double hot spot and

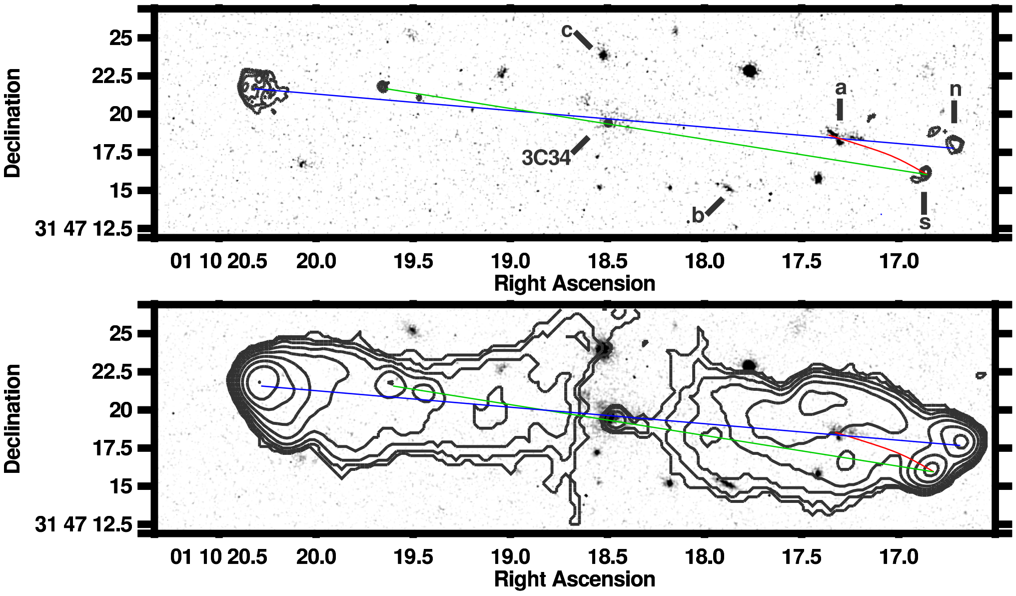

Figure VI.6: Optical image of the radio galaxy 3C 34 with VLA radio contours superimposed. Top: Image at 545 nm taken with the Hubble Space Telescope with overlaid radio contours at 8.4 GHz taken with the VLA A–Array. The contour levels are 120 μJy × (2, 4, 8, 16). Bottom: HST image at 865 nm with overlaid contours of the radio emission at 5 GHz as seen using the B and C arrays of the VLA. The contour levels are 120 μJy × (1, 2, 4, 8, 16, 32, 64, 128). Both images from Best et al. (1997). The blue line is what seems to be the old axis of the radio galaxy. The green one is what appears to be its current axis. The red line shows what the path of the west jet will be if a deflection of the jet would have been caused by the collision with the galaxy underlying the emission labelled a.

the difference in ages of their electron populations is automatically satisfied. This means also that the radio jet of 3C 34 was previously lying in the direction of the blue axis of fig.(VI.6) and that it is currently aligned with the green axis. The collision of the radio jet of 3C 34 with the galaxy underlying object a occurred when the jet was aligned with the blue axis and star formation was induced due to this interaction.

However, there is another scenario which could well explain the features observed in 3C 34. If the west radio jet collides with the galaxy underlying object a, this interaction could deviate the jet from its original trajectory, as it is pictorially represented by the red curved line in fig.(VI.6). The appearance of a double hot spot could then be explained as follows: originally, the western jet was lying along the blue line of fig.(VI.6) and the proper motion of the orbital companion object a in the cluster resulted in it intersecting the path of the jet which made it follow a curved trajectory such as that shown by the red line. It could also have been that the precession of the jet eventually interacted with object a giving rise to the observed deflection. No radio jet has been observed, but the narrow width of the object a would be consistent with values of $D/R \lesssim 0.01$.

If the jet in 3C 34 was bent because of the interaction with a typical galaxy for which its gas is in pressure equilibrium with a dark matter halo, then we can use the standard values presented in section §21. First of all, the western jet in 3C 34 has a bending angle $\theta \sim 10\,^{\circ}$, so that the deflection angle $\psi \sim 170\,^{\circ}$. If we assume that the flow inside the jet moves with a velocity $v = 0.99c$, it follows from the bottom diagram in fig.(III.8) that $\sin \varphi_0 \sim 0.3$, or $\varphi_0 \sim 17\,^{\circ}$. On the other hand, the value $\theta \sim 10\,^{\circ}$ is well below the upper limit of $\sim 50\,^{\circ}$ calculated in eq.(25.7), so that at least no terminal shock will be produced by the deflection of the jet. From the bottom plot of fig.(IV.4) and because the angle $\theta_{\star} \ll 1$ for a high relativistic flow, it follows that if the trajectory of the jet in 3C 34 is circular, then in order not to produce an internal shock at the onset of the curvature, the ratio D/R has to be less than $\sim$0.08.

§34 Discontinuities in jet–cloud collisions

As it was discussed in Chapter V the one dimensional collision between a shock and a cloud generates two types of strong discontinuities: shock waves and rarefaction waves. It still remains an open question as to how good these solutions are for understanding the more general three dimensional case. At least it should be expected that far away from the boundaries of a spherical cloud, where the interaction can be considered plane–parallel the solution should not differ too much from the one dimensional case.

When the two dimensional case is considered, more strong discontinuities (shocks) are generated and the cloud is unstable due to the generation of Raleigh–Taylor and Kelvin–Helmholtz instabilities (Klein et al., 1994). This is seen analytically as follows.

When a shock wave propagates through the interstellar or intergalactic medium with a velocity v_b and collides with a cloud, it drives a shock wave into it (cf. Chapter V). Let us assume that the incoming shock is strong so that the Mach number $M \gg 1$. Under this circumstances, the postshock pressure is about $\rho_e v_b^2$ (Landau & Lifshitz, 1995), with ρ_0 being the density of the external medium around the cloud. In the same way, the pressure behind the shock in the cloud is about $\rho_c v_s^2$, where ρ_c is the original density of the cloud, and v_s is the the shock velocity inside the cloud. These two pressures most be comparable, and so (Bychkov & Pikelner, 1975; McKee & Cowie, 1975; Klein et al., 1994):

$$v_s \simeq \frac{v_b}{\sqrt{\chi}}, \tag{34.1}$$

where $\chi \equiv \rho_c/\rho_e$ is the *density contrast* between the cloud and the intercloud environment. The time for the shock in the intercloud medium to sweep across the cloud is:

$$t_{ic} \equiv \frac{2\Delta_0}{v_b}, \tag{34.2}$$

in which Δ_0 is the initial radius of the cloud. The characteristic time for the cloud to be "*crushed*" by the shocks inside the cloud is Δ_0/v_s. From this and eq.(34.1) it follows that the *cloud crushing time* is:

$$t_{cc} \equiv \frac{\chi^{1/2}\Delta_0}{v_b}. \tag{34.3}$$

After the blast wave has swept over the cloud, the shocked cloud is subject to both, Kelvin–Helmholtz and Rayleigh–Taylor instabilities (Klein et al., 1994). For $\chi \gg 1$ the timescale t_{KH} for the growth of Kelvin–Helmholtz instabilities for perturbations of wavenumber k parallel to the relative velocity v_{rel} between the cloud and intercloud media is $t_{KH}^{-1} = k v_{rel}/\chi^{1/2}$ (Chandrasekhar, 1961; Klein et al., 1994). In other words, the Kelvin–Helmholtz growth time is comparable to the cloud crushing time:

$$\frac{t_{KH}}{t_{cc}} = \frac{v_b/v_{rel}}{k\Delta_0}. \tag{34.4}$$

Short wavelengths have a fast growth, but longer wavelengths ($k\Delta_0 \sim 1$) are far more disruptive.

The blast wave accelerates the cloud in two stages (Klein et al., 1994). Firstly, the cloud shock accelerates it to a velocity v_s. Secondly, the flow of shocked intracloud gas accelerates it until it is comoving with the flow behind the incoming shock, which for a monoatomic gas has a velocity of $3v_b/4$. For a large density contrast, the cloud shock velocity is small and the acceleration is dominated by the second stage. Let v_c be the mean velocity of the cloud, v_{i1} the velocity of the shocked intercloud medium and $v'_c = |v_{i1} - v_c|$ the magnitude of the velocity of the cloud relative to the shocked intercloud medium. With these, the equation of motion of the cloud can be written (Klein et al., 1994; Landau & Lifshitz, 1995):

$$m_c \frac{dv'_c}{dt} = -\frac{1}{2} C_D \rho_{i1} v'^2_c A, \tag{34.5}$$

where m_c is the mass of the cloud, $C_D \sim 1$ is the drag coefficient, $\rho_{i1} \sim 4\rho_0$ is the density of the shocked intercloud medium and A is the cross section area of the cloud. If this cross section remains constant then $A \approx \pi\Delta_0^2$ and the mass of the cloud $m_c \approx \rho_c V_c$ in which the volume of the cloud $V_c \propto \pi\Delta_0^3$. Since the velocity $v'_c \sim v_b$, it follows that eq.(34.5) defines a characteristic drag time $t_{drag,0}$ for a strong shock given by (Klein et al., 1994):

$$t_{drag,0} = \frac{\chi\Delta_0}{C_D v_b} = \frac{\chi^{1/2} t_{cc}}{C_D}. \tag{34.6}$$

The deceleration of the cloud initially proceeds on the drag timescale $t_{drag,0}$. This gives a deceleration $g \simeq v_b/t_{drag,0}$, which corresponds to a Rayleigh–Taylor growth time given by $t_{RT}^{-1} \simeq \sqrt{gk}$ (Chandrasekhar, 1961). This instability has a growth time of the order of the cloud crushing time (Klein et al., 1994):

$$\frac{t_{RT}}{t_{cc}} \simeq \frac{1}{(k\Delta_0)^{1/2}}. \tag{34.7}$$

The above results suggest that the cloud will be destroyed in a time related to the cloud crushing time. In fact, numerical simulations carried out by Nittmann, Falle & Gaskell (1982) and Klein, McKee & Colella (1994) show that the cloud destruction time is indeed a few times the cloud crushing time.

The two dimensional problem of the collision between a shock wave and a cylindrical cloud of constant density can be described as follows according to numerical simulations (Klein et al., 1994). Four stages can be identified in the collision. (i) When the incoming plane parallel shock wave hits the cylindrical cloud two shocks are formed. One penetrates the cloud and another one is reflected from the point of impact (cf. Chapter V). The reflected shock settles into a standing bow shock in a time of the order $\Delta_0/v_b = t_{ic}/2$. (ii) The next stage is *shock compression* of the cloud. After a time $\sim t_{ic}$ the flow around the cloud converges on the axis behind the cloud, producing a high pressure reflected shock in the intercloud medium and driving a shock into the rear of the cloud. The shocks produced at the sides of the cloud are weaker than those at the front and the back of the cloud. This is due to the fact that the pressure is a minimum at the sides of the cloud. As a result of all this, the cloud is compressed into a thin pancake, with its traverse dimension reduced by a factor of 2. The collision of the transmitted shock into the cloud with the shock coming from the rear produces further compression. (iii) When the shock transmitted into the cloud reaches the opposite side of the cloud it transmits a shock to the intracloud medium and reflects back a rarefaction wave. This produces the so called *reexpansion stage*. At the same time, the low pressure at the sides of the cloud compared to that on the axis causes the cloud to expand laterally. This lateral expansion continues up to a time of a few cloud crushing times. (iv) Finally, instabilities and differential forces due to the flow of the intercloud gas past the cloud makes the last stage: *cloud destruction*. This causes the cloud to fragment.

As it is seen from the above discussion and from the results presented in Chapter V, the one dimensional case and the two dimensional one are quite different. This is mainly due to the fact that in the two dimensional case the cloud is of a finite size (cylindrical cloud) whereas in the one dimensional case it is not (plane parallel cloud). However, the most important strong discontinuities (shocks and rarefaction waves) are produced in both cases. From the results of Chapter V it follows that the pressure behind the transmitted shock (for a large density contrast) should be about six times the pressure in the intercloud medium, as would be expected from the reflection of a strong shock with a solid wall (Spitzer, 1982; McKee, 1988). However, such a high pressure has not been seen in the numerical simulations by Bedogni & Woodward (1990) and Klein, McKee & Colella (1994). It seems that this high pressure exists only as the flow is one dimensional or it does happen for such a short time that it does not show up in the simulation.

Despite all of these differences, the perturbed solution found in Chapter V serves as an upper limit to values of pressures, densities and temperatures and provides a very simple way of understanding the behaviour of the collision between a shock wave and a cloud in detail.

An important use of the results presented in Chapter V is to compare the cooling time behind the transmitted shock wave to the shock crossing time. Let us assume that the density contrast is 10^4 (see section §6) and that the shock that penetrates the cloud after the first initial discontinuity compresses the gas $\sim 5 \times 10^2$ of its original value, as shown pictorically in fig.(V.5). The density in the cloud increases by a factor of ~ 3 with the passage of the shock wave. The temperature of the cloud is enhanced by a factor of $\sim 1.6 \times 10^4$ of its original value. In other words, if we assume that the temperature of the cold clouds is $\sim 10^4\,\mathrm{K}$, then the passage of the shock wave is able to increase this value to $\sim 10^8\,\mathrm{K}$. The dissipation of the heated gas in the cloud, that is, its energy loss produced by radiation can be calculated from calculations made by Silk & Wyse (1993); Sutherland & Dopita (1993) and described by Longair (1998). If the cooling function Λ is measured in $\mathrm{ergs\,cm^3\,s^{-1}}$, then $dE/dt = -n^2\Lambda(T)$ is the energy loss rate per unit volume in which E is the energy of the system, t time, n the particle number and T the temperature of the gas. From the results presented in Longair (1998), it follows that $\Lambda(T \sim 10^8\,\mathrm{K}) \approx 10^{-23}\,\mathrm{ergs\,cm^3\,s^{-1}}$. The cooling time $\tau_{\mathrm{cool}} \equiv E/|dE/dt|$ is then given by $\tau_{\mathrm{cool}} \sim 10^3\,\mathrm{yr}$, where we have used the fact that $E = 3nk_BT$ for a fully ionised gas, k_B is the Boltzmann constant and the particle number density of clouds needed for the radio alignment effect is $n_{\mathrm{cloud}} \sim 10^3\,\mathrm{cm}^{-3}$ (Best et al., 2000).

The time it takes the incoming shock with velocity v_s to cross a cloud of width Δ is $\tau_{\mathrm{cross}} = \Delta / v_s$. Typical values for the advance speed of a jet in a radio source are $v_s \sim 0.1c$. The characteristic size of a cloud needed to produce the observed radio–optical alignment effect is about 1 kpc. This implies that the crossing time is $\tau_{\mathrm{cross}} \sim 10^4\,\mathrm{yr}$. In other words $\tau_{\mathrm{cool}} \sim \tau_{\mathrm{cross}}$, so thermal instabilities are likely to develop inside the cloud. Because of this, if a shock wave associated with an expanding jet in a radio source interacts with a set of clouds in the interstellar and intergalactic medium, it is possible that the optical emission observed in the alignment effect in radio galaxies is produced.

Summary and conclusions

The interaction of the jets on extragalactic double radio sources has been the central theme of this work. In Chapter I it was discussed that "*real*" bending of jets, ie. bending not produced by projection effects, can be achieved by two mechanisms. Firstly, ram pressure produced by a *wind* in the intergalactic medium is able to bend jets which are non–relativistic. This causes the jets to have a semicircular, or *U*, shape with the host galaxy in the pole. Radio galaxies which have this structure are called *radio trails*. Secondly, deflections of jets can be achieved if jets pass through a stratified high density region. In this case it is the gradients of the pressure that make the jet to follow a non–straight trajectory. Gravitational effects might be important on the deflection of jets depending on the mass of the stratified density region.

In order to understand this second possibility, the hydrodynamical interaction between a jet and a cloud was analysed in detail, once the steady state has been reached. This was carried out in two steps.

In the first case, the bulk motion of the flow in the jet was assumed to be non–relativistic and the self gravity of the gas in the cloud acting on the jet was included in the description of the problem. Because the jet was assumed to expand adiabatically it was possible to calculate the trajectory of the jet by means of an energy equation (Bernoulli's law). In addition, assuming that the jet Mach number was sufficiently high, analytic solutions to the problem were found for the cases in which the cloud was assumed to be an isothermal sphere and when it was considered to be a gas in hydrostatic equilibrium with a galactic dark matter halo. Dimensional analysis showed that when gravity is included in the relevant equations, the whole problem is described by the initial dimensionless Mach number inside the jet M_0 and the polytropic index κ of the gas in the jet. Gravity, through the gravitational constant G, adds another dimensionless parameter $\Lambda \equiv G\rho_0 r_0^2 / M_0^2 c_0^2$ when the stratified density region is an isothermal sphere and ρ_0 is the density of the cloud at the radius r_0, where the jet penetrates it. The Mach number at this point is M_0 and the velocity of sound in the cloud is c_0. The parameter Λ is an indicator of how large the deflections produced by the gravitational field of the isothermal sphere are from its straight trajectory. The greater Λ, the more curved the trajectory is. In contrast, when the cloud is assumed to be a sphere of gas in hydrostatic equilibrium with a dark matter halo in a galaxy, the problem also involves the dimensionless number $k \equiv -4\pi G \rho_{d_\star} a^2 / c_\star^2$. The core radius is represented by a, the density of the dark matter halo at its centre is

$\rho_{d_\star}$, and the velocity of sound is $c_\star$. Just as in the previous case, the parameter k is an indicator as to how big deflections induced by the pressure gradients in the gas around the dark matter halo are.

The parameter Λ has the following physical meaning. Because Λ has the same value of $10^{-2}/M_0^2$ for galactic jets embedded in molecular clouds and extragalactic jets inside cluster of galaxies, this result provides a clue as to why jets in such different environments as giant molecular clouds and the gaseous haloes of clusters of galaxies have similar properties.

In the second case, the bulk motion of the jet was considered to be relativistic, but the gravitational effects induced by the gas in the cloud were not taken into account. Under the same assumptions as in the non–relativistic case, it was possible to show that the trajectory of jets is also determined by the relativistic version of Bernoulli's equation. Analytic solutions for jet velocities with a high relativistic Mach number were found for an isothermal sphere cloud and for gas in pressure equilibrium with a dark matter halo. Since the flow inside the jet was assumed to have an ultrarelativistic equation of state, the only parameter that plays an important role in the solutions is the initial velocity of the flow.

In both, the relativistic and non–relativistic cases, the solutions are extremely sensitive to variations in velocity. This occurs because the pressure and gravitational force fields applied to a certain fluid element in the jet are the same at a given position. However, as the velocity of the flow in the jet increases, there is not enough time for this force to change the curvature of the jet fast enough, giving rise to very straight jets.

When supersonic flow bends, its characteristics intersect at a certain point in space. Since the hydrodynamical quantities have a constant value on characteristic lines, this means that the point of intersection is such that the value of every hydrodynamical quantity is multivalued. This situation cannot happen in nature and a shock wave is created in order to bypass it. In Chapter IV the problem of the formation of shock waves inside bent jets was analysed in detail. If the intersection of the characteristic lines occurs outside the jet, the jet bends without any generation of internal shock waves. However, if this intersection occurs inside the jet, a shock wave forms and it is potentially dangerous to the jet. This is because behind a shock wave the normal component of the velocity is subsonic and collimation can not be achieved. By using a relativistic generalisation of steady simple waves in classical fluid dynamics, it was possible to describe in detail the generation of shock waves inside a jet due to this mechanism.

The proper Mach number in a supersonic flow that bends through a continuous curved trajectory decreases along its path. This implies that at some point, when $M \gtrapprox 1$, the rate of change of the Mach angle with respect to the bending angle increases without limits. This means that the characteristic lines tend to intersect at the end of the bending, when the flow is near the transonic point. Jets with Mach numbers between this lower limit and the maximum allowed value ($M = \infty$) do not generate shocks at the end of the curvature.

The difference between the bending angles evaluated at these last two values of the Mach number give upper limits for the bending angle of jets. For instance, it was shown in Chapter IV that for non–relativistic bulk motion of jets with a polytropic index of 5/3, appropriate to Herbig–Haro jets, this limiting angle has a value of $\sim 75\,^{\circ}$. However, if the polytropic index has a value of 4/3, for example radio trail sources, the upper limit for the bending angle is $\sim 135\,^{\circ}$. Relativistic bulk motion of jets with a polytropic index of 4/3, appropriate for classical double radio sources, have an upper limit of $\sim 50\,^{\circ}$. The reason why relativistic jets can bend less than non–relativistic ones is because the region of transmission of information from a perturbation, bounded by characteristics, is closer to the streamlines in relativistic flow. This increases the chances of an intersection of the characteristics as the jet bends.

In Chapter I the radio–optical alignment effect in powerful double radio sources was discussed. The optical radiation shows an alignment with the radio source axis rather than an elliptical structure. The effect fades away as the sources grow larger ($\sim 10\,\mathrm{Myr}$) and small sources ($\sim 50\,\mathrm{kpc}$) show strongest aligned optical structures. The morphology, kinematics and ionisation properties of the emission line gas of these small radio sources are dominated by the intense effect of shock waves associated with the expansion of the radio jet through the interstellar and intergalactic medium. It seems that cold clouds ($\sim 10^4\,\mathrm{K}$) embedded in the intergalactic and extragalactic medium of the host galaxy are able to interact with the bowshock of the expanding radio source in such a way as to generate sufficient strong shock waves in this interaction to produce the shock ionisation observed.

In Chapter V the one dimensional interaction between a shock and a cold high density region bounded by two tangential discontinuities (a cloud) was analysed in detail. It was shown that as a result of the interaction a discontinuity in the initial conditions was formed and a penetrating shock wave into the cloud and a reflected shock were produced. The shock wave that penetrates the cloud is able to hit, accelerate and compress the cloud until it reaches its opposite boundary giving rise to another (second) initial discontinuity. As a result, a shock wave is transmitted to the external medium and a rarefaction wave bounded by two tangential discontinuities is reflected back to the cloud. The rarefaction wave re–expands and cools the cloud. The important conclusion of this analysis is that most of the energy that the incoming shock was carrying before the collision is injected to the cloud. Very little energy is transmitted to the other side of the cloud, regardless of the strength of the original incoming shock.

Bibliography

ALFVEN, H. & HERLOFSON, N., 1950. Cosmic Radiation and Radio Stars. *Phys. Rev.*, **78**, 616.

ANTONUCCI, R. R. J. & MILLER, J. S., 1985. Spectropolarimetry and the nature of NGC 1068. *ApJ*, **297**, 621–632.

BAADE, W. & MINKOWSKI, R., 1954. Identification of the Radio Sources in Cassiopeia, Cygnus a, and Puppis a. *ApJ*, **119**, 206+.

BACHILLER, R., GUILLOTEAU, S., DUTREY, A., PLANESAS, P. & MARTIN-PINTADO, J., 1995. The jet-driven molecular outflow in L 1448. CO and continuum synthesis images. *Astronomy and Astrophysics*, **299**, 857–868.

BARTHEL, P., 1989a. Quasars and Radio Galaxies may BE Two of a Kind. *Scientific American*, **260**, 20+.

BARTHEL, P. D., 1989b. Is every quasar beamed? *ApJ*, **336**, 606–611.

BEDOGNI, R. & WOODWARD, P. R., 1990. Shock wave interactions with interstellar clouds. *Astronomy and Astrophysics*, **231**, 481–498.

BEGELMAN, M., BLANDFORD, R. & REES, M., 1984. Theory of extragalactic radio sources. *Rev. Mod. Phys.*, **56**, 255.

BEGELMAN, M. & CIOFFI, D., 1989. Overpressured cocoons in extragalactic radio sources. *ApJ*, **345**, L21.

BEGELMAN, M. & REES, M., 1996. *Gravity's fatal attraction. Black holes in the universe*. Scientific American Library, New York: W.H. Freeman.

BEGELMAN, M. C., REES, M. J. & BLANDFORD, R. D., 1979. A twin-jet model for radio trails. *Nature*, **279**, 770–773.

BEST, P. N., 1996. *The 3CR radio galaxies at redshift* $z{\sim}1$. Ph.D. thesis, Cavendish Laboratory, Cambridge University U.K.

BEST, P. N., CARILLI, C. L., GARRINGTON, S. T., LONGAIR, M. S. & ROTTGERING, H. J. A., 1998. Deep radio observations of 3C 324 and 3C 368: evidence for jet-cloud interactions. *MNRAS*, **299**, 357–370.

Best, P. N., Longair, M. S. & Rottgering, H. J. A., 1996. Evolution of the aligned structures in z~1 radio galaxies. *MNRAS*, **280**, L9–L12.

Best, P. N., Longair, M. S. & Rottgering, H. J. A., 1997. A jet-cloud interaction in 3C 34 at redshift z=0.69. *MNRAS*, **286**, 785–794.

Best, P. N., Röttgering, H. J. A. & Longair, M. . S., 2000. Ionization, shocks and evolution of the emission-line gas of distant 3CR radio galaxies. *MNRAS*, **311**, 23–36.

Binney, J. & Tremaine, S., 1997. *Galactic Dynamics*. Princeton University Press.

Blandford, R., 1990. Physical Processes in Active Galactic Nuclei. In T.-L. Courvoisier & M. Mayor, eds., *Active Galactic Nuclei*, Saas-Fee Advanced Course 20, 161–275. Springer-Verlag, Les Diablerets.

Blandford, R. & Icke, V., 1978. A dynamical interpretation of the radio jet in 3C 31. *MNRAS*, **185**, 527–538.

Blundell, K. M., 1994. *Assymmetries in Radio Galaxies and Quasars*. Ph.D. thesis, Cavendish Laboratory, Cambridge University U.K.

Bridle, A., 2000. Alan Bridle's Image Gallery. Images availabe at `http://www.cv.nrao.edu/~abridle/images.htm`.

Bridle, A. H., Hough, D. H., Lonsdale, C. J., Burns, J. O. & Laing, R. A., 1994. Deep VLA imaging of twelve extended 3CR quasars. *Astronomical Journal*, **108**, 766–820.

Burns, J. O., 1986. Wide-angle tailed radio galaxies. *Canadian Journal of Physics*, **64**, 373–377.

Bychkov, K. V. & Pikelner, S. B., 1975. Interstellar density fluctuations and the disparity between the optical and X-ray velocities of supernova remnants. *Soviet Astronomy Letters*, **1**, 14–16.

Cantó, J. & Raga, A. C., 1996. The steady structure of a jet/cloud interaction - I. The case of a plane-parallel stratification. *MNRAS*, **280**, 559–566.

Cantó, J., Tenorio-Tagle, G. & Rozyczka, M., 1988. The formation of interstellar jets by the convergence of supersonic conical flows. *Astronomy and Astrophysics*, **192**, 287–294.

Chambers, K., Miley, G. & van Breugel, W., 1987. Alignment of radio and optical orientations in high-redshift radio galaxies. *Nature*, **329**, 15.

Chandrasekhar, S., 1958. *An introduction to the study of stellar structure*. Dover, 1st ed.

Chandrasekhar, S., 1961. *Hydrodynamic and hydromagnetic stability*. International Series of Monographs on Physics, Oxford: Clarendon, 1961.

Chiu, H. H., 1973. Relativistic gas dynamics. *Physics of Fluids*, **16**(6), 825–830.

Christiansen, W. A., Pacholczyk, A. G. & Scott, J. S., 1981. On the energetics and morphology of radio tail galaxies. *ApJ*, **251**, 518–522.

Condon, J. J., Cotton, W. D., Greisen, E. W., Yin, Q. F., Perley, R. A., Taylor, G. B. & Broderick, J. J., 1998. The NRAO VLA Sky Survey. *Astronomical Journal*, **115**, 1693–1716. URL `http://www.cv.nrao.edu/~jcondon/nvss.html`.

Courant, R. & Friedrichs, K., 1976. *Supersonic Flow and Shock Waves*. Applied mathematical sciences; vol.21. Interscience Publishers.

Cox, C. I., Gull, S. F. & Scheuer, P. A. G., 1991. Three-dimensional simulations of the jets of extragalactic radio sources. *MNRAS*, **252**, 558–585.

Curtis, H. D., 1918. The planetary nebulae. *Publications of Lick Observatory*, **13**, 55–74.

de Young, D. S., 1986. Mass entrainment in astrophysical jets. *ApJ*, **307**, 62–72.

de Young, D. S., 1989. Star formation in radio galaxies at large redshift. *ApJL*, **342**, L59–L62.

de Young, D. S., 1991. The deflection of cosmic jets. *ApJ*, **371**, 69–81.

Eilek, J. A., Burns, J. O., O'Dea, C. P. & Owen, F. N., 1984. What bends 3C 465? *ApJ*, **278**, 37–50.

Fabian, A., 2000. Astronomy Picture of the Day (aop). For evidence for cooling flows in the Perseus cluster of galaxies see `http://antwrp.gsfc.nasa.gov/apod/ap001031.html`.

Falle, S. A. E. G., 1991. Self-similar jets. *MNRAS*, **250**, 581–596.

Forman, W. & Jones, C., 1982. X-ray-imaging observations of clusters of galaxies. *Ann. Rev. Ast. & Ast.*, **20**, 547–585.

Gradshteyn, I. S. & Ryzhik, I. M., 1994. *Table of integrals, series and products*. New York: Academic Press, 5th ed.

Hartmann, L., 1998. *Accretion processes in star formation*. Accretion processes in star formation / Lee Hartmann. Cambridge, UK ; New York : Cambridge University Press, 1998. (Cambridge astrophysics series ; 32) ISBN 0521435072.

Higgins, S. W., O'Brien, T. J. & Dunlop, J. S., 1999. Structures produced by the collision of extragalactic jets with dense clouds. *MNRAS*, **309**, 273–286.

Icke, V., 1981. Kinematic evidence for precessing beams in 3C 129. *ApJL*, **246**, L65–L68.

Icke, V., 1991. From Nucleus to Hotspot. In P. A. Huges, ed., *Beams and Jets in Astrophysics*, 232–277. Cambridge University Press.

Jaffe, W. & Perola, G., 1973. Dynamical Models of Tailed Radio Sources in Clusters of Galaxies. *Astron. Astrophys.*, **26**, 423.

Jennison, R. C. & Das Gupta, M. K., 1956. The measurement of the angular diameter of two intense radio sources I. A radio interferometer using post-detector correlation [and] II. Diameter and structural measurements of the radio stars Cygnus A and Cassiopeia A. *ApJ*, **124**, 660–662.

Klein, R. I., McKee, C. F. & Colella, P., 1994. On the hydrodynamic interaction of shock waves with interstellar clouds. 1: Nonradiative shocks in small clouds. *ApJ*, **420**, 213–236.

Kolosnitsyn, N. I. & Stanyukovich, K. P., 1984. Relativistic Prandtl-Meyer flow. *PMM Journal of Applied Mathematics and Mechanics*, **48**(1), 96–98.

Königl, A., 1980. Relativistic gas dynamics in two dimensions. *Physics of Fluids*, **23**(6), 1083–1090.

Kron, R., Longair, M. & Sandage, A., 1995. *The Deep Universe: Saas–Fee Advanced Course 23*, vol. xiv of *Lecture Notes 1993 Swiss Society for Astrophysics and Astronomy*. Berlin: Springer–Verlag.

Laing, R., Bridle, A., Perley, R., Feretti, L., Giovanni, G. & P., P., 2000. Data to be published.

Landau, L. & Lifshitz, E., 1994a. *The Classical Theory of Fields*, vol. 2 of *Course of Theoretical Physics*. Pergamon, 4th ed.

Landau, L. & Lifshitz, E., 1994b. *Statistical Physics*, vol. 5 of *Course of Theoretical Physics*. Pergamon, 3rd ed.

Landau, L. & Lifshitz, E., 1995. *Fluid Mechanics*, vol. 6 of *Course of Theoretical Physics*. Pergamon, 2nd ed.

Leahy, D. A. & Yin, D., 2000. X-ray analysis of the cluster 3C 129. *MNRAS*, **313**, 617–626.

Lehnert, M. D., van Breugel, W. J. M., Heckman, T. M. & Miley, G. K., 1999. Hubble Space Telescope Imaging of the Host Galaxies of High-RedshiftRadio-loud Quasars. *ApJS*, **124**, 11–31.

Longair, M., 1992. *High Energy Astrophysics*, vol. 2. Cambridge University Press.

Longair, M., 1998. *Galaxy Formation*. Cambridge University Press.

Longair, M. S., 1995. Astrophysics and Cosmology. In L. M. Brown, A. Pais & B. Pippard, eds., *Twentieth Century Physics*, 1691–1821. IOP Publishing and New York AIP Press.

Longair, M. S., Best, P. N. & Rottgering, H. J. A., 1995. HST observations of three radio galaxies at redshift $z \sim 1$. *MNRAS*, **275**, L47–L51.

Longair, M. S., Ryle, M. & Scheuer, P. A. G., 1973. Models of extended radio-sources. *MNRAS*, **164**, 243+.

McCarthy, P., van Breugel, W. & Spinrad, H., 1987. A correlation between the radio and optical morphologies of distant 3CR radio galaxies. *ApJ*, **321**, L33.

McKee, C. F., 1988. Supernova Remnant Shocks in an Inhomogeneous Interstellar Medium. In *IAU Colloq. 101: Supernova Remnants and the Interstellar Medium*, 205+. Cambridge University Press.

McKee, C. F. & Cowie, L. L., 1975. The interaction between the blast wave of a supernova remnant and interstellar clouds. *ApJ*, **195**, 715–725.

McNamara, B. R., Wise, M., Sarazin, C. L., Jannuzi, B. T. & Elston, R., 1996. Optical Structure in the Abell 1795 Cluster Central Galaxy: Evidence for Stripping and Deflection of Radio Jets. *ApJL*, **466**, L9–L12.

Nittmann, J., Falle, S. A. E. G. & Gaskell, P. H., 1982. The dynamical destruction of shocked gas clouds. *MNRAS*, **201**, 833–847.

Norman, M., 1993. Numerical Simulation of Astrophysical Jets. In D. Burgarella, M. Livio & C. P. O'Dea, eds., *Astrophysical jets*, Space Telescope Science Institute Symposium Series, 211–240. Cambridge University Press, Baltimore, USA.

O'Dea, C. P., 1985. Constraints on bent beams in narrow angle tail radio sources. *ApJ*, **295**, 80–88.

O'Dea, C. P. & Owen, F. N., 1986. Multifrequency VLA observations of the prototypical narrow-angle tail radio source NGC 1265. *ApJ*, **301**, 841–859.

O'Dea, C. P. & Owen, F. N., 1987a. Astrophysical implications of the multifrequency VLA observations of NGC 1265. *ApJ*, **316**, 95–112.

O'Dea, C. P. & Owen, F. N., 1987b. Astrophysical implications of the multifrequency VLA observations of NGC 1265. *ApJ*, **316**, 95–112.

O'Donoghue, A. A., Eilek, J. A. & Owen, F. N., 1990. VLA observations of wide-angle tailed radio sources. *ApJS*, **72**, 75–131.

Perley, R. A., Dreher, J. W. & Cowan, J. J., 1984. The jet and filaments in Cygnus A. *ApJL*, **285**, L35–L38. Image taken from `http://www.astronomica.org`, which comes from the NRAO CD-ROM: "Images from the Invisible Universe".

Raga, A. C. & Cantó, J., 1995. The initial stages of an HH jet/cloud core collision. *Revista Mexicana de Astronomía y Astrofísica*, **31**, 51–61.

Raga, A. C. & Cantó, J., 1996. The steady structure of a jet/cloud interaction - II. The case of a spherically symmetric stratification. *MNRAS*, **280**, 567–571.

Reber, G., 1940. Cosmic Static. *ApJ*, **91**, 621+.

Reber, G., 1944. Cosmic Static. *ApJ*, **100**, 279+.

Recami, E., Castellino, A., Maccarrone, G. D. & Rodonò, M., 1986. Considerations about the Apparent "Superluminal Expansions" Observed in Astrophysics. *Il Nuovo Cimento*, **93B**, 119.

Rees, M., 1966. Appearance of Relativistically Expanding Radio Sources. *Nature*, **211**, 468.

Rees, M., 1988. The radio/optical alignment of high-z radio galaxies: triggering of star formation in radio lobes. *MNRAS*, **239**, L1.

Rees, M. J., 1971. New Interpretation of Extragalactic Radio Sources. *Nature*, **229**, 312 and 510.

Reynolds, C. S., 1996. *X–Ray emission and absorption in active galaxies*. Ph.D. thesis, Institute of Astronomy, Cambridge University U.K.

Robson, I., 1996. *Active galactic nuclei*. Wiley-Praxis Series in Astronomy and Astrophysics, New York, NY: Wiley, Chichester: Praxis Publishing.

Sanders, R. H. & Prendergast, K. H., 1974. The Possible Relation of the 3-Kiloparsec Arm to Explosions in the Galactic Nucleus. *ApJ*, **188**, 489–500.

Scheuer, P. A. G., 1974. Models of extragalactic radio sources with a continuous energy supply from a central object. *MNRAS*, **166**, 513–528.

Sedov, L., 1993. *Similarity and Dimensional Methods in Mechanics*. CRC Press, 10th ed.

Sijbring, D. & de Bruyn, A. G., 1998. Multifrequency radio continuum observations of head-tail galaxies in the Perseus cluster. *Astronomy and Astrophysics*, **331**, 901–915.

Silk, J. & Wyse, R. F. G., 1993. Galaxy formation and the Hubble sequence. *Physics Reports*, **231**, 295–365.

Spitzer, L., 1982. Acoustic waves in supernova remnants. *ApJ*, **262**, 315–321.

Spitzer, L., 1998. *Physical Processes in the Interstelar Medium.* Willey.

Stanyuokovich, K. P., 1960. *Unsteady motion of continuous Media.* Pergamon.

Sutherland, R. S. & Dopita, M. A., 1993. Cooling functions for low-density astrophysical plasmas. *ApJS*, **88**, 253–327.

Taub, A. H., 1948. Relativistic Rankine–Hugoniot Equations. *Physical Review*, **74**, 328–334.

Taub, A. H., 1978. Relativistic Fluid Mechanics. *Annual Reviews of Fluid Mechanics*, **10**, 301–332.

Thorne, K. S., 1973. Relativistic Shocks: the Taub Adiabat. *ApJ*, **179**, 897–908.

Woltjer, L., 1990. Physical Processes in Active Galactic Nuclei. In T.-L. Courvoisier & M. Mayor, eds., *Active Galactic Nuclei*, Saas-Fee Advanced Course 20. Springer-Verlag, Les Diablerets.